

NEURAL CIRCUIT DYNAMICS AND FUNCTION OF COMPLEX BEHAVIORAL STATES

Joshua Holden Jennings

A dissertation submitted to the faculty at the University of North Carolina at Chapel Hill in partial fulfillment of the requirements for the degree of Doctor of Philosophy in the Graduate School (Neurobiology Curriculum).

Chapel Hill
2014

Approved by:

Garret D. Stuber

Ben D. Philpot

Cynthia M. Bulik

Spencer L. Smith

Joyce Besheer

© 2014
Joshua Holden Jennings
ALL RIGHTS RESERVED

ABSTRACT

Joshua H. Jennings: Neural circuit dynamics and function of complex behavioral states
(Under the direction of Garret Stuber)

Mammalian neural circuits are sophisticated biological systems that choreograph behavioral processes vital for survival. While the inherent complexity of discrete neural circuits has proven difficult to decipher, many parallel methodological developments promise to help delineate the function and connectivity of molecularly defined neural circuits. Here, I utilize novel neurotechniques to precisely monitor and manipulate anxiety- and feeding-related circuit activity. By using a holistic, multifaceted approach for perturbing and measuring neural circuit dynamics, we begin to provide a framework for understanding how adaptive and maladaptive behavioral states are manifested through the cooperative interactions of discrete extended amygdala, midbrain, and hypothalamic circuit elements.

To my little brother, Johnathon Gregory Taylor (1996 – 2014), I dedicate all my work and effort to you. I will always miss you and will never forget the times we shared together. You will continue to inspire me to be the best that I can.

PREFACE

The human brain contains billions of neurons that are wired together in redundant and reciprocal patterns. Complicating matters further, numerous subpopulations of neurons possess functionally, genetically, and anatomically distinct features that make them separate entities or nodes within the collective system. To translate this complexity into a tangible thought, imagine if you had to deactivate an explosive device by locating a single unidentified wire that was tangled amongst a billion of other intermingled wires. This complexity has solidified the brain as one of the most mystical components of the human body. Aristotle, also known as “The Philosopher,” made vital contributions to biology during the fifth century and was considered to be the first anatomist, embryologist, taxonomist, and animal behaviorist. However, the concept of perception and cognition confused Aristotle to the point where he falsely attributed the brain’s function to the heart. In response, Alcmaeon, a famous Greek scientist, was the first to hypothesize the brain as the controller of these complex cognitive functions. Nevertheless, the brain still remains a mystery, but the rapid advances in neuroscience may bring us closer to the truth:

“Can the brain understand the brain? Is it a giant computer, or some other kind of giant machine, or something more? The brain is a tissue. It is a complicated, intricately woven tissue, like nothing else we know of in the universe, but it is composed of cells, as any tissue is. They are, to be sure, highly specialized cells, but they function according to the laws that govern any other cells. Their electrical and chemical signals can be detected, recorded and interpreted and their chemicals can be identified; the connections that constitute the brain’s woven feltwork can be mapped. In short, the brain can be studied, just as the kidney can.” - David H. Hubel, Scientific American 1979.

This brief historical perspective demonstrates our persistent curiosity for understanding the brain. Will we ever completely understand why we feel or react the way we do? If we reach this goal, then does that make us no longer complex relative to other organisms? Keep in mind, the brain is the only tissue that categorizes or names itself. All together, these unsolved questions drive my passion for neuroscience and enhance my desire to contribute to the greater cause of solving this complex puzzle.

ACKNOWLEDGEMENTS

I would like to thank the Stuber laboratory and the UNC community for all their support. In particular, I would like to thank Alice Stamatakis for always being there for me. You are the best teammate, scientist, and person that I have ever worked with. Thank you Garret for all your guidance. Your mentorship was vital to my success as a graduate student and I truly appreciate everything you have done for me. I will continue to value these vital lessons as I move forward in my career. Some of my best memories of graduate school involve the times where we just sat and talked science even if the ideas were never materialized into a project. In my opinion, moments like those helped tremendously by teaching me how to think as a scientist. Thank you Mom, Dad, Greg, Caroline, John, Jordyn, and the rest of my family for your support, care, and guidance. Each of you significantly contributed to my growth and accomplishments. I would also like to thank my thesis committee, Ben Philpot, Joyce Besheer, Spencer Smith, and Cynthia Bulik, for their time, effort, and mentorship.

TABLE OF CONTENTS

LIST OF FIGURES.....	x
LIST OF ABBREVIATIONS.....	xii
CHAPTER 1: GENERAL INTRODUCTION.....	1
Motivated behaviors.....	1
Maladaptive behavioral states.....	2
Neural candidates for these comorbid disease states.....	3
VTA activity dynamics and function.....	6
Molecular and anatomical heterogeneity of the VTA.....	8
Function and cellular composition of the LH.....	9
Neuromodulator tools for ascribing circuit function to behavior.....	12
Providing a neural circuit wiring diagram.....	14
Neurophysiological dynamics of distinct neural circuit elements.....	16
Dissertation.....	19
CHAPTER 2: DISTINCT EXTENDED AMYGDALA CIRCUITS FOR DIVERGENT MOTIVATIONAL STATES.....	21
Introduction.....	21
Methods.....	22

Results.....	32
Discussion.....	38
CHAPTER 3: THE INHIBITORY CIRCUIT ARCHITECTURE OF THE LATERAL HYPOTHALAMUS ORCHESTRATES FEEDING.....	56
Introduction.....	56
Methods.....	57
Results.....	66
Discussion.....	69
CHAPTER 4: VISUALIZING HYPOTHALAMIC NETWORK DYNAMICS FOR MOTIVATION AND CONSUMPTION.....	82
Introduction.....	82
Methods.....	84
Results.....	96
Discussion.....	104
CHAPTER 5: DISCUSSION.....	125
General Discussion.....	125
REFERENCES.....	134

LIST OF FIGURES

Figure 1.1: Neurocircuit blueprint for diverse motivated behavioral states.....	20
Figure 2.1: Optogenetic identification of vBNST→VTA projection neurons.....	39
Figure 2.2: Optogenetic identification of CaMKIIa ^{vBNST→VTA} projection neurons in freely moving mice.....	41
Figure 2.3: vBNST→VTA projection neurons differentially respond to aversive stimuli.....	43
Figure 2.4: Neurochemically distinct vBNST cell types contain CaMKIIa and form functional excitatory and inhibitory synapses onto VTA neurons.....	44
Figure 2.5: Excitatory and inhibitory synapses onto non-dopaminergic VTA neurons from neurochemically distinct vBNST neurons.....	45
Figure 2.6: <i>Vglut2</i> ^{vBNST→VTA} and <i>Vgat</i> ^{vBNST→VTA} terminals synapse onto non-dopaminergic and I _h negative dopaminergic neurons in the VTA.....	47
Figure 2.7: <i>Vglut2</i> ^{vBNST→VTA} and <i>Vgat</i> ^{vBNST→VTA} projection neurons display distinct firing patterns in response to foot-shock and shock-associated contextual cues.....	48
Figure 2.8: Photostimulation of the <i>Vglut2</i> ^{vBNST→VTA} pathway promotes aversion and anxiety.....	50
Figure 2.9: Photostimulation of the <i>Vgat</i> ^{vBNST→VTA} pathway and inhibition of <i>Vgat</i> ^{VTA} neurons produces reward-related behaviours.....	52
Figure 2.10: Photostimulation of the <i>Vgat</i> ^{vBNST→VTA} pathway and inhibition of <i>Vgat</i> ^{VTA} neurons attenuates anxiety.....	54
Figure 3.1: <i>Vgat</i> ^{BNST→LH} circuit activation induces feeding in well-fed mice.....	70

Figure 3.2: Photoactivation of the $Vgat^{BNST \rightarrow VTA}$ pathway is rewarding, but does not produce feeding behavior.....72

Figure 3.3: $Vgat^{BNST \rightarrow LH}$ circuit inhibition diminishes feeding in food-deprived mice and is aversive.....74

Figure 3.4: $Vgat^{BNST \rightarrow LH}$ projections preferentially target LH glutamatergic neurons.....76

Figure 3.5: Photoactivation of $Vglut2^{LH}$ neurons suppresses feeding in food-deprived mice and is aversive.....78

Figure 3.6: Photoinhibition of $Vglut2^{LH}$ neurons promotes feeding and is rewarding.....80

Figure 4.1: Optogenetic Modulation of LH GABAergic Neurons Bidirectionally Modulates Feeding and Reward-Related Behaviors.....107

Figure 4.2: Bulk Chemogenetic Activation of LH GABAergic Neurons Enhances Consummatory Behaviors.....110

Figure 4.3: Neurochemically Distinct $Vgat$ LH Neurons are Completely Separate From MCH and Orx Cells.....113

Figure 4.4: Genetic Ablation of LH GABAergic Neurons Attenuates Weight Gain, Food-seeking, and Consummatory Behaviors.....115

Figure 4.5: *In Vivo* Ca^{2+} Imaging of LH GABAergic Neurons in Freely Moving Mice.....118

Figure 4.6: Subsets of LH GABAergic Neurons Display Enhanced or Reduced Activity to Environmental Locations Containing Food.....120

Figure 4.7: Separate LH GABAergic Neurons Selectively Encode Aspects of Motivation or Consumption.....122

Figure 4.8: Tracking the Activity Dynamics of Individual LH GABAergic Neurons Across Separate Behavioral Tasks.....124

LIST OF ABBREVIATIONS

3V	Third ventricle
AAV	Adeno-associated virus
aCSF	Artificial cerebral spinal fluid
Arc	Arcuate nucleus
BNST	Bed nucleus of the stria terminalis
Ca ²⁺	Calcium
CaMKIIa	Calcium/calmodulin-dependent protein kinase II a
ChR2	Channelrhodopsin-2
CNO	Clozapine-N-oxide
DA	Dopamine
DMH	Dorsal medial hypothalamus
DREADD	Designer receptors exclusively activated by designer drugs
eArch3.0	Enhanced archaerhodopsin
EP	Entopenduncular nucleus
eYFP	Enhanced yellow fluorescent protein
Fx	Fornix
GABA	Gamma-Aminobutyric acid
GCaMP6m	Genetically encoded calcium indicator-6 (medium variant)
GAD	Glutamate decarboxylase

GFP	Green fluorescent protein
GRIN	Gradient refractive index lens
hM3Dq	G _q -coupled human M3 muscarinic DREADD
LH	Lateral hypothalamus
MCH	Melanin-concentrating hormone
NpHR3.0	Halorhodopsin
Nts	Neurotensin
Orx	Orexin
taCasp3	Designer procaspase-3
<i>TH</i>	Tyrosine hydroxylase
<i>Vgat</i>	Vesicular GABA transporter
<i>Vgat</i> ^{BNST-LH}	LH-projecting BNST GABAergic neurons
<i>Vgat</i> ^{vBNST-VTA}	VTA-projecting BNST GABAergic neurons
<i>Vglut2</i>	Vesicular glutamate transporter-2
<i>Vglut2</i> ^{vBNST-VTA}	VTA-projecting BNST glutamatergic neurons
VMH	Ventral medial hypothalamus
VTA	Ventral Tegmental Area

CHAPTER 1: GENERAL INTRODUCTION¹

Motivated behaviors

Adaptive motivated behaviors, such as seeking and obtaining resources, consuming nutrients, and avoiding danger, are fundamental survival processes that are driven by an organism's basic needs. Furthermore, these survival-oriented behaviors are well conserved across all animal species and play a crucial role in many other complex behavioral states. In agreement with this, Abraham Maslow proposed that; "*Practically all organismic states are to be understood as motivated. Usually acts have more than one motivation.*" Therefore, maladaptation of these purposive behaviors likely underlies numerous mental disease states that are detrimental to society, including addiction, depression, anxiety, and eating disorders. However, the main contributing factors responsible for the manifestation of these maladaptive disease states remain poorly understood. Recent advances in neuroscience have demonstrated that an animal's behavioral intent and actions are drastically altered from direct modulation of discrete neural circuit connections, suggesting that precise neuronal signaling and coding in defined brain networks selectively coordinate motivated behaviors. Thus, elucidating how behaviorally relevant information is transferred, integrated, and represented within distinct neural circuits is critical for determining the causal underpinnings of maladaptive behavioral states and may assist in the development of proper psychiatric treatment methods.

¹Some material within this chapter previously appeared in a review published in the journal *Current Biology*. The original citation is as follows: Jennings JH, Stuber GD. (2014). Tools for resolving functional activity and connectivity within intact neural circuits. *Current Biology*. PMID: 24405680.

Maladaptive behavioral states

Stress modifies the intensity and direction of purposive behaviors, enabling an organism to properly adapt to novel environmental challenges. Chronic exposure to stressful and aversive stimuli initiates a series of maladaptive neuronal responses that can result in psychiatric disorders, such as anxiety, addiction, and depression (Davis et al., 2010). Anxiety is classified as persistent hypervigilance in the absence of aversive stimuli and immediate threats (Sylvers et al., 2011). Anxiety disorders are the most prevalent type of mental illness, affecting around 18 percent of adults in the United States (Kessler et al., 2005). Further, the expenses associated with treating anxiety as well as the lost of productivity from the disorder amounted to approximately 46 billion dollars in 1990, which accounted for 30 percent of all mental health expenditures in the United States (DuPont et al., 1996). Given the prevalence of these substantial economic and social burdens of anxiety, much emphasis is now placed on identifying the neural circuit elements that underlie this crippling disorder.

Addiction and obesity-related eating disorders share similar compulsive behaviors, such as foraging and ingestion, that persist despite adverse health, economic, or social consequences (Volkow and Wise, 2005). Addiction- and obesity-promoting environmental factors, including drugs of abuse and palatable foods, activate similar brain reward areas to enhance reward-seeking and consummatory behaviors, further supporting the notion that addiction and obesity share overlapping hedonic mechanisms (Kenny, 2011). However, the precise neural circuit modulators responsible for both overeating in obesity and excessive drug use in addiction are not well defined. Thus, delineating the mutual neural circuits that promote aspects of reward-related behaviors is a crucial scientific priority for treating addiction and obesity-related eating disorders.

Obesity is characterized as a condition in which the total amount of triglyceride stored in adipose tissue is abnormally high and is strongly associated with detrimental health problems,

including diabetes, vascular disease, and cancer (Kopelman, 2000). Approximately 30 percent of adults in the United States possess a body mass index (BMI) of >30 and thus are considered to be obese (Flegal KM et al., 2002). Moreover, obesity contributes to more than 300,000 deaths in the United States each year, making it the second leading cause of death (Allison et al., 1999). Therefore, it is of critical importance to identify the precise mechanisms that give rise to eating disorders. Disruption in adaptive feeding behavior is a defining trait of eating disorders, which are detrimental to society as they possess the highest mortality rate of any mental illness (Hudson et al., 2007). Binge-eating, classified as excessive feeding that is uncontrollable, is the most prevalent type of eating disorder¹⁵ and likely contributes to the worldwide obesity epidemic (Hill et al., 2003). Hyperphagia, also known as excessive feeding behavior, is another key factor contributing to the nationwide obesity epidemic (Swinburn et al., 2009). Furthermore, the growing abundance and easy accessibility of palatable high-fat foods are major environmental risks for the development of hyperphagia (Volkow and Wise, 2005). Therefore, pinpointing the discrete neural circuit elements that promote hyperphagia could unravel the underlying causes involved with high fat diet-induced obesity and thus provide crucial opportunities for developing novel therapeutic targets to treat obesity-related disorders. Taken together, the high prevalence of comorbidity between anxiety, addiction, and eating disorders, suggests that mutual neural circuits contribute to these disparate neuropsychiatric disease states (Back and Brady, 2008; Grilo et al., 2009; Javaras et al., 2008; Jordan et al., 2003; Kaye et al., 2004; Parylak et al., 2011; Tanofsky-Kraff et al., 2013).

Neural candidates for these comorbid disease states

The bed nucleus of the stria terminalis (BNST) was originally described by Johnston in 1923 as a limbic forebrain structure that forms a continuum with other amygdaloid structures, including the central amygdala and nucleus accumbens (Johnston, 1923). This continuum of tissue was eventually labeled as the extended amygdala (Alheid and Heimer, 1988), since the

structures within the continuum share similar neurochemical and morphological properties (Alheid, 2003). The BNST contains a vast array of molecularly distinct cell types, including GABAergic and glutamatergic neuronal populations, as well as cholinergic interneurons (Cullinan et al., 1993; Ju and Swanson, 1989; Kudo et al., 2012). Additionally, an assortment of BNST neurons synthesize and release various neuropeptides, which includes enkephalin, corticotropin releasing factor (CRF), dynorphin, neuropeptide Y (NPY), and substance P (Gray and Magnuson, 1987; Kash and Winder, 2006; Kozicz et al., 1997; Phelix and Paull, 1990; Poulin et al., 2009; Walter et al., 1991). These heterogeneous cell types are located throughout multiple subdivisions of the BNST, such as the dorsal (BNSTd) and ventral (BNSTv) sub-regions (Johnston, 1923; Ju and Swanson, 1989).

The BNST also possesses a complex connectivity profile as evident by the structure's numerous connections that spread diffusely throughout the brain (Dong and Swanson, 2004; Dong et al., 2000, 2001a, 2001b). Moreover, the BNST is considered to be a major relay hub between stress regions and brain reward centers, since it is heavily interconnected with midbrain, hindbrain, amygdala, and hypothalamic areas that are important for mediating many of the autonomic and behavioral responses to aversive and reward-related stimuli (Walker et al., 2003). Thus, the BNST is thought to play an important role in the integration of behavioral states that have both positive and/or negative valences. Taken together, the diverse cell types as well as the complex wiring of the BNST arm the structure with the necessary tools for modulating diverse aspects of motivated behaviors, while also making it difficult to dissect the region's precise functions and dynamics that underlie complex behavioral states.

The BNST has been implicated in modulating pathological anxiety-like states that result from chronic stress exposure and/or aversive stimuli (Davis et al., 2010). Complimentary to this idea, recent studies demonstrated that ablation or chemical inactivation of the BNST alters the behavioral consequences of stress and reduces anxiety (Christianson et al., 2011; Duvarci et

al., 2009; Hammack et al., 2004; Schulz and Canbeyli, 2000; Walker et al., 2003), while pharmacological activation of the BNST enhances anxiety-like phenotypes (Walker and Davis, 1997). Furthermore, human imaging studies have shown that BNST activity is enhanced in response to aversive stimuli (Somerville et al., 2010; Straube et al., 2007). In addition, BNST neurons respond to cocaine exposure (Mahler and Aston-Jones, 2012) and modulate the reinforcing properties of opiates (Walker et al., 2000), indicating that the BNST may also be involved with reward-related processes. The consumption and anticipation of food also activates BNST neurons (Ángeles-Castellanos et al., 2007) and the BNST heavily innervates motivated-feeding areas such as the lateral hypothalamus (LH) (Hahn and Swanson, 2012; Kim et al., 2013). Thus, the BNST may also play a pivotal role in regulating food intake through its molecularly- and projection-specific connections with the hypothalamus. Though these past findings define a causal role for the BNST in modulating anxiety and addiction-related states, the manipulations used by each study lack molecular and anatomical specificity and thus do not reveal the genetically distinct and projection specific cell populations that are mediating these diverse behavioral effects.

Initial electrophysiological and anatomical tract tracing studies demonstrated that a direct anatomic connection exists between the BNST and a classic brain reward center, the ventral tegmental area (VTA) (Georges and Aston-Jones, 2002; Kudo et al., 2012). In agreement with this, electrical stimulation of the BNSTv results in consistent activation of VTA neurons (Georges and Aston-Jones, 2001), implying that a functional connection may also exist between both brain structures. Thus, the projections from the BNST to the VTA may provide a circuit mechanism through which the BNST controls anxiety- and reward-related behaviors. However, the precise genetic composition as well as the activity dynamics and functional roles of this circuit remain largely unknown.

VTA activity dynamics and function

The VTA, a heterogeneous midbrain region comprised primarily of dopamine (DA) neurons (approximately 60%) (Margolis et al., 2006a; Swanson, 1982), is canonically viewed as a crucial regulator of motivated behaviors. Numerous behavioral, pharmacological, electrophysiological, and anatomical studies have associated the activity of these neurons with various functions including aversion, salience, novelty, and reward processing (Bromberg-Martin et al., 2010; Schultz, 2007; Ungless et al., 2010). DA neurons within the VTA are considered to be one of the principal neuronal systems of reward function. Consistent with this idea, selective ablation of DA neurons and blockade of DAergic signaling within major target sites of the VTA, such as the ventral and dorsal striatum, drastically attenuate motivational responding for normally rewarding substances (Ettenberg and Camp, 1986; Fouriez et al., 1978; McFarland and Ettenberg, 1995; Ungerstedt, 1971; Wise et al., 1978; Yokel and Wise, 1975; Zarevics and Setler, 1979). Thus, the reward value of food, drugs, and brain stimulation is diminished in animals that have impaired DA function and signaling. In contrast, selective activation of VTA DA neurons enhances behavioral conditioning and increases motivation to obtain rewards (Adamantidis et al., 2011; Tsai et al., 2009). Collectively, these initial studies defined a causal role for VTA DA neurons in modulating motivation and reward-related behaviors. Although these functional assays ascribe DA function to motivated behaviors, the findings only offer causal information and thus do not account for the natural DAergic activity dynamics that likely underlie discrete components of motivation. Therefore, to determine how these neurons are able to act as valence detectors, one must elucidate how the DA system integrates and converts external stimuli from the environment into an internal representation by monitoring the endogenous activity patterns of VTA DA neurons during discrete behavioral states.

Past activity-based measurements revealed that VTA DA neurons display unique activity dynamics during various motivated behavioral states. Specifically, seminal studies involving *in*

vivo extracellular recordings within the VTA of primates and rodents, and fMRI imaging in humans, showed that the delivery of unexpected rewards as well as the presentation of reward-predictive cues enhance DA activity, while the absence of an expected reward decreases DA activity (Bayer and Glimcher, 2005; Cohen et al., 2012; D'Ardenne et al., 2008; Ljungberg et al., 1992; Mirenowicz and Schultz, 1994; Schultz, 1997, 1998; Schultz et al., 1993, 1993; Takikawa et al., 2004). In addition, DA neurons also respond to aversive stimuli in a heterogeneous manner, as aversive stimuli can excite or inhibit distinct VTA neuronal subpopulations (Brischoux et al., 2009; Bromberg-Martin et al., 2010; Cohen et al., 2012; Matsumoto and Hikosaka, 2009). Furthermore, additional studies associated DA neuron activity and function with stress- and depression-related phenotypes (Anstrom and Woodward, 2005; Anstrom et al., 2009; Chaudhury et al., 2013). Clearly, VTA DA neurons are a functionally heterogeneous network of cells that serve divergent roles in motivational control. These bidirectional valence-coding properties of VTA DA neurons enable an organism to perform a wide range of motivated behaviors that are essential for survival. However, due to the multitude of computational and functional roles of VTA DA neurons, it has remained a major challenge to precisely decipher the behavioral contribution and computation of each neuronal subtype within the VTA. Therefore, the origin of these dual-signaling modalities within the VTA and the identity of their "master neural controller" remain unknown. For example, what upstream neural signals precede these valence detector signals in the VTA? Since VTA neuronal activity is under direct control of precise inputs that arise from both distal and local connections (Geisler and Zahm, 2005a; Watabe-Uchida et al., 2012), the functional and computational heterogeneity of these distinct valence-coding patterns are likely due to differences in connectivity of discrete VTA neuronal subtypes.

Molecular and anatomical heterogeneity of the VTA

The molecular and anatomical heterogeneity within the VTA may contribute to the diverse functions of DA neurons in processing aspects of reward and aversion (Ikemoto, 2007; Lammel et al., 2008; Nair-Roberts et al., 2008). Intermingled with DA neurons, are also a large population of GABAergic cells that account for approximately 30 percent of the total VTA population (Van Bockstaele and Pickel, 1995; Johnson and North, 1992; Margolis et al., 2006b). VTA GABAergic neurons suppress DA activity by forming local inhibitory synapses onto neighboring VTA DA cells (Johnson and North, 1992; van Zessen et al., 2012) Further, selective activation of VTA GABAergic neurons disrupts reward consumption (van Zessen et al., 2012), and these neurons display increased activity in response to aversive stimuli (Cohen et al., 2012), indicating that VTA DA and GABAergic neurons share opposing roles for regulating and computing reward and aversion.

The activity of VTA DA neurons is also regulated by distal inputs arising from various brain regions, including hypothalamic nuclei, amygdala/extended amygdala regions, and hindbrain areas (Abler et al., 2012; Edinger et al., 1977; Geisler and Zahm, 2005a; Hernandez and Hoebel, 1988; Kempadoo et al., 2013; Korotkova et al., 2003; Kranz et al., 2010; Liu et al., 2014; Maeda and Mogenson, 1982; Schweimer and Ungless, 2010). Recent tracing studies further highlight the BNST as a major input of the VTA. In particular, these studies reveal that BNST axonal projections primarily target VTA GABAergic neurons, while also innervating a small population of DA neurons (Kudo et al., 2012; Watabe-Uchida et al., 2012). Furthermore, Kudo and colleagues refined the neurochemical composition of this circuit by combining retrograde tracing with fluorescence *in situ* hybridization for GABAergic and glutamatergic markers in VTA-projecting BNST neurons and found that both glutamatergic and GABAergic BNST neuronal subpopulations project to the VTA and synapse primarily onto VTA GABAergic neurons (Kudo et al., 2012). While these innovative tracing studies offer genetic specificity at

the presynaptic and postsynaptic sites of the BNST to VTA circuit connection, the existence of a functional connection within this pathway has not been established. Also, the functional significance of this circuit for controlling reward, aversion, and anxiety is completely unknown. Thus, a key objective of this dissertation is to reveal the functional and genetic composition of the BNST to VTA pathway, while also attempting to define a causal role for this circuit in controlling divergent motivated states.

Function and cellular composition of the LH

The LH, an evolutionary ancient and well-conserved brain structure (Tessmar-Raible et al., 2007), was first highlighted as the feeding and motivation center over half a century ago by influential studies that employed gross manipulation tactics. These initial studies underscored the necessity of the LH for feeding and motivation by demonstrating that non-specific electrical activation of the LH elicited voracious feeding behavior in rodents (ANAND and BROBECK, 1951; DELGADO and ANAND, 1953) and positive reinforcement behavior (Hoebel and Teitelbaum, 1962; Olds, 1958; OLDS and MILNER, 1954), while ablation of the region resulted in diminution of feeding with pronounced emaciation (Anand and Brobeck, 1951). Additional electrical stimulation experiments showed that electrical stimulation of LH can also evoke drinking (Greer, 1955), aggression (Woodworth, 1971), and sexual behaviors (Vaughan and Fisher, 1962), suggesting that the LH is involved with many purposive behaviors that satisfy an organism's basic needs. The vast assortment of genetically distinct cell types within the LH likely contribute to these diverse behavioral responses (Berthoud and Münzberg, 2011; Harthoorn et al., 2005). Thus, given the heterogeneous cellular composition of the LH, and the fact that multiple fibers of passage traverse this region, electrical stimulation or lesion studies are not suitable for determining the precise genetically defined neuronal populations in the LH that regulate feeding and positive reinforcement behavior.

The LH encompasses a plethora of genetically and functionally distinct cell types that utilize various signaling modalities, including neurotransmitters and neuropeptides (Allen and Cechetto, 1995; Burdakov and Alexopoulos, 2005; Collin et al., 2003; Goforth et al., 2014; Griffond and Risold, 2009; Laque et al., 2013a; Leininger et al., 2009), to control nutrient intake. Vesicular glutamate transporter type 2 (*Vglut2*; a marker for glutamate neurons) mRNA expression is abundant in the LH (Collin et al., 2003; Rosin et al., 2003; Ziegler et al., 2002), suggesting that numerous LH neuronal subpopulations synthesize the excitatory neurotransmitter, glutamate. In addition to glutamate, the LH is enriched with GABAergic neurons (Acuna-Goycolea et al., 2005; Karnani et al., 2013; Laque et al., 2013a; Rosin et al., 2003), which are completely separate from *Vglut2*-expressing LH cells (Ziegler et al., 2002). These prevalent neurotransmitter-containing neurons in the LH also coexpress several feeding-related neuropeptides, including orexin (Orx), melanin-concentrating hormone (MCH), neurotensin (Nts), and galanin (GAL).

Neurons that synthesize and release the neuropeptide Orx (~5000 total in rodents) are restricted to the LH and also express *Vglut2* (Rosin et al., 2003). Orx neurons are thought to promote feeding and reward seeking behaviors. Consistent with this idea, injections of the peptide into the lateral ventricle increases food intake (Sakurai, 1999), while Orx receptor antagonists and genetic removal of Orx decrease consumption (Haynes et al., 2002). Furthermore, chemical activation of Orx cells as well as infusions of the peptide into the VTA reinstate drug- and food-seeking behaviors (Harris et al., 2005). However, these neurons are also heavily involved with arousal, as Orx neuron activation increases wakefulness (Adamantidis et al., 2007), while genetic ablation of the cells causes narcolepsy (Hara et al., 2001). Therefore, the feeding related properties of Orx might be a secondary effect from its regulation of arousal.

MCH cells are also only found in the LH and are distinct from Orx neurons (Bittencourt et al., 1992; Elias et al., 1998). Several MCH neurons express markers for GABA (glutamatic acid decarboxylase; GAD67) and glutamate (*Vglut2*) (Elias et al., 2008; Harthoorn et al., 2005; Jego et al., 2013), suggesting that MCH neurons are composed of subsets of inhibitory and excitatory cells. MCH neurons have also been implicated in the regulation of feeding and sleep-wakefulness balance. Intracerebroventricular injections of the peptide increases feeding and body weight in rodents (Qu et al., 1996). Further, recent genetic studies revealed that overexpression of MCH leads to hyperphagia and obesity (Ludwig et al., 2001), while mice lacking MCH neurons are hypophagic and lean (Alon and Friedman, 2006). In contrast to Orx neurons, activation of MCH neurons promotes sleep (Jego et al., 2013).

A separate neuropeptide-containing cell population within the LH (Kahn et al., 1980), Nts neurons, have been ascribed to be involved with negative energy balance. Peripheral and central administration of Nts suppresses feeding (Cooke et al., 2009), and both the genetic ablation of Nts neurons that contain leptin receptors, as well as the removal of the Nts receptor (NTR1) in a knock-out mouse model, result in hyperphagia and obesity (Kim et al., 2008; Leininger et al., 2011). Nts neurons highly colocalize with GAL-expressing neurons (~95% overlap), but not with MCH and Orx cells (Laque et al., 2013b).

Given that numerous molecularly distinct LH neuronal populations have been associated with feeding and that over 50 neuronal products in the brain have experimental consequences on feeding behavior (Harrold and Halford, 2006), differentiating the precise cell types and input regions of the LH that control nutrient intake has proven to be a difficult task. To accomplish this, a multidisciplinary approach can be used to systematically characterize the connectivity, function, and neurophysiological dynamics of precise neural circuits during food-motivated and consummatory behaviors. Assembling a genetically precise neural circuit wiring diagram and unraveling the choreography of neuronal network dynamics within a defined neurocircuit with

advanced *in vivo* measurements and manipulations, should provide critical insights into how neuronal networks within these regions of interest, the BNST, VTA, and LH, orchestrate motivated behavioral states.

Neuromodulator tools for ascribing circuit function to behavior

Manipulating neurons to control behavioral responses has been a hallmark feature of neuroscience (Caggiula and Hoebel, 1966; Hoebel and Teitelbaum, 1962; MARGULES and OLDS, 1962; OLDS and MILNER, 1954). The brain, however, embodies a mosaic of diverse cell types that are exquisitely woven together, thus manipulations involving non-specific electrical stimulation are not sufficient for ascribing brain function to behavior. The functional role of different cell types can be defined by their genetic complexion, therefore genetically directed manipulations are vital for understanding the causal link between specific circuit function and mammalian behavior. Advances in molecular genetics and genetically guided activity modulators have provided entry points for identifying precise neurocircuits that modulate the intensity and direction of certain behaviors. To selectively target genetically defined neuronal populations, Cre recombinase in transgenic animals can be used to turn on gene expression for Cre-dependent viral vectors encoding optogenetic modulators, such as the excitatory opsin, channelrhodopsin-2 (ChR2), and inhibitory opsins, halorhodopsin-3 (NpHR3.0) and archaerhodopsin (eArch3.0) (Atasoy et al., 2008; Cardin et al., 2009; Chow et al., 2010, 2010; Kravitz et al., 2010; Mattis et al., 2012; Saunders et al., 2012; Sohal et al., 2009; Tsai et al., 2009).

ChR2, a light-gated cation channel, is expressed in the somas and axonal fibers of neurons (Yizhar et al., 2011). Thus, ChR2 can be used to activate the cell bodies of select neuronal populations as well as axonal projections within defined circuit connections (Adamantidis et al., 2007; Stuber et al., 2011). Since ChR2 is activated by blue light (450-490 nm) (Nagel et al., 2003), an implantable optical fiber is inserted directly into brain tissue and

positioned above the region expressing the membrane-bound ion channel. Upon illumination via an optical fiber interfaced with a 473-nm solid state laser, the channel opens rapidly and an influx of cations enter the cell, resulting in light-evoked action potentials (Boyden et al., 2005). Optogenetic activation of genetically distinct neurocircuit elements offers valuable causal information by demonstrating that the activity of a particular neuronal population or circuit is sufficient for driving a certain behavioral state.

Inhibitory opsins can be used to determine if neuronal activity in a given region or circuit is required for a particular behavior. In contrast to ChR2, NpHR3.0 is a light-activated chloride pump that suppresses neuronal activity by pumping chloride ions from the extracellular to the intracellular space of the cell upon yellow light presentation (~590 nm) (Gradinaru et al., 2010; Tye et al., 2011; Witten et al., 2010; Zhang et al., 2007). eArch3.0, an outward proton pump, can also be used for somata and terminal photoinhibition applications (Chow et al., 2010; Fenno et al., 2011; Mattis et al., 2012). In response to yellow/green (~566 nm) light delivery, eArch3.0 pumps protons out of the cell, causing hyperpolarization of the cell and decreased neuron spiking (Chow et al., 2010).

Although optogenetic manipulations offer precise temporal control of neural circuit activity, the propensity of decreased opsin efficiency and phototoxicity significantly increases during chronic behavioral manipulations. Thus, behavioral experiments that demand sustained neuronal modulation may consider using 'designer receptors exclusively activated by designed drugs, or DREADDs (Coward et al., 1998; Rogan and Roth, 2011). DREADD-mediated manipulations utilize a pharmacologically inert compound, clozapine-*N*-oxide (CNO), that potently activates a family of muscarinic receptors on a longer timescale (up to several hours), allowing for selective modulation of signal-transduction pathways that is sustained through long durations (Armbruster et al., 2007). In comparison to the properties of optogenetic manipulators, longer-term chemogenetic approaches have the capacity to induce prolonged

hyperpolarization and depolarization effects in genetically defined neuronal populations (Alexander et al., 2009; Atasoy et al., 2012; Krashes et al., 2011; Sasaki et al., 2011), making it a more viable option for reproducing the natural physiological characteristics of particular behavioral/disease states that are associated with persistent hyper- or hypo-activated neural circuits.

Providing a neural circuit wiring diagram

Unraveling the intricate neural wiring patterns within molecularly defined circuits is essential for elucidating the anatomical specificity underlying particular behavioral states. While gross neuroanatomical tracing methods have been used since the dawn of modern neuroscience to provide critical insight into the axonal wiring between brain regions, these classical strategies typically cannot delineate neural circuit connectivity originating from 'genetically' distinct neuronal populations (that is, populations differing in their states of gene expression). Anterograde tracing viruses, such as Adeno-associated viruses (AAVs) (Monahan and Samulski, 2000) encoding ChR2 tagged with a fluorescent protein (ChR2-eYFP), are useful for mapping specific axonal projections and their selective destination points within distinct brain regions. AAV-mediated delivery of ChR2-eYFP to projection neurons in one brain region results in somata transduction (Gradinaru et al., 2009; Lee et al., 2010) and subsequently leads to anterograde transfer of the membrane-bound fusion protein to the axon terminals in downstream regions (Lewis et al., 2011; Stuber et al., 2011; Tye et al., 2011), allowing anatomical visualization of the pattern and density of innervation. However, these AAV-based anterograde tracing strategies cannot exclusively identify functional connections between multiple circuit nodes and so should only be used as an initial guide for visualizing possible neurocircuit interactions. Functional connectivity between two brain regions can be revealed through the combination of optogenetic approaches, i.e. ChR2, and patch clamp electrophysiology. For example, if a functional connection exist within a defined circuit then

whole cell recordings in the postsynaptic neurons with concurrent photostimulation of afferents expressing ChR2-eYFP will result in timelocked optically-evoked postsynaptic currents (Chuhma et al., 2011).

Axonal terminal targeting with retrograde transsynaptic viruses can be used to determine the specific connections between postsynaptic seed neurons and their upstream presynaptic input cells. The Pseudorabies and Rabies viruses are well characterized and serve as effective transneuronal tracers of multisynaptic circuit connections (Callaway, 2008; Kelly and Strick, 2000). Given that any particular brain region contains a multitude of cell types and connections with other structures, and that the fast rate of retrograde viral spread increases the number of synaptic phases, it becomes increasingly challenging to decipher the precise wiring from the initial viral infection site (Nassi and Callaway, 2006). Thus, the ideal tracing scenario would involve targeting genetically defined postsynaptic starter neurons and their monosynaptic inputs with a transsynaptic retrograde tracer. Wickersham *et al.* (Wickersham et al., 2007) made this possible by developing a modified monosynaptic rabies virus, EnvA-SADΔG-GFP, which restricts viral infection to a genetically distinct postsynaptic cell type and its monosynaptic input cell. Under normal circumstances the modified rabies virus does not infect mammalian tissue, but infection will occur in the presence of the envelope glycoprotein of avian sarcoma/leukosis (EnvA) receptor, TVA. Thus, postsynaptic target neurons must express TVA for initial rabies infection, as well as the rabies glycoprotein (RG) for the formation of new viral particles and transsynaptic spread. Cre-dependent viral delivery of TVA and RG along with the infusion of the modified rabies virus sufficiently labels presynaptic neurons with GFP from a single postsynaptic seed neuron (Wall et al., 2013; Watabe-Uchida et al., 2012). This viral construct enables specific presynaptic neurons to be targeted with many new rabies virus variants to perturb and record activity from discrete circuit connections (Osakada et al., 2011). Despite the utility of these viral tracing tools for circuit mapping, complimentary approaches, such as ChR2-

assisted slice electrophysiology experiments, should be used in combination to validate the presence of a functional synaptic connection between virally identified circuits. Another important factor to consider when applying these viral tracing techniques is the complexity and diversity of various synaptic connections that may display differences in transsynaptic viral spread. Accordingly, the absence of viral labeling does not exclusively rule out a specific circuit connection.

Neurophysiological dynamics of distinct neural circuit elements

The ability to identify *in vivo* single-unit activity originating from genetically defined neurons provides an avenue for elucidating how specific neuronal subpopulations are engaged by environmental stimuli (Cohen et al., 2012; Kvitsiani et al., 2013; Lima et al., 2009; Zhang et al., 2013). Without these genetically guided electrophysiological approaches, the readout from extracellular recordings within brain tissue that originates from a vast array of diverse cell types, oftentimes with their own unique function, makes it virtually impossible to definitively characterize the activity patterns of select neuronal subpopulations. As extracellular recordings within a given brain region usually reveal a multitude of discrete firing profiles timelocked to behaviorally relevant stimuli, it is now critical to determine if these functionally distinct activity patterns arise from genetically distinct neuronal subpopulations. Identifying distinct activity patterns will likely be fundamental for illustrating how whole neurocircuit systems are equal to the sum of their individual parts (genetically and functionally distinct cell types).

When extracellular recordings are performed, ChR2 can be a useful physiological tag or marker, as a brief pulse of blue light elicits a short-latency action potential in cells expressing ChR2 that is reliably detected across multiple light presentations (Cardin, 2012; Cardin et al., 2010; Lima et al., 2009). Consequently, cells expressing ChR2 are distinguishable from 'ChR2-negative' neurons during *in vivo* extracellular recordings based on their electrical responses to

light. Under certain circumstances, however, using phototagging methods to identify light-responsive neurons may generate false-negatives or false-positives. For example, some light-evoked responses may be mediated through both local and distal polysynaptic circuit modulation, as photoexcitable ChR2-expressing neurons may respond to light and elicit detectable spikes from neighboring synaptic partner neurons that do not express ChR2, thus giving a false-positive. When trying to identify neurons *in vivo*, there are certain criteria that can be used to minimize such problems. First, demonstrate a high-spike fidelity in response to high photostimulation frequencies (Cohen et al., 2012). Second, confirm that detected units possess short light-evoked latencies that have minimal variance (spike jitter) (Cohen et al., 2012; Zhang et al., 2013). Third, show that light delivery at certain intensities should does not alter the shape of the detected waveform, indicating that the responses to light are not caused from direct photoelectric artifacts (Cohen et al., 2012).

While these criteria may uphold for particular cell types, other cells of interest may require adjustments or alternative criteria for properly identifying light responses. False-negative occurrences are influenced by factors underlying the detectability of light responses in recorded neurons. The detectability of light-responsive neurons depends on the level of ChR2 expression and on the volume of tissue that is efficiently illuminated by light. ChR2 expression strength is contingent upon the diffusion and spread of viral particles as well as the viral titer, while the volume of illuminated tissue relies on the intensity and scattering of the light in tissue. Thus, the absence of light-evoked responses does not completely rule out the possibility that a recorded neuron expresses the target gene.

The functional role of particular neurons depends on how they are integrated within a circuit. Thus, specific neuronal subpopulations that project to different postsynaptic target regions often display unique firing patterns compared to cells that project elsewhere. Therefore, phototagging of genetically defined neurons in a projection-specific fashion can further define

and refine the computational role of participant cells within a complex circuit. To accomplish this, ChR2 localized in axons and presynaptic terminals can be activated via light delivery through implanted optical fibers. Congruently, multielectrode recording devices can be implanted near the somas of these ChR2-targeted neurons. Photostimulation of ChR2-expressing axonal fibers elicits an antidromic spike that propagates from the axons back to the soma region where the implanted electrode is capable of detecting these antidromic-initiated spikes. To confirm that detected light-evoked spikes originate from antidromic action potentials, orthodromic and antidromic photostimulations that occur close in time can be used to demonstrate that the photoinitiated spikes, traveling in opposite directions, collide with each other and occlude the detectable spike. Spike collision is a key indicator that the action potentials are conducting along the same axon and thus are not due to synaptic transmission within a polysynaptic circuit (Fuller and Schlag, 1976; Nagy and Paré, 2008). Because ChR2 is expressed along axons, in certain situations the photoinitiation site of the antidromic spike is not restricted to the terminals and may arise from photoactivated fibers of passage that traverse through the postsynaptic target region. This key factor should be kept in mind when antidromic photostimulation methods are used to identify projection-specific activity.

While *in vivo* extracellular recordings can produce valuable neurophysiological information in a precise temporal fashion, there are many challenges faced with this technique that can drastically hinder the investigation of neurocircuit dynamics. Modifications that have been made to long-term *in vivo* imaging techniques (Huber et al., 2012), along with the advent of newer variants of genetically encoded calcium indicators (Akerboom et al., 2012; Chen et al., 2013), have partially alleviated some of the limiting factors of extracellular recordings by resolving the activity from large genetically-defined neuronal populations over extended timescales (Dombeck et al., 2010; O'Connor et al., 2010; Tian et al., 2009; Ziv et al., 2013). Given that calcium ions (Ca^{2+}) enter the cell in response to neuronal activation (Baker et al.,

1971), and that engineered fluorescent proteins display changes in fluorescent intensity as they bind Ca^{2+} (Akerboom et al., 2009), action potentials and synaptic transmission are reliably measured by imaging changes in intracellular free Ca^{2+} (Yasuda et al., 2004). Chen and colleagues (Chen et al., 2013) recently developed a family of ultrasensitive protein calcium sensors (GCaMP6) that allow for reliable detection of single action potentials in neuronal somata.

Optical-fiber based approaches (Adelsberger et al., 2005; Cui et al., 2013; Gunaydin et al., 2014; Ziv et al., 2013) that are being developed are suited for complicated freely moving behavioral experiments that require *in vivo* imaging of activity in large neuronal populations situated in deep brain regions. Microendoscopes are composed of a relay lens fused to a doublet of gradient-index (GRIN) microlenses. GRIN lenses have a flat optical surface to refract light through a refractive index gradient and are able to efficiently focus and collect light through highly scattered tissue in deep brain regions (Göbel et al., 2004). High-speed, miniature epifluorescence microscopes (weighing less than 2 g) equipped with a complimentary metal oxide semiconductor (CMOS) image sensor and interfaced with a microendoscope are able to resolve simultaneous Ca^{2+} signals in large populations of genetically defined neurons. Notably, these integrated microscopes can repeatedly image neuronal populations for weeks to months (Ziv et al., 2013). Further technical developments, including innovative microendoscopic methods and Ca^{2+} indicators, will likely prove to be pivotal for addressing how large ensembles of genetically defined neurons encode aspects of multifaceted behavioral tasks.

Dissertation

Anxiety, addiction, and eating disorders are highly comorbid, suggesting that common neural circuits may underlie these debilitating neuropsychiatric disease states (Back and Brady, 2008; Grilo et al., 2009; Javaras et al., 2008; Jordan et al., 2003; Kaye et al., 2004; Parylak et al., 2011; Tanofsky-Kraff et al., 2013). The BNST, a neural component of the extended

amygdala (Heimer and Alheid, 1991), serves as a potential candidate for integrating comorbid disease conditions through its various circuit connections. While the BNST is canonically viewed as a modulator of fear and anxiety (Davis et al., 2010), its diverse synaptic targets, including the VTA (Geisler and Zahm, 2005b; Georges and Aston-Jones, 2001b, 2002; Kim et al., 2013), a brain region implicated in reward and aversion (Cohen et al., 2012; Fields et al., 2007; Lammel et al., 2012; Stamatakis and Stuber, 2012; Tan et al., 2012; Tye et al., 2013; van Zessen et al., 2012b), as well as the LH (Hahn and Swanson, 2012; Kim et al., 2013), a neurosubstrate known to promote feeding and positive reinforcement behavior (DELGADO and ANAND, 1953; Hoebel and Teitelbaum, 1962; MARGULES and OLDS, 1962; Wise, 1968), indicates that the BNST may govern a multitude of motivational processes. Thus, a major goal of this thesis is to systematically dissect the precise neural circuits and networks that regulate stress-, reward-, and feeding-related processes (**Figure 1.1**). To accomplish this, we monitored and manipulated the activity of projection-specific and genetically distinct neurons within the BNST to VTA circuit (**Chapter 2**) and identified the circuit connectivity and functional significance of the BNST to LH pathway for feeding (**Chapter 3**). Lastly, we monitored and manipulated the activity of genetically distinct LH GABAergic neurons to uncover the precise feeding- and motivation-coding ensembles within the LH (**Chapter 4**).

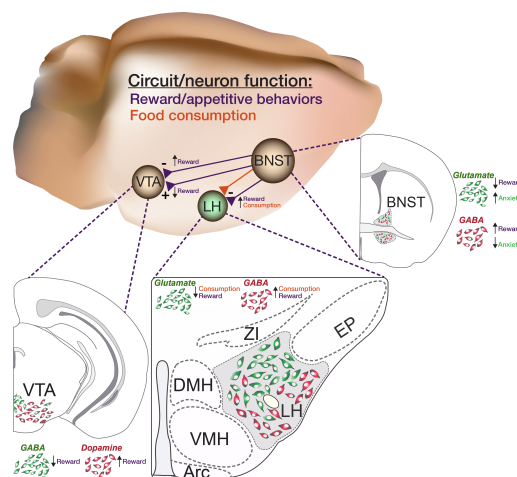


Figure 1.1: Neurocircuit blueprint for diverse motivated behavioral states.

CHAPTER 2: DISTINCT EXTENDED AMYGDALA CIRCUITS FOR DIVERGENT MOTIVATIONAL STATES²

Introduction

The co-morbidity of anxiety and dysfunctional reward processing in illnesses such as addiction (Koob and Le Moal, 2001) and depression (Nestler and Carlezon, 2006) suggests that common neural circuitry contributes to these disparate neuropsychiatric symptoms. The extended amygdala, including the bed nucleus of the stria terminalis (BNST), modulates fear and anxiety (Davis et al., 2010; Walker and Davis, 2008), but also projects to the ventral tegmental area (VTA) (Geisler and Zahm, 2005; Georges and Aston-Jones, 2001), a region implicated in reward and aversion (Cohen et al., 2012; Fields et al., 2007; Lammel et al., 2012; Stamatakis and Stuber, 2012; Tan et al., 2012; Tye et al., 2013; van Zessen et al., 2012), thus providing a candidate neural substrate for integrating diverse emotional states. However, the precise functional connectivity between distinct BNST projection neurons and their postsynaptic targets in the VTA, as well as the role of this circuit in controlling motivational states, have not been described. Here we record and manipulate the activity of genetically and neurochemically identified VTA-projecting BNST neurons in freely behaving mice. Collectively, aversive stimuli exposure produced heterogeneous firing patterns in VTA-projecting BNST neurons. By contrast, *in vivo* optically identified glutamatergic projection neurons displayed a net enhancement of activity to aversive stimuli, whereas the firing rate of identified GABAergic (γ -

²This chapter previously appeared as an article published in the journal *Nature*. The original citation is as follows: Jennings JH*, Sparta DR*, Stamatakis AM, Ung RL, Pleil KE, Kash TL, Stuber GD. (2013). Distinct extended amygdala circuits for divergent motivational states. *Nature* 496, 224-228. PMID: 23515155.

aminobutyric acid-containing) projection neurons was suppressed. Channelrhodopsin-2-assisted circuit mapping revealed that both BNST glutamatergic and GABAergic projections preferentially innervate postsynaptic non-dopaminergic VTA neurons, thus providing a mechanistic framework for *in vivo* circuit perturbations. *In vivo* photostimulation of BNST glutamatergic projections resulted in aversive and anxiogenic behavioural phenotypes. Conversely, activation of BNST GABAergic projections produced rewarding and anxiolytic phenotypes, which were also recapitulated by direct inhibition of VTA GABAergic neurons. These data demonstrate that functionally opposing BNST to VTA circuits regulate rewarding and aversive motivational states, and may serve as a crucial circuit node for bidirectionally normalizing maladaptive behaviours.

Methods

Experimental subjects and stereotactic surgery

All procedures were conducted in accordance with the Guide for the Care and Use of Laboratory Animals, as adopted by the NIH, and with approval of the Institutional Animal Care and Use Committee at UNC. Adult (25-30g) male C57BL/6J mice (Jackson Laboratory), adult male *Vgat-ires-cre* mice and adult male *Vglut2-ires-cre* mice (see (Vong et al., 2011) for additional details on the *Vglut2-ires-cre* and *Vgat-ires-cre* mouse lines) were group housed prior to surgery. All mice were maintained on a reverse 12 hr light cycle (lights off at 07:00) with *ad libitum* access to food and water, unless described below. Mice were anesthetized with a ketamine (150 mg per kg of body weight) and xylazine (50 mg per kg) solution and placed into a stereotactic frame (Kopf Instruments). For all *in vivo* electrophysiology experiments, male mice were unilaterally injected with 0.5 μ l of purified and concentrated adeno-associated virus (AAV) ($\sim 10^{12}$ infections units per ml, packaged and titered by the UNC Vector Core Facility) into the VBNST using the following stereotactic coordinates: + 0.14 mm to bregma, +/- 0.9 lateral to midline, and - 4.8 mm ventral to the skull surface (Franklin and Paxinos, 2007). All viral

constructs were packaged by the UNC vector core facility at a final working concentration of $1 - 5E12$ genome copies per mL.

For all *in vivo* electrophysiology experiments, mice were implanted with a 16-wire (4 x 4 configuration, wire diameter~30 μ m) tungsten multielectrode array (MEA) (Innovative Neurophysiology, Inc) aimed at the vBNST using the stereotactic coordinates stated above. For all *in vivo* electrophysiological and *in vivo* behavioral experiments, except for the VTA microinjection experiments, all mice were implanted with an optical fiber aimed at the VTA using the following stereotactic coordinates: -3.2 mm to bregma, +/-0.5 lateral to midline, and - 4.69 mm ventral to skull surface. For the VTA microinjection experiments, a 26-gauge steel tube cannula (McMasters-Carr) that terminated 0.5 mm above the tip of the optical fiber was epoxied to an optical fiber and unilaterally aimed at the VTA using the following stereotactic coordinates: -3.2 mm to bregma, +/-0.5 lateral to midline, and -4.69 mm ventral to skull surface. For photoinhibition of VTA-GABAergic neurons using NpHR3.0, all mice were bilaterally implanted with an optical fiber at a 10° angle in the VTA using the following stereotactic coordinates: -3.2 mm to bregma, +/-1.1 lateral to midline, and - 4.75 mm ventral to skull surface. The time from virus injection to the start of the experiments was 4 – 6 weeks for all ChR2 terminal stimulation manipulations and 3 – 4 weeks for cell body manipulations.

Histology, immunohistochemistry, and microscopy

Mice were anesthetized with pentobarbital and transcardially perfused with phosphate buffered saline (PBS) followed by 4% paraformaldehyde (weight/volume) in PBS. 40 μ m brain sections were subjected to immunohistochemical staining for neuronal cell bodies (NeuroTrace Invitrogen; 640 nm excitation/660 nm emission or 435 nm excitation/455 nm emission and/or tyrosine hydroxylase (TH)) (Pel Freeze; made in sheep, 1:500) (see (Stamatakis and Stuber, 2012; van Zessen et al., 2012) for additional information). Brain sections were mounted, coverslipped, and z-stack and tiled images were captured on a Zeiss LSM 710 confocal

microscope using a 20x or 63x objective. To determine optical fiber placement, tissue was imaged at 10x and 20x on an upright epi-fluorescent microscope.

In vivo anesthetized electrophysiology

C57BL/6J mice were bilaterally injected with 0.3 μ l of AAV5-CaMKIIa-ChR2-eYFP into the vBNST. 6 weeks following virus injection, mice were anesthetized with 0.5 – 1.0% isoflurane (Butler Schein) and were placed into a stereotaxic frame (Kopf Instruments). Body temperature was maintained at $\sim 37^{\circ}\text{C}$ with a homeothermic heating blanket (Harvard Apparatus, Holliston, MA). Tail pinches were administered frequently to monitor responses under anesthesia. A reference electrode was fixed inside brain tissue, approximately 2 mm from both the vBNST and VTA. Extracellular neural activity was recorded using a glass recording electrode (5 - 10 $\text{M}\Omega$: and filled with 0.5 M NaCl). The recording electrode was lowered into the vBNST (+ 0.14 mm to bregma, +/- 0.9 lateral to midline, and - 4.8 mm ventral to the skull surface) by a motorized micromanipulator (Scientifica). Recordings were amplified (Multiclamp 700B, Molecular Devices), highpass filtered at 6 kHz and sampled at 10 kHz.

For orthodromic activation, an optical fiber coupled to a solid state laser (473 nm) was fed through the side port of the electrode holder to terminate near the tip of the glass recording electrode, which allowed for delivery of ~ 5 mW light pulses into the vBNST. For antidromic activation, an optical fiber housed in a steel cannula and coupled to a separate solid state laser (473 nm) was inserted into the VTA at a 16° angle (- 3.2 mm to bregma, + 1.4 mm lateral to midline, and - 4.9 mm ventral to the skull surface), which delivered ~ 10 mW of light to the VTA. vBNST neurons were classified as antidromic-responsive, if the following 3 criteria were met: 1) stable antidromic spike latency (< 0.2 ms), 2) ability to respond reliably to high frequency photostimulation, 3) collision between orthodromic- and antidromic-evoked spikes. Each photostimulation parameter delivered a 5 ms light pulse to either vBNST cell bodies (orthodromic) or vBNST axons within the VTA (antidromic). To determine stable antidromic

latencies, 5 ms light pulses were delivered to the VTA every 5 s for 20 trials. To confirm reliable antidromic spike fidelity, 20, 40, and 100 Hz train pulses of light were delivered to the VTA every 10 s for 10 trials at each frequency. To validate spike collision, we varied the collision interval (0, 1, 2, 5, 10, 20 ms) between orthodromic and antidromic photostimulation. Each collision interval was repeated every 5 s for a total of 10 trials. Data acquisition and analysis was performed using pCLAMP software (Molecular Devices). Placements of recording electrode tips within the vBNST and optical fibers within the VTA were verified with histological examination of brain tissue following the experiments.

Patch-clamp electrophysiology

Brain slices preparation and general methods for patch-clamp electrophysiology were conducted as previously described (Stamatakis and Stuber, 2012; Stuber et al., 2011; van Zessen et al., 2012), with the following changes. To examine both vBNST postsynaptic glutamatergic and GABAergic currents, C57BL/6J mice were injected with AAV5-CaMKIIa-ChR2-eYFP to nonspecifically target vBNST→VTA projection neurons (CaMKIIa^{vBNST→VTA}::ChR2). For whole-cell voltage recordings (EPSCs and IPSCs) from VTA neurons, electrodes (2-4 MΩ electrode resistance) contained in mM: 117 cesium methanesulfonate, 20 HEPES, 0.4 EGTA, 2.8 NaCl, 5 TEA, 2 Mg-ATP, 0.2 Na-GTP (pH 7.2-7.4), 275-285 mOsm. The cesium methanesulfonate internal solution also contained the selective NMDA antagonist, MK-801 (1.125 mM). VTA neurons were held at $V_h = -70\text{mV}$ (E_{REV} for GABA_A receptors) and $V_h = +10\text{ mV}$ (E_{REV} for AMPA receptors) to examine both glutamatergic and GABAergic postsynaptic currents respectively within the same neuron. Photostimulation (5 ms pulses of 1 - 2 mW, 473 nm light delivery via LED through a 40x microscope objective) was used at both voltages. In a subset of neurons ($n = 4$ of 11 neurons), TTX (1 μM) and 4-AP (1 mM) was bath applied to isolate monosynaptic currents. To isolate vBNST glutamatergic and GABAergic postsynaptic currents, *Vglut2*^{vBNST→VTA}::ChR2 and

Vgat^{vBNST→VTA::ChR2} mice were used for recordings. For whole-cell voltage clamp recordings of VTA EPSCs from *Vglut*^{vBNST→VTA::ChR2} mice, once stable light-evoked EPSCs were achieved, 10 μM DNQX was bath applied. For whole-cell voltage clamp recordings of VTA IPSCs from *Vgat*^{vBNST→VTA::ChR2} mice, once stable light-evoked IPSCs were achieved, 10 μM Gabazine was bath applied.

Ex vivo validation of photoinhibition of VTA GABA neurons

For current clamp recordings to show hyperpolarization of membrane voltage from VTA GABA neurons following NpHR3.0 inhibition, *Vgat*-ires-cre mice were transduced with Cre-inducible NpHR3.0 under control of the EF1α promoter in the VTA. Electrodes (2-4 MΩ) contained in mM: 130 K-gluconate, 10 KCl, 10 HEPES, 10 EGTA, 2 MgCl₂, 2 Mg-ATP, 0.2 Na-GTP (pH 7.2-7.4), 275-285 mOsm. VTA neurons were maintained at ~ -60 mV. For photoinhibition, 500 ms pulses of 5 - 8 mW, 532 nm light delivery via a solid-state laser coupled to an optical fiber positioned in the brain slice.

Unpredictable foot-shock paradigm

Mice were placed in sound-attenuated mouse behavioral chambers (Med Associates) where an unpredictable foot shock was used as an aversive stimulus. A houselight and white noise signaled the start of the trial and remained on throughout the entire 20 min foot-shock session (contextual cues). Each unpredictable foot shock was 0.75 mA in intensity and 500 ms in duration on a variable interval (VI60) schedule. Mice received approximately 20 unpredictable foot shocks during the entire 20 min session.

For the *in vivo* electrophysiology experiments, *Vglut*^{vBNST→VTA::ChR2} and *Vgat*^{vBNST→VTA::ChR2} mice implanted with a MEA in the vBNST and an optical fiber in the VTA were placed in the unpredictable foot-shock context where they received the visual and auditory contextual cues in the absence of foot shock for 20 min (contextual cue exposure prior to shock

association). Five days after the unpaired contextual cue session, mice were run in the standard unpredictable foot-shock session (approx. 20 unpredictable foot shocks, 0.75 mA, 500 ms) for 5 consecutive days as stated above, which included paired presentation of the contextual cues. Seven days following the 5th unpredictable foot-shock session, mice were placed back into the unpredictable foot-shock paradigm, where they received the visual and auditory contextual cues (housetlight and white noise) in the absence of foot shock for 20 min.

In vivo electrophysiology

Neural activity was recorded using an Omniplex recording system (Plexon Instruments). Signals from each electrode in the array were referenced to ground, and recordings were performed in differential mode to subtract artifacts unrelated to neural activity. Acquired data was bandpass filtered between 0.1 and 8,000 Hz. Spike sorting was performed offline using Offline sorter (Plexon Instruments), as previously described (Roitman et al., 2005). Briefly, discrimination of individual units was performed offline using principal component analysis to separate individual units from the same electrode. In addition, auto- and cross-correlograms, firing characteristics, and inter-spike interval distributions were examined to ensure units were well-isolated. In addition, timestamp data to signify the start and end of foot-shock sessions, and the delivery of light pulses to optical fibers was synchronized with electrophysiological data. Sorted waveforms were further processed in NeuroExplorer (Nex Technologies) to extract unit timestamps and relevant events. NeuroExplorer-extracted timestamps were exported to MATLAB and further data processing and statistical testing. Neuronal units were included in the data if the signal-to-noise ratio was high, and the mean firing rate was between 0.5 – 25 Hz during baseline recording periods. During the time epoch surrounding the individual delivered foot shocks, large shock artifact were readily apparent. While these were easily isolated and excluded from the analyzed waveform data using offline spike sorting, neuronal firing responses in the 500 – 1000 ms following foot shock onset could not be reliably quantified. Thus, data

collected during these time epochs were excluded from analysis. This represents an approximate loss of 0.8 – 1.66% of the collected data during the foot-shock session. Resulting data was binned in 30 s epochs in order to minimize the skewing of our results due to data lost by the shock artifacts. In addition, recording sites was verified histologically using electrolytic lesions at 200 μ A for 5 s.

To identify units originating from vBNST projection neurons, 5 ms light pulses were delivered to VTA to antidromically stimulate vBNST projection neurons that innervated the area. Light pulses were delivered in 10 s intervals for 20 trials starting 40 min after the end of the unpredictable foot-shock session. Recorded vBNST units were classified as light-responsive, and thus VTA-projecting, if they met both of the following two criteria. 1) The latency of the first spike after light stimulation onset was less than 20 ms for $\geq 20\%$ of the trials. 2) Light-evoked and spontaneous waveform shapes had a correlation coefficient of > 0.90 . To compare light-evoked and spontaneous waveforms from units, light-evoked waveform characteristics were defined using the average waveform shape and average principal component values (PC1-3) of the first spike following photostimulation onset from each successful trial where a waveform was collected within 20 ms after light onset. This subset of light-evoked waveforms were then averaged together for a given unit, and compared to a subset of spontaneous, non-light-evoked waveforms that occurred immediately preceding the onset of light stimulations (pre-stimulation waveforms) and the first collected waveforms occurring after the 20 ms interval following the offset of photostimulations (post-stimulation waveforms). The correlation between each average waveform shape over the three time epochs (pre-stimulation, during stimulation, post-stimulation) was then calculated using Pearson's product-moment coefficient as well as their average principle component values.

VTA-projecting vBNST neuronal units were then further classified, dependent on their firing response to the foot shock session into 3 categories: foot-shock session-excited, foot-

shock session-inhibited and foot-shock session-no effect. To clarify, foot-shock session-excited, foot-shock session-inhibited, and foot-shock session-no effect refers to a neural unit's activity in response to the collective aversive experience, not to individual foot shocks. To assess the firing rate of a particular neuron, each spike from 10 min preceding the foot shock session to 20 min following the end of the foot shock session was binned into 30 s bins. Firing rate was then normalized to the mean firing rate during the 10 min preceding the start of the 20 min foot-shock session using z-scores. Neurons were classified as foot-shock session-excited if their average z-score during the 20-min foot-shock session was greater than 1. Likewise, neurons were classified as foot-shock session-inhibited if their average z-score during the shock session fell below -1. All other units where the z-score did not exceed an absolute value of 1 during the 20 min foot-shock session were classified as no effect. Neural activity was recorded from the same mice during the cue exposure, foot shock, and cue re-exposure sessions, therefore we were able to reliably record activity from the same population of neurons during each of the three sessions.

Photostimulation of $Vglut2^{vBNST \rightarrow VTA}::ChR2$ and $Vgat^{vBNST \rightarrow VTA}::ChR2$ projections and photoinhibition of $Vgat^{VTA}::NpHR$ neurons during real-time place preference

$Vglut2^{vBNST \rightarrow VTA}::ChR2$, $Vgat^{vBNST \rightarrow VTA}::ChR2$, $Vgat^{VTA}::NpHR$, and litter mate controls were implanted with optical fibers above the VTA and were run in the real-time place preference paradigm. See (Stamatakis and Stuber, 2012) for additional details on this method.

Intra-VTA injection of antagonists and photostimulation of $Vglut2^{vBNST \rightarrow VTA}::ChR2$ and $Vgat^{vBNST \rightarrow VTA}::ChR2$ projections during real-time place preference

A separate cohort of $Vglut2^{vBNST \rightarrow VTA}::ChR2$ and $Vgat^{vBNST \rightarrow VTA}::ChR2$ mice were unilaterally implanted with a 26-gauge cannula coupled to an optical fiber aimed above the VTA. All mice were placed in a custom-made place preference arena and were run in the real-time place preference paradigm to achieve a baseline measurement. Two days following the

baseline session, *Vglut2*^{vBNST→VTA}::ChR2 mice were injected with either 0.3 μl of vehicle (saline) or a cocktail of selective glutamate antagonists (0.1 μg AP-5/0.001 μg DNQX in saline) and *Vgat*^{vBNST→VTA}::ChR2 mice were injected with either 0.3 μl of vehicle (saline) or a selective GABA_A antagonist (0.001 μg Gabazine) into the VTA in a counter balanced design (all drugs from Tocris). The injector needle (33 gauge steel tube, McMasters-Carr) extended approximately 1 mm past the cannula to ensure drug delivery 0.5 mm below the optical fiber. All mice were infused at a rate of 0.1 μl per minute. The injector remained in place for approximately 2 min following infusion to ensure proper diffusion of drug into the VTA. Immediately following the microinjection procedure, all mice were placed into the real-time place preference chamber. Mice had 2 days off between each VTA microinjection.

Photostimulation of *Vglut2*^{vBNST→VTA}::ChR2 projections during open-field testing

Vglut2^{vBNST→VTA}::ChR2 and *Vglut2*^{vBNST→VTA}::Control mice were examined in a custom made open field arena (25 x 25 x 25 cm white plexiglass arena) for 35 min. After a baseline period of 5 min, all mice received constant 20 Hz photostimulation. Immediately, following the 20 min photostimulation epoch, all mice had a 10 min period in which they received no photostimulation. Center zone was defined as the center 156 cm² (25% of the entire arena). Corner zones were defined as the 39 cm² in each corner. The 35 min session was recorded with a CCD camera that was interfaced with Ethovision software (Noldus Information Technologies). Time spent in the corner and the center of the open-field apparatus was recorded. Heat maps and post-acquisition processing were conducted in MATLAB (Mathworks Inc.).

Photostimulation of *Vglut2*^{vBNST→VTA}::ChR2 projections during sucrose self-administration

Vglut2^{vBNST→VTA}::ChR2 and *Vglut2*^{vBNST→VTA}::Control mice with optical fibers implanted above the VTA were first food restricted to 90% of their free-feeding weight. They were then

placed in standard mouse operant chambers in order to nose poke for a 15% (w/v) sucrose solution on a fixed ratio (FR-1) schedule in a 30 min session. Once stable nose-poking behavior for 15% sucrose was observed (approximately 100 active nose pokes on at least 2 consecutive days), all mice received constant 20 Hz photostimulation during the entire 30 min sucrose session.

Optical self-stimulation of $Vgat^{vBNST \rightarrow VTA}::ChR2$ projections

$Vgat^{vBNST \rightarrow VTA}::ChR2$ and $Vgat^{vBNST \rightarrow VTA}::Control$ mice with optical fibers implanted above the VTA were trained in one 30 min session to nose poke on a fixed ratio (FR-1) schedule for optical self-stimulation of the $Vgat^{vBNST \rightarrow VTA}::ChR2$ projections in standard mouse operant chambers (Med Associates). Each nose poke resulted in a single 3 s 20 Hz optical pulse train. Following the 1 day 20 Hz training session, mice were run daily at each photostimulation frequency (1, 5, 10, 20, 40 Hz) in a counter-balanced design.

Optical self-inhibition of $Vgat^{VTA}::NpHR$ neurons

$Vgat^{VTA}::NpHR$ and $Vgat^{VTA}::Control$ mice with optical fibers implanted above the VTA were trained in one 30 min session to nose poke on a FR1 schedule for 3-s constant photoinhibition of VTA GABAergic cell bodies in standard mouse operant chambers as described above (Med Associates).

Photostimulation of $Vgat^{vBNST \rightarrow VTA}::ChR2$ projections and photoinhibition of $Vgat^{VTA}::NpHR$ neurons during the elevated plus maze

$Vgat^{vBNST \rightarrow VTA}::ChR2$, $Vgat^{VTA}::NpHR$, $Vgat^{VTA}::Control$, and $Vgat^{vBNST \rightarrow VTA}::Control$ mice were run in the elevated plus maze (EPM) to assay anxiety-like behavior. Activity and location was recorded for 5 min (baseline). Following this 5 min baseline period, $Vgat^{vBNST \rightarrow VTA}::ChR2$ and $Vgat^{vBNST \rightarrow VTA}::Control$ mice received constant 20 Hz photostimulation for 5 min, while $Vgat^{VTA}::NpHR$ and $Vgat^{VTA}::Control$ mice received constant inhibition for 5 min. Immediately

following the 5 min photostimulation or photoinhibition epoch, all mice had a 5 min period in which they received no light delivery.

Photostimulation of $Vgat^{vBNST \rightarrow VTA}::ChR2$ projections during foot-shock followed by freezing and anxiety-like behavior measurements

$Vgat^{vBNST \rightarrow VTA}::ChR2$ and $Vgat^{vBNST \rightarrow VTA}::Control$ mice with optical fibers implanted above the VTA were run in a modified foot-shock paradigm as described above. Briefly, mice were placed into sound attenuated mouse chambers (Med Associates) for a 5 min baseline period. After the 5 min baseline period, a house light and white noise were activated and mice received the same foot shock protocol as described above. Additionally, during the 20 min shock session, all mice received constant 20 Hz photostimulation. A separate cohort of mice ($Vgat^{vBNST \rightarrow VT}::ChR2$ and $Vgat^{vBNST \rightarrow VT}::Control$) received constant 20 Hz photostimulation of this pathway in the absence of foot shock. Immediately following the 20 min foot shock and photostimulation epoch, all mice had a 5 min period in which they received no foot shock or photostimulation while still exposed to contextual cues, to assay freezing behavior. Freezing was defined as the total lack of any movement, except respiration for a period of 2 s. The 30 min test session was recorded with a CCD camera that was interfaced with Ethovision software (Noldus Information Technologies). Time frozen during the 5 min period immediately following the foot shock and photostimulation session was recorded. Approximately 3 hr after the foot shock and photostimulation session or just the photostimulation session in the absence of foot shock, mice were run on the elevated-plus maze to assay anxiety-like behavior for 5 min.

Results

Optogenetic identification of $vBNST \rightarrow VTA$ projection neurons

The ventral BNST (vBNST) is a heterogeneous structure (Hammack et al., 2007) that innervates the VTA (Dong and Swanson, 2004; Dumont and Williams, 2004; Geisler and Zahm,

2005; Jalabert et al., 2009; Kudo et al., 2012), and aversive and rewarding stimuli activate a subset of these vBNST projection neurons (Briand et al., 2010; Christianson et al., 2011; Mahler and Aston-Jones, 2012). To identify and record the activity of vBNST→VTA neurons using antidromic photostimulation *in vivo*, we targeted channelrhodopsin-2 fused to enhanced yellow fluorescent protein (ChR2–eYFP) (Boyden et al., 2005) under the control of a CaMKII α promoter to the vBNST of adult mice. After 4–6 weeks, ChR2–eYFP was observed in vBNST cell bodies and projection fibres that innervate the VTA (**Figure 2.1 A**). Under anaesthesia, optical fibres for antidromic photostimulation were positioned above the VTA, whereas recording electrodes and optical fibres for orthodromic photostimulation were positioned in the vBNST (**Figure 2.1 B**). We recorded from vBNST units that showed reliable spiking to both orthodromic and antidromic photostimulation. By systematically decreasing the interval between orthodromic and antidromic photostimulation, the fidelity of antidromic spikes was significantly attenuated (**Figures 2.1 C and D**), demonstrating spike collision (Fuller and Schlag, 1976). In addition, antidromic spike latencies were significantly greater and showed less variability than orthodromic spikes (**Figures 2.1E and F**), and antidromic spike fidelity was significantly greater than orthodromic spike fidelity to 40-Hz photostimulation (**Figure 2.1 G**). Thus, photostimulation of vBNST→VTA projections results in antidromic spiking that is reliably distinguishable from putative transsynaptic circuit activation.

To examine the neurophysiological dynamics of identified vBNST→VTA neurons in behaving mice, we implanted 16-channel multielectrode arrays in the vBNST, as well as optical fibres above the VTA for antidromic identification of neurons (Sparta et al., 2012) (**Figure 2.1 H and Figures 2.2 A and B**). Delivery of single 5-ms, 473-nm light pulses to the VTA resulted in time-locked firing in many vBNST neurons. Photostimulation of vBNST→VTA fibres resulted in a bimodal firing pattern in vBNST neurons due to distinguishable antidromic and polysynaptic activity (**Figure 2.2C**). Principle component and correlation analysis comparing waveform

shapes demonstrated that spontaneous waveforms were highly correlated with light-evoked waveforms 7 (average $r = 0.950 \pm 0.008$ (mean \pm s.e.m.) (**Figures 2.2 D and E**). Light-evoked spike latencies showed that a subset of recorded units consistently displayed time-locked spiking on 11.21 ± 0.68 out of 20 trials (56%), with a mean latency of 7.31 ± 0.32 ms (**Figures 2.1 I and J**), comparable with our anaesthetized recording data (**Figure 2.1 E**) and a previous study using electrical antidromic stimulation of BNST projections in rodents (Nagy and Paré, 2008). Accordingly, neurons that were identified as antidromic-responsive displayed a spike fidelity of $81 \pm 15\%$ in response to 20-Hz photostimulation (**Figure 2.2 F**). Using these criteria, we identified 53 out of 137 units as vBNST→VTA projection neurons.

vBNST neurons display heterogeneous responses to aversive stimuli exposure (Briand et al., 2010; Christianson et al., 2011). Thus, we classified the firing patterns of identified vBNST→VTA neurons in response to unpredictable foot shocks and associated contextual cues. Identified vBNST→VTA neurons segregated into three functionally distinct classes based on changes in their normalized firing rates throughout the foot-shock session (**Figures 2.3 A and B**), demonstrating that vBNST→VTA neurons differentially encode information related to aversive stimuli and their associated contextual cues.

Electrical stimulation of the BNST produces both excitatory and inhibitory responses in VTA neurons *in vivo* (Georges and Aston-Jones, 2001), suggesting that distinct subcircuits may exist. Mice were injected with adeno-associated viral vector (AAV5) expressing ChR2–eYFP under the control of the CaMKII α promoter (AAV5:CaMKII α ::ChR2–eYFP) to nonspecifically target vBNST→VTA projection neurons (CaMKII α ^{vBNST→VTA}::ChR2). Whole-cell recordings in brain slices revealed that photostimulation of the CaMKII α ^{vBNST→VTA} pathway produced both glutamatergic and GABAergic currents in VTA neurons (**Figure 2.4**), demonstrating that neurochemically distinct vBNST neurons project to the VTA.

Excitatory and inhibitory synapses onto non-dopaminergic VTA neurons from neurochemically distinct vBNST neurons

We next dissected the functional connectivity between distinct glutamatergic and GABAergic vBNST→VTA neurons and their genetically defined postsynaptic targets within the VTA. Injection of a Cre-inducible viral construct coding for ChR2–eYFP into the vBNST in *Vglut2-ires-cre* or *Vgat-ires-cre* mouse lines (which express Cre recombinase from the endogenous *Vglut2* (also known as *Slc17a6*) or *Vgat* (*Slc32a1*) promoters, respectively) (Vong et al., 2011) resulted in robust expression in the vBNST as well as in fibres originating from these neurons that innervated the VTA (**Figures 2.5 A and B**). Whole-cell recordings from VTA neurons revealed that photostimulation of ChR2-containing fibres originating from vBNST neurons expressing *Vglut2* (*Vglut2*^{vBNST→VTA::ChR2}) or *Vgat* (*Vgat*^{vBNST→VTA::ChR2}) produced excitatory or inhibitory postsynaptic currents, respectively (**Figures 2.5 C and D**).

Vglut2^{vBNST→VTA} and *Vgat*^{vBNST→VTA} terminals formed functional synapses primarily onto non-dopaminergic and medially located dopaminergic neurons, which have been implicated in responding to aversive stimuli (Cohen et al., 2012; Lammel et al., 2012; Tan et al., 2012; van Zessen et al., 2012) (**Figures 2.5 E and F and Figure 2.6**). These data provide a circuit blueprint by which vBNST subcircuits interact with VTA-reward circuitry.

***Vglut2*^{vBNST→VTA} and *Vgat*^{vBNST→VTA} projection neurons display distinct firing patterns in response to foot-shock and shock-associated contextual cues**

We next explored whether glutamatergic or GABAergic subpopulations of vBNST→VTA neurons differentially respond to foot-shock sessions and associated contextual cues. Using optical antidromic activation *in vivo*, we identified 34 *Vglut2*^{vBNST→VTA::ChR2}-expressing neurons out of 145 recorded neurons. Although all projection neurons displayed heterogeneous firing patterns, identified *Vglut2*^{vBNST→VTA} projection neurons exhibited a net enhancement of firing during the aversive event (**Figures 2.7 A and B**). By contrast, 33 identified

Vgat^{vBNST→VTA::ChR2}-expressing neurons out of 77 total neurons principally exhibited reduced firing during the aversive event (**Figures 2.7 C and D**). In addition, 1 week after five consecutive daily foot-shock sessions, re-exposure to shock-associated contextual cues alone resulted in a net enhancement of *Vglut2*^{vBNST→VTA::ChR2} neuronal activity (**Figures 2.7 E and F**), whereas the activity of *Vgat*^{vBNST→VTA::ChR2} neurons was largely suppressed (**Figures 2.7 G and H**). Collectively, exposure to the aversive event or associated cues alone enhanced the firing of *Vglut2*^{vBNST→VTA} neurons, while simultaneously suppressing the activity of *Vgat*^{vBNST→VTA} neurons.

Photostimulation of the *Vglut2*^{vBNST→VTA} pathway promotes aversion and anxiety

Because aversive stimuli enhanced the activity of *Vglut2*^{vBNST→VTA} neurons (**Figures 2.7 A and B**), which can excite non-dopaminergic VTA neurons (**Figure 2.5 E**), we next explored the behavioural consequences of selectively activating this projection in behaving mice. We tested mice in a real-time place preference (RTPP) model to assay the effects of photostimulation of the *Vglut2*^{vBNST→VTA} pathway on motivational valence. Photostimulation of *Vglut2*^{vBNST→VTA::ChR2} mice resulted in a significant avoidance of a stimulation-paired chamber (**Figures 2.8 A and B**). The aversive effects of this stimulation was dependent on local VTA glutamatergic signalling as infusions of an ionotropic glutamate receptor antagonist cocktail abolished the aversive phenotype induced by *Vglut2*^{vBNST→VTA} activation (**Figure 2.8 B**). Activation of this pathway also reduced active reward seeking (**Figures 2.8 C and D**). In addition, inescapable activation of this pathway for 20 min in an open field resulted in significantly less centre and more corner time in *Vglut2*^{vBNST→VTA::ChR2} mice in the 10 min after stimulation offset compared to controls, suggesting that enhanced activity in the *Vglut2*^{vBNST→VTA} pathway contributes to anxiety-like behaviour (**Figure 2.8 E**).

Photostimulation of the $Vgat^{vBNST-VTA}$ pathway and inhibition of $Vgat^{VTA}$ neurons produces reward-related behaviours and attenuates anxiety

In contrast to the aversive consequences of stimulating the $Vglut2^{vBNST-VTA}$ pathway, 20-Hz photostimulation in $Vgat^{vBNST-VTA::ChR2}$ mice resulted in a significant place preference (**Figures 2.9 A and B**). VTA infusions of a GABA_A receptor antagonist prevented the $Vgat^{vBNST-VTA}$ -mediated place preference compared to saline injections (**Figure 2.9 B**). To determine whether *in vivo* optogenetic activation of the $Vgat^{vBNST-VTA}$ pathway produces active reward seeking, we tested whether these mice would nose poke to receive photostimulation (Stuber et al., 2011). $Vgat^{vBNST-VTA::ChR2}$ mice readily nose poked to receive photostimulation (**Figure 2.9 C**). Together, these data suggest that photostimulation of the $Vgat^{vBNST-VTA}$ pathway promotes reward-related behaviours.

Because the $Vgat^{vBNST-VTA}$ projection preferentially innervates non-dopaminergic VTA neurons (**Figure 2.5 F**), we considered VTA GABAergic neurons as the likely postsynaptic target. VTA GABAergic neuronal inhibition via halorhodopsin activation with enhanced Natronomonas pharaonis halorhodopsin (eNpHR3.0) also produced reward-related phenotypes ($Vgat^{vBNST-VTA::eNpHR3.0}$; **Figures 2.9 D-I**). Together, these results show that reward-related responses to $Vgat^{vBNST-VTA}$ activation are recapitulated by directly inhibiting $Vgat^{VTA}$ neurons, thus providing a circuit mechanism for the $Vgat^{vBNST-VTA}$ pathway to regulate motivated behaviour.

As the BNST regulates the expression of fear and anxiety-related behavioural phenotypes (Davis et al., 2010; Erb et al., 2001; Poulos et al., 2010), we also sought to establish a role for the $Vgat^{vBNST-VTA}$ pathway in these negative motivational states. Photostimulation of the $Vgat^{vBNST-VTA}$ pathway and direct inhibition of $Vgat^{VTA}$ neurons significantly increased the time spent in the open arms of an elevated-plus maze (EPM) test, indicative of anxiolysis (**Figures 2.10 A-D**). These coinciding observations suggest that

$Vgat^{vBNST \rightarrow VTA}$ and $Vgat^{VTA}$ neurons act as crucial circuit nodes for moderating the expression of anxiety.

Discussion

Given that $Vgat^{vBNST \rightarrow VTA}$ neurons are largely inhibited by aversive stimuli (**Figures 2.7 C and D**), we examined whether concurrent activation of the $Vgat^{vBNST \rightarrow VTA}$ projection during an unpredictable foot-shock session could alleviate the subsequent development of anxiety-like behavior. Immediately after termination of the foot-shock session and cessation of $Vgat^{vBNST \rightarrow VTA}::ChR2$ stimulation, we measured the acute freezing response while mice were still in the shock-associated context, as well as their behaviour in the EPM test 3 h later (**Figure 2.7 E**). $Vgat^{vBNST \rightarrow VTA}::ChR2$ mice displayed significantly more open-arm time and entries in the EPM test relative to controls (**Figures 2.7 F and G**). Taken together, these data suggest that enhancing activity of the $Vgat^{vBNST \rightarrow VTA}$ pathway during aversive stimuli exposure has anxiety-buffering properties. Although the canonical view of BNST function proposes a dominant role of this structure in promoting anxiety states (Davis et al., 2010; Phelps and LeDoux, 2005; Walker and Davis, 2008), the cellular and functional complexity described here illustrates that particular BNST circuit elements orchestrate divergent aspects of emotional and motivational processing.

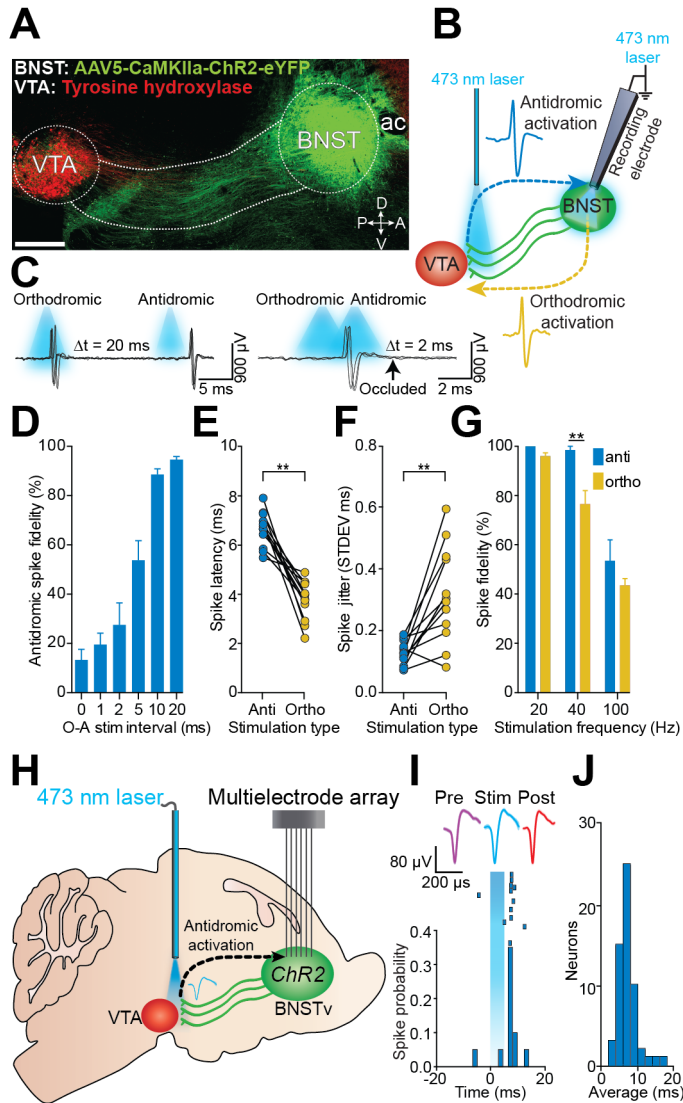


Figure 2.1: Optogenetic identification of vBNST→VTA projection neurons. **A.** Sagittal image showing the vBNST→VTA projection (ac, anterior commissure; D, dorsal; V, ventral; P, posterior; A, anterior; scale = 500 μ m). **B.** Optogenetic collision test. **C.** Example traces from a single CaMKIIa^{vBNST→VTA} unit demonstrating antidromic-orthodromic spike collision. **D.** Significant reduction in antidromic spike fidelity (%) at short antidromic-orthodromic photostimulation intervals (O, orthodromic photostimulation; A, antidromic photostimulation; $F_{5,65} = 48.63$, $P < 0.0001$; $n = 12$ units). **E.** Antidromic spike latencies were significantly greater than orthodromic latencies ($P < 0.0001$; $n = 12$ units). **F.** Antidromic-initiated spikes displayed

significantly greater latency stability compared to orthodromic-activated spikes ($P < 0.001$; $n = 12$ units). **G.** Antidromic spikes responded more reliably to 40 Hz photostimulation compared to orthodromic spikes ($F_{2,18} = 11.2$, $P = 0.003$, $n = 4$ units). **H.** Optogenetic identification of BNSTv→VTA projection neurons in behaving mice. **I.** Representative peri-event histogram and raster of a single unit timelocked to 5 ms antidromic photostimulation. **J.** Mean first-spike latencies following antidromic photostimulation for all identified CaMKIIa^{BNSTv→VTA} projection neurons ($n = 53$ units, $n = 7$ mice). All values for all figures represent mean \pm s.e.m. * $P < 0.05$, ** $P < 0.01$.

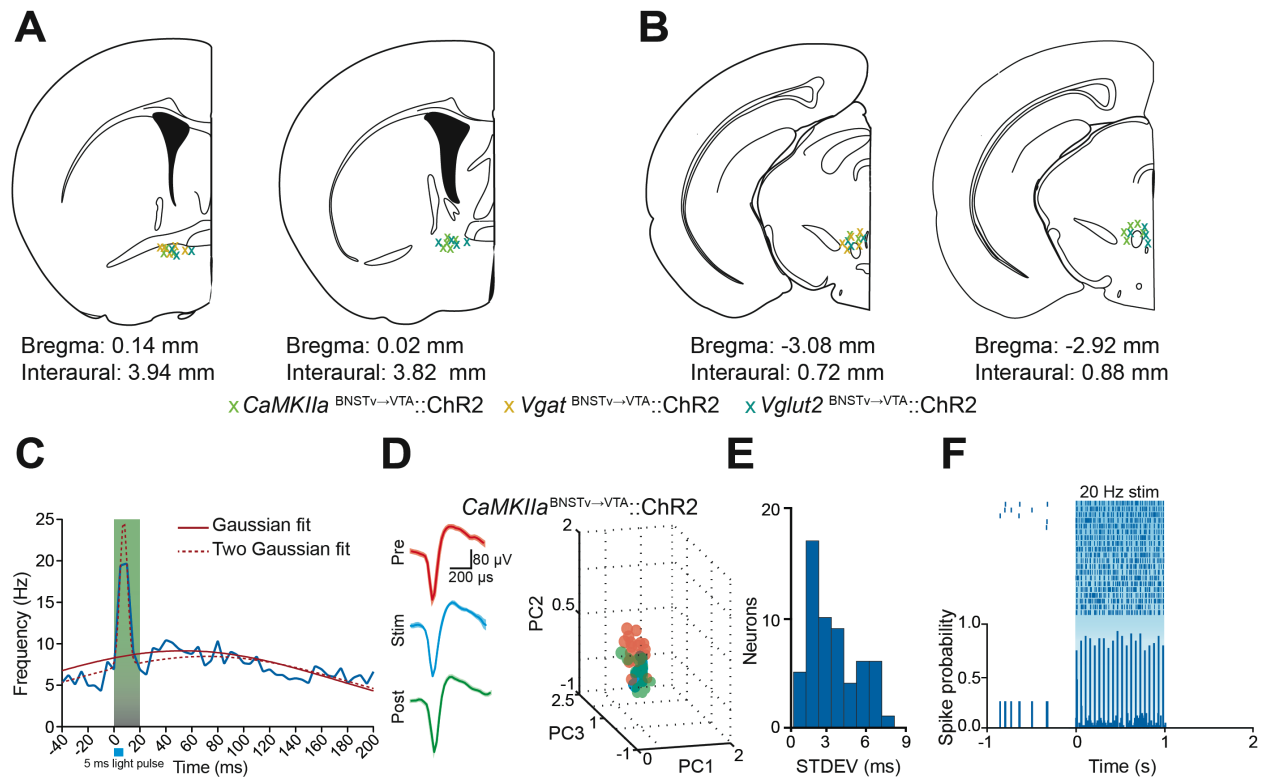


Figure 2.2: Optogenetic identification of $CaMKIIa^{BNSTv \rightarrow VTA}$ projection neurons in freely

moving mice. A-B. Location of multi-electrode arrays within the vBNST (**A**) and optical fibers within the VTA (**B**) based on histological examination of brain tissue following the experiments.

C. Kolmogorov-Smirnov test for goodness of fit revealed the spike rate following antidromic photostimulation was not normally distributed ($P < 0.0001$; $n = 53$ units). Consistent with this, the data did not reliably fit a Gaussian distribution ($R^2 = 0.2025$), but was better encapsulated by a bimodal distribution using a sum of two Gaussian fit ($R^2 = 0.8510$). The two Gaussian model revealed distinct peaks in the fitted data occurring at $t = 7.54$ ms and $t = 70.55$ ms after the photostimulation onset. The peak occurring at 7.54 ms is indicative of antidromic

photostimulation, while the latter peak could represent transynaptic activity. **D.** Photostimulation does not alter recorded waveform shape during freely moving recordings ($n = 53$ units, $n = 7$ mice; PC: principle components, colored circles indicate waveform recorded during pre, during, or post stimulation epochs). **E.** Standard deviation (STDEV) spike latency after photostimulation

for all identified projection neurons shown in Figure 1J. **F.** Representative peri-event histogram and raster of a single unit responding reliably to high frequency antidromic photostimulation (5 ms pulse duration, 20 Hz, 1 s trial duration).

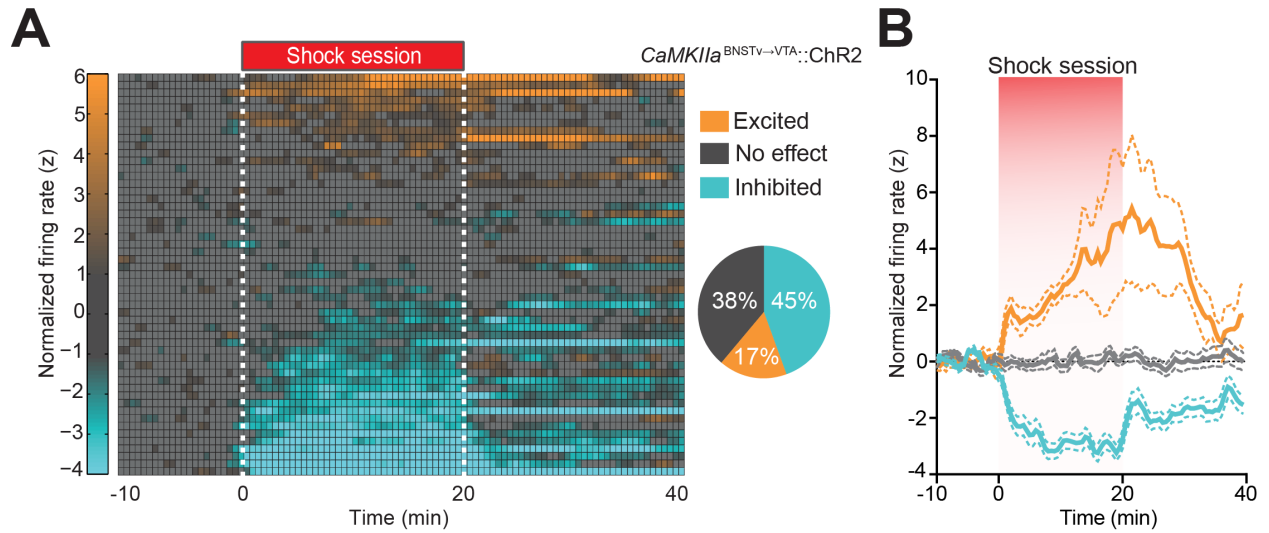


Figure 2.3: vBNST→VTA projection neurons differentially respond to aversive stimuli.

A. Color plot and pie chart showing the normalized firing rates and classifications of all light responsive CaMKIIa^{vBNST→VTA} projection neurons (n = 53) during the foot-shock session. **B.**

Average normalized firing rate of all classified CaMKIIa^{vBNST→VTA} projection neurons are significantly altered during and following the foot-shock session ($F_{200, 5052} = 7.21$, $P < 0.0001$).

All values are \pm s.e.m.

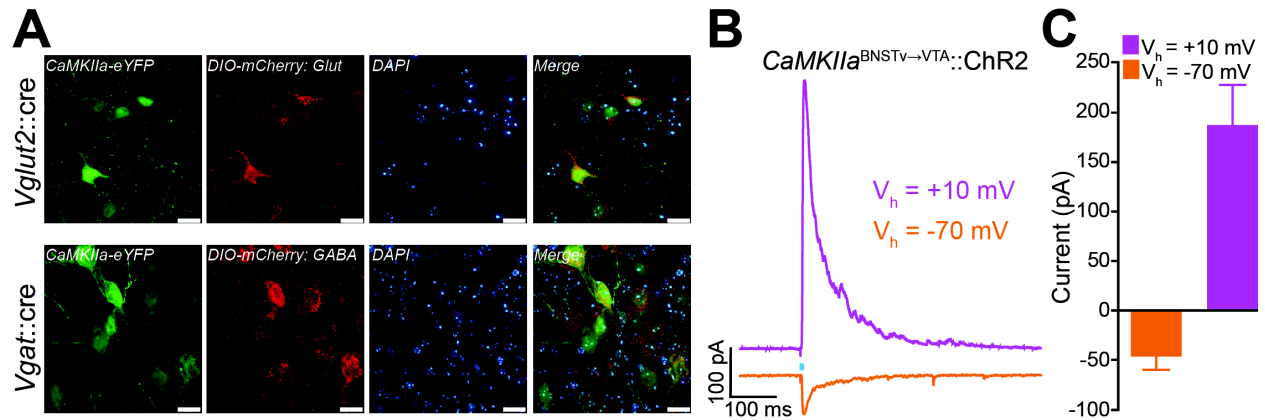


Figure 2.4: Neurochemically distinct vBNST cell types contain CaMKIIa and form functional excitatory and inhibitory synapses onto VTA neurons. A. AAV5-CaMKIIa-eYFP expression in both vBNST-glutamatergic (top) and -GABAergic (bottom) neurons (scale bars = 20 μ m). **B - C.** CaMKIIa^{vBNST→VTA}::ChR2 photostimulation resulted in inward currents at $V_h = -70$ mV and outward currents at $V_h = +10$ mV in VTA neurons (n = 11).

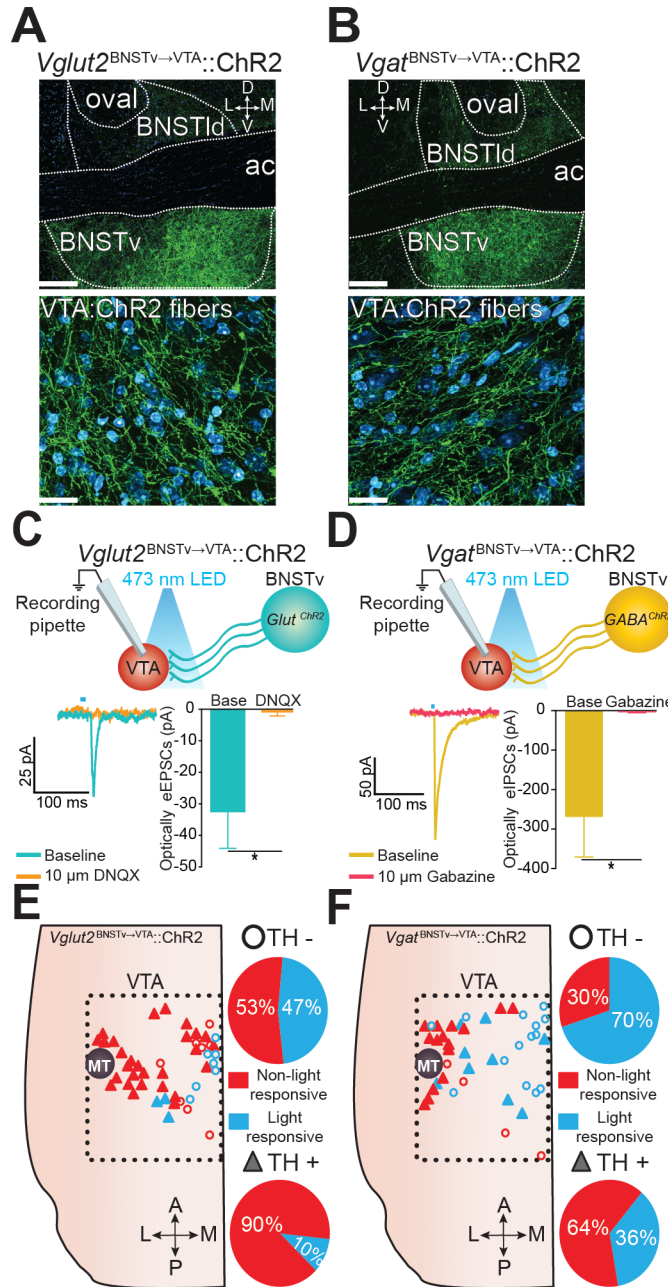


Figure 2.5: Excitatory and inhibitory synapses onto non-dopaminergic VTA neurons from neurochemically distinct vBNST neurons. **A-B.** ChR2–eYFP (green) in the vBNST (top) and fibres in the VTA (bottom) in *Vglut2-ires-cre* (**A**) and *Vgat-ires-cre* (**B**) mice. Cyan denotes fluorescent Nissl stain. Scale bars, 200 μm (top) and 20 μm (bottom). L, lateral; ldBNST, lateral-dorsal BNST; M, medial; oval, oval nucleus BNST. **C.** Optically evoked excitatory postsynaptic currents (eEPSCs) recorded in VTA neurons after *Vglut2*^{vBNST→VTA::ChR2} stimulation before and

after application of the glutamate receptor antagonist 6,7-dinitroquinoxaline-2,3-dione (DNQX) (bottom) (n = 4 cells, P = 0.0307). LED, light-emitting diode. **D.** Optically evoked inhibitory postsynaptic currents (eIPSCs) recorded in VTA neurons after $Vgat^{vBNST \rightarrow VTA}::ChR2$ stimulation before and after application of the GABA_A receptor antagonist gabazine (bottom) (n = 4 cells, P = 0.0378). **E-F.** Location of light-responsive and non-light-responsive dopaminergic and non-dopaminergic neurons in horizontal VTA slices after photostimulation of $Vglut2^{vBNST \rightarrow VTA}::ChR2$ (**E**) and $Vgat^{vBNST \rightarrow VTA}::ChR2$ (**F**) projections. TH, tyrosine hydroxylase. Data are mean \pm s.e.m. *P < 0.05 (Student's t-test for paired samples).

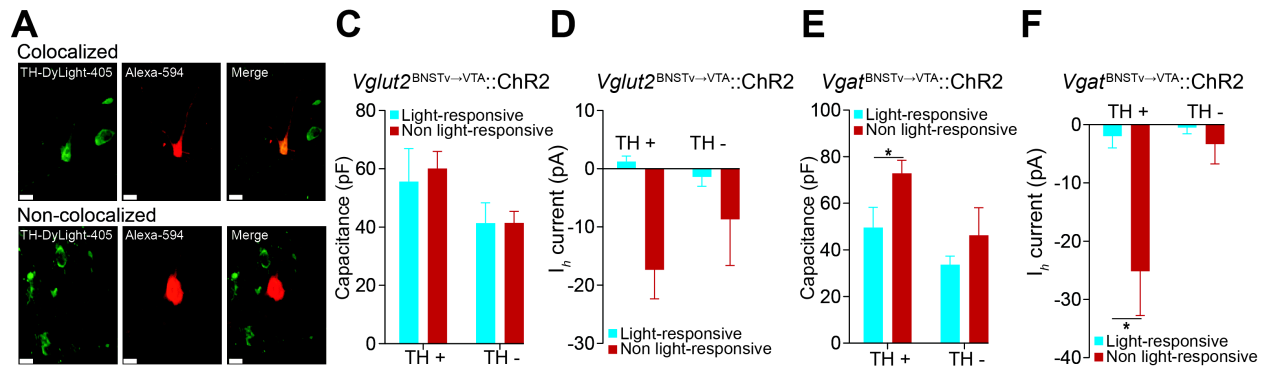


Figure 2.6: *Vglut2*^{vBNST→VTA} and *Vgat*^{vBNST→VTA} terminals synapse onto non-dopaminergic

and I_h negative dopaminergic neurons in the VTA. **A.** Example confocal images of a non

light-responsive TH+, VTA dopaminergic neuron (top) and a light-responsive nondopaminergic

neuron (bottom; scale bars = 20 μ m). **C-F.** Membrane capacitance (pF) and I_h currents (pA)

recorded from light-responsive (n = 3 - 9 cells per group) and non light-responsive (n = 16 - 26

cells per group) VTA dopaminergic neurons and light-responsive (n = 7 - 14 cells per group) and

non light-responsive (n = 6 - 8 cells per group) non-dopaminergic neurons in *Vglut2*^{vBNST→}

VTA::ChR2 and *Vgat*^{vBNST→VTA::ChR2} mice. Whole-cell voltage-clamp recordings from VTA

dopaminergic neurons in *Vgat*^{vBNST→VTA::ChR2} mice show that light-responsive neurons have

significantly lower membrane capacitance (**E**; P = 0.027) as well as significantly lower I_h

currents (**F**; P = 0.034) compared to non light-responsive neurons. All values are \pm s.e.m. * P <

0.05, ** P < 0.01.

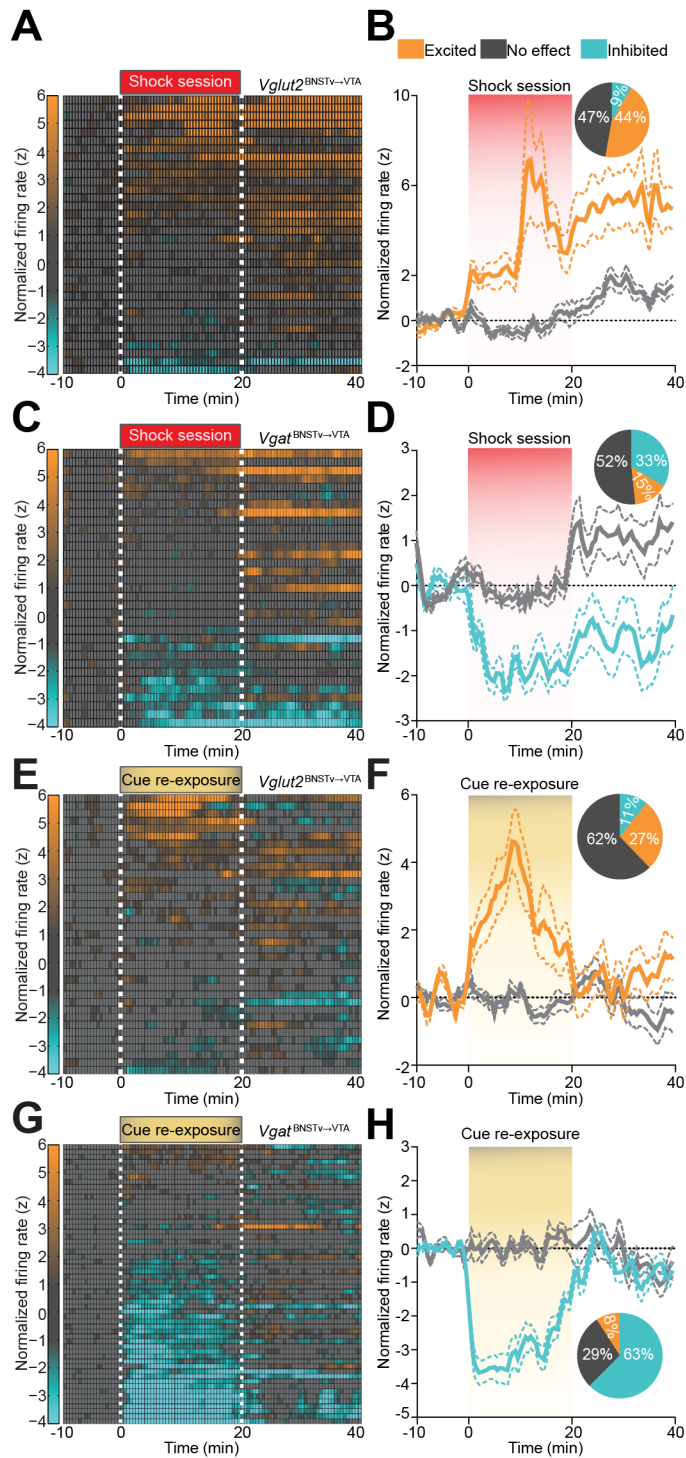


Figure 2.7: $Vglut2^{vBNST \rightarrow VTA}$ and $Vgat^{vBNST \rightarrow VTA}$ projection neurons display distinct firing patterns in response to foot-shock and shock-associated contextual cues. A. Colour-coded normalized firing rates for all identified $Vglut2^{vBNST \rightarrow VTA}$ neurons in response to the first

foot-shock session. **B.** Average normalized firing rate of classified shock-excited $Vglut2^{vBNST \rightarrow VTA}$ neurons is significantly altered compared to classified no-effect neurons during and after the foot-shock session ($F_{99,2900} = 3.13$, $P < 0.0001$, $n = 34$ units, $n = 7$ mice). Inset, percentages of classified neurons. **C.** Colour-coded normalized firing rates for all identified $Vgat^{vBNST \rightarrow VTA}$ neurons in response to the first foot-shock session. **D.** Average normalized firing rate of classified shock-inhibited $Vgat^{vBNST \rightarrow VTA}$ neurons is significantly altered compared to classified no-effect neurons during and after the foot-shock session ($F_{99,2600} = 2.66$, $P < 0.0001$, $n = 33$ units, $n = 5$ mice). **E.** Colour-coded normalized firing rates of identified $Vglut2^{vBNST \rightarrow VTA}$ neurons in response to cue re-exposure. **F.** Average normalized firing rate of classified cue-excited $Vglut2^{vBNST \rightarrow VTA}$ neurons is significantly altered compared to classified no-effect neurons during and after cue re-exposure ($F_{99,3100} = 5.135$, $P < 0.0001$, $n = 37$ units, $n = 4$ mice). **G.** Colour-coded normalized firing rates of $Vgat^{vBNST \rightarrow VTA}$ neurons in response to cue re-exposure. **H.** Average normalized firing rate of classified cue-inhibited $Vgat^{vBNST \rightarrow VTA}$ neurons is significantly altered compared to classified no-effect neurons during and after cue re-exposure ($F_{99,4,900} = 8.285$, $P < 0.0001$, $n = 56$ units, $n = 4$ mice).

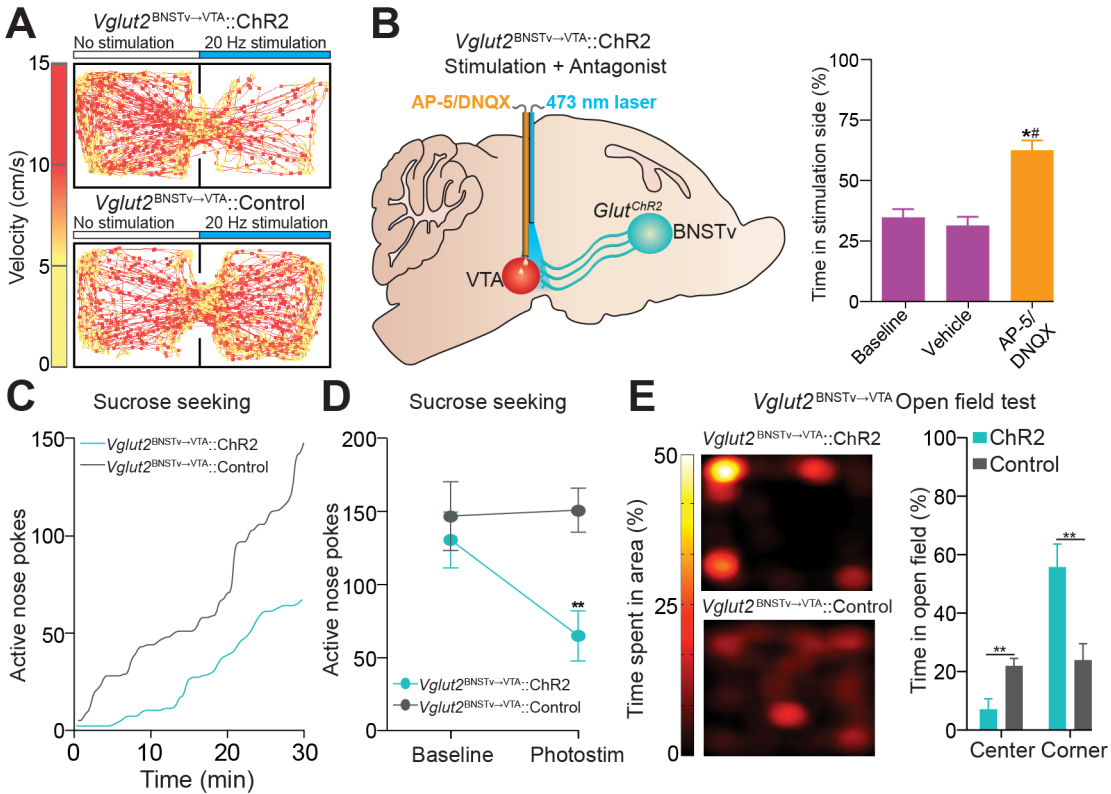


Figure 2.8: Photostimulation of the $Vglut2^{vBNST \rightarrow VTA}$ pathway promotes aversion and anxiety. **A.** Representative RTTPP tracks from $Vglut2^{vBNST \rightarrow VTA}::ChR2$ (top) and control (bottom) mice. **B.** Intra-VTA infusions of a glutamate antagonist cocktail (D(-)-2-amino-5-phosphonovaleric acid (AP5) plus DNQX), followed by $Vglut2^{vBNST \rightarrow VTA}::ChR2$ stimulation during blocked aversion in the RTTPP test ($F_{3,15} = 12.811$, $P < 0.001$, $n = 6$ mice). **C.** Example cumulative records of active nose pokes made by representative $Vglut2^{vBNST \rightarrow VTA}::ChR2$ and $Vglut2^{vBNST \rightarrow VTA}::Control$ mice to obtain a sucrose reward during constant 20 Hz photostimulation. **D.** $Vglut2^{vBNST \rightarrow VTA}::ChR2$ mice made significantly fewer nose pokes for a sucrose reward during constant 20 Hz photostimulation when compared to $Vglut2^{vBNST \rightarrow VTA}::Control$ mice ($F_{1,12} = 13.09$, $P = 0.008$; $n = 7$ mice per group). **E.** Representative heat maps displaying average time spent in an open field for 10 min after stimulation from $Vglut2^{vBNST \rightarrow VTA}::ChR2$ (top) and $Vglut2^{vBNST \rightarrow VTA}::control$ (bottom) mice. $Vglut2^{vBNST \rightarrow VTA}::ChR2$ mice spent significantly

more time in the corners ($P = 0.008$) and less time in the centre ($P = 0.007$) of an open field immediately after constant 20-Hz stimulation than *Vglut2*^{vBNST→VTA}::control mice (n = 6 mice per group). Data are mean \pm s.e.m. * $P < 0.05$; ** $P < 0.01$. Dagger symbol denotes significance compared to all manipulations.

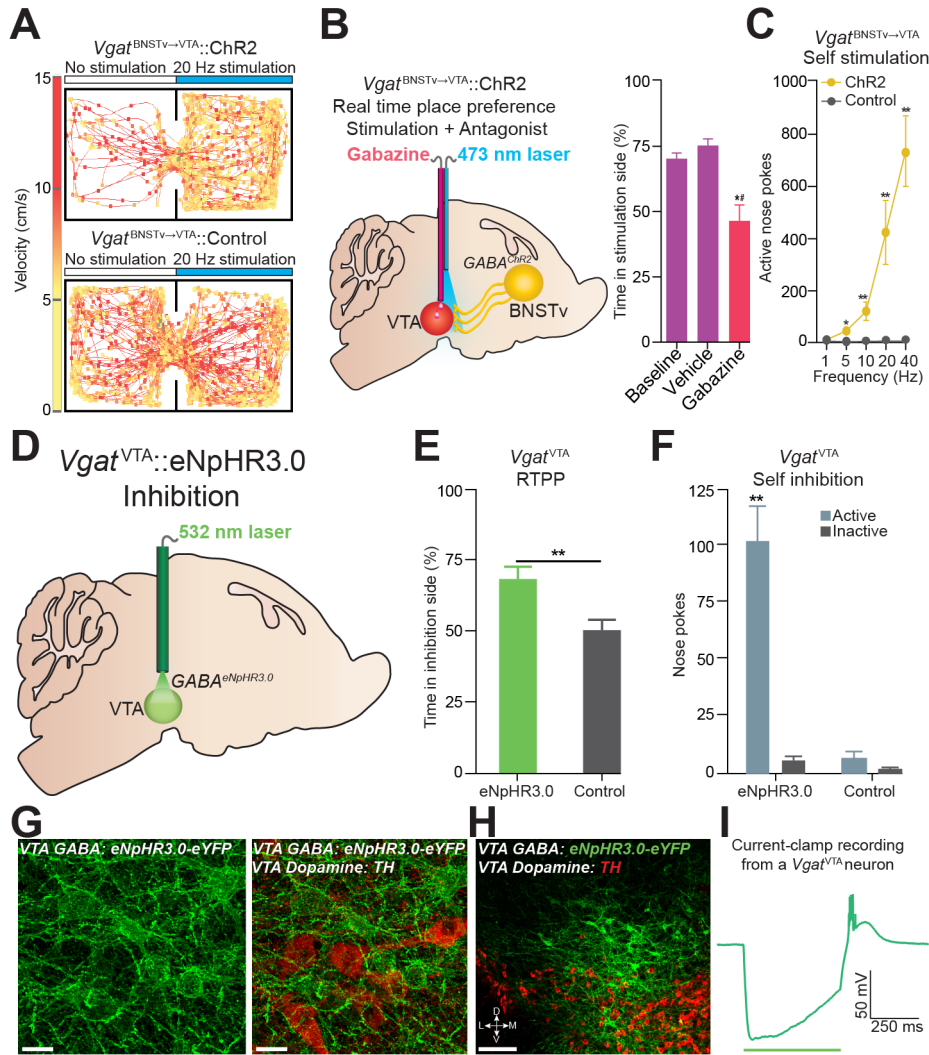


Figure 2.9: Photostimulation of the $Vgat^{vBNST \rightarrow VTA}$ pathway and inhibition of $Vgat^{VTA}$ neurons produces reward-related behaviours. **A.** Representative RTTP tracks from $Vgat^{vBNST \rightarrow VTA}::ChR2$ (top) and control (bottom) mice. **B.** Intra-VTA infusions of the GABA_A antagonist gabazine followed by $Vgat^{vBNST \rightarrow VTA}::ChR2$ stimulation abolished place preference ($F_{3,15} = 13.718$, $P < 0.001$, $n = 6$ mice). **C.** $Vgat^{vBNST \rightarrow VTA}::ChR2$ mice made significantly more nose pokes to obtain photostimulation than controls ($F_{4,36} = 12.42$, $P < 0.001$, $n = 5 - 7$ mice per group). **D.** Schematic detailing $Vgat^{VTA}::eNpHR3.0$ inhibition during behavioural experiments. **E.** $Vgat^{VTA}::eNpHR3.0$ mice spent significantly more time in the inhibition-paired side than

controls ($P = 0.01$, $n = 6$ mice per group). **F.** $Vgat^{VTA}::eNpHR3.0$ mice made significantly more nose pokes to obtain photoinhibition than controls ($P < 0.001$, $n = 5$ mice per group). **G.** 63x confocal image showing expression of eNpHR3.0-eYFP (green) in $Vgat^{VTA}$ neurons (left) and tyrosine hydroxylase (TH) (right). (Scale = 20 μm). **H.** 20x confocal image showing expression of eNpHR3.0-eYFP in $Vgat^{VTA}$ neurons following injection of the viral construct into the VTA, shown in green. VTA dopaminergic neurons, as indicated by TH immunoreactivity, are shown in red (D, dorsal; V, ventral; L, lateral; M, medial; Scale bar = 200 μm). **I.** Example whole-cell current clamp recording showing robust membrane hyperpolarization after a 500 ms green light pulse (532 nm) in a VTA neuron expressing eNpHR3.0-eYFP. Average hyperpolarization of membrane = -52.95 ± 11.95 mV in $n = 4$ neurons.

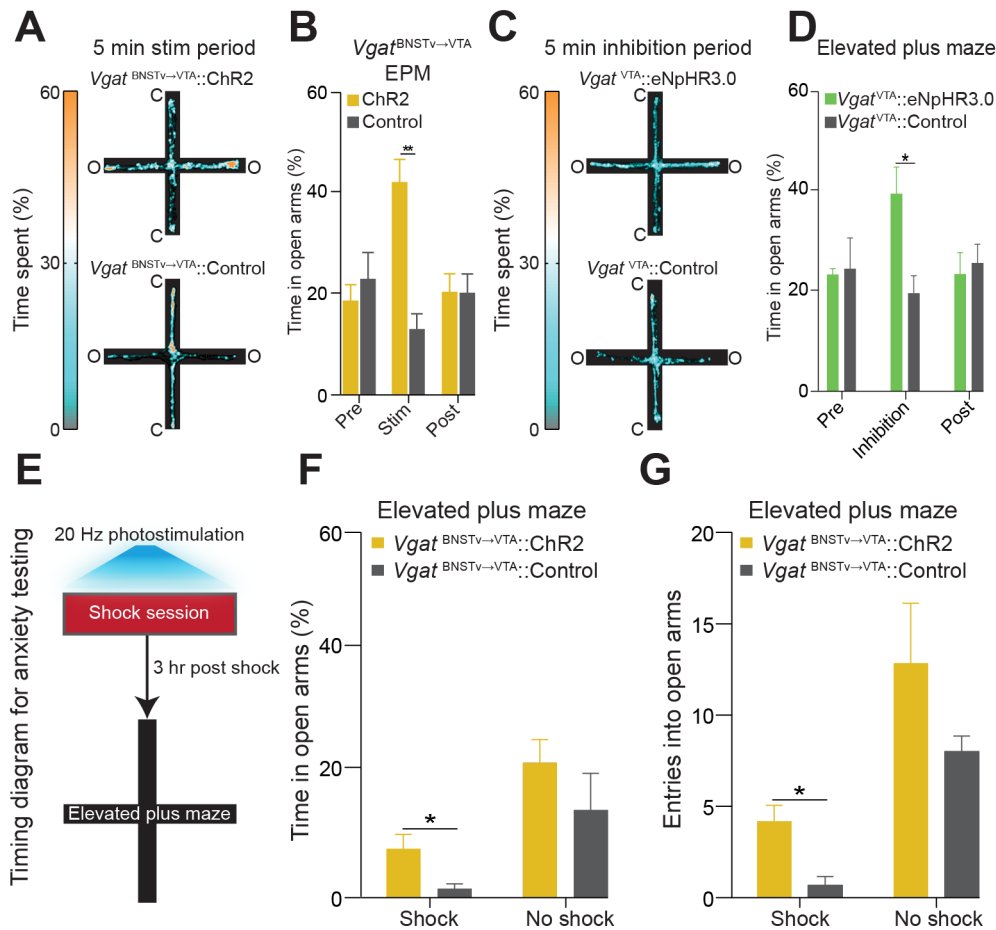


Figure 2.10: Photostimulation of the $Vgat^{vBNST \rightarrow VTA}$ pathway and inhibition of $Vgat^{VTA}$ neurons attenuates anxiety. **A.** Representative heat maps displaying average time spent in the elevated plus maze during the 5 min photostimulation epoch from $Vgat^{vBNST \rightarrow VTA}::ChR2$ (top) and $Vgat^{vBNST \rightarrow VTA}::Control$ (bottom) mice (O, open arm; C, closed arm). **B.** $Vgat^{vBNST \rightarrow VTA}::ChR2$ mice spent significantly more time in the EPM open arms than controls during the 5-min photostimulation epoch ($F_{2,24} = 14.648$, $P < 0.001$, $n = 7$ mice per group). **C.** Representative heat maps displaying average time spent in the elevated plus maze during the 5 min photoinhibition epoch from $Vgat^{VTA}::eNpHR3.0$ (top) and $Vgat^{VTA}::Control$ (bottom) mice. **D.** $Vgat^{VTA}::eNpHR3.0$ mice spent significantly more time in the open arms compared to $Vgat^{VTA}::Control$ mice ($n = 5$ mice per group) during the 5 min photoinhibition epoch ($F_{2,16} = 10.519$, $P < 0.01$). **E.** Schematic of shock-induced anxiety paradigm. **F-G.** 3 hr after shock exposure,

Vgat^{vBNST→VTA}::ChR2 mice spent significantly more time in the open arms (**F**; $F_{1,20} = 12.822$, $P = 0.002$, $P = 0.03$) and made significantly more open-arm entries (**G**; $F_{1,20} = 20.3771$, $P < 0.001$, $P = 0.008$) compared to *Vgat*^{vBNST→VTA}::Control mice (n = 6 - 7 per group). All values are \pm s.e.m. * $P < 0.05$.

CHAPTER 3: THE INHIBITORY CIRCUIT ARCHITECTURE OF THE LATERAL HYPOTHALAMUS ORCHESTRATES FEEDING³

Introduction

The growing prevalence of overeating disorders is a key contributor to the worldwide obesity epidemic. Dysfunction of particular neural circuits may trigger deviations from adaptive feeding behaviors. The LH is a crucial neural substrate for motivated behavior including feeding, but the precise functional neurocircuitry that controls LH neuronal activity to engage feeding has not been defined. We observed that inhibitory synaptic inputs from the extended amygdala preferentially innervate and suppress the activity of LH glutamatergic neurons to control food intake. These findings help explain how dysregulated activity at a number of unique nodes can result in a cascading failure within a defined brain network to produce maladaptive feeding.

Over half a century ago, experiments in rodents and other species have revealed that gross neuroanatomical manipulations of the LH alter diverse behaviors, including feeding (DELGADO and ANAND, 1953; Hoebel and Teitelbaum, 1962; Wise, 1968). While direct anatomical and neuropharmacological manipulations (Stanley et al., 1993; Turenius et al., 2009) within the LH produce profound alterations in a variety of motivated behaviors, they provide

³This chapter previously appeared as an article published in the journal *Science*. The original citation is as follows: Jennings JH, Rizzi G, Stamatakis AM, Ung RL, Stuber GD. (2013). The inhibitory circuit architecture of the lateral hypothalamus orchestrates feeding. *Science*. 341, 1517-1521. PMID: 24072922.

limited mechanistic insight into the discrete circuit connections within the LH that regulate precise behaviors such as feeding. Given the circuit complexity within the LH (Hahn and Swanson, 2012), we aimed to dissect the neurocircuitry between the LH and a principal afferent from the extended amygdala. The BNST, a neural component of the extended amygdala (de Olmos and Heimer, 1999), is a key integrator of diverse motivational states through its interactions with various synaptic targets, including the ventral tegmental area (VTA) (Jennings et al., 2013) and the LH (Kim et al., 2013). The BNST is comprised primarily of GABAergic cells (Kudo et al., 2012) and consumption of food activates BNST neurons (Ángeles-Castellanos et al., 2007). Therefore, we considered the BNST and its inhibitory projections to the LH as an important candidate for regulating feeding.

Methods

Experimental subjects and stereotactic surgery

All procedures were conducted in accordance with the Guide for the Care and Use of Laboratory Animals, as adopted by the NIH, and with approval of the Institutional Animal Care and Use Committee at UNC. Adult (25-30g) male *Vgat-ires-Cre* and *Vglut2-ires-Cre* (Vong et al., 2011) mice were group housed prior to surgery. All mice were maintained on a reverse 12-hr light cycle (lights off at 07:00) with *ad libitum* access to food and water, unless described below. Mice were anesthetized with a ketamine (150 mg per kg of body weight) and xylazine (50 mg per kg) solution and placed into a stereotactic frame (Kopf Instruments). All viral constructs, except the SADΔG-GFP(EnvA) virus (Viral Vector Core Facility at the Salk Institute for Biological Studies), were packaged and titered by the UNC Vector Core Facility. To photoactivate and photoinhibit *Vgat*^{BNST→LH} projections during *in vivo* behavioral experiments, male *Vgat-ires-Cre* positive and negative littermates were bilaterally microinjected with 0.3 ml of purified and concentrated adeno-associated virus (~10¹² infections units per ml) into the BNST with the following stereotactic coordinates: + 0.14 mm anterior to bregma, +/- 0.9 lateral to

midline, and - 4.8 mm ventral to skull surface. Each BNST microinjection contained an AAV5 viral construct coding Cre-inducible ChR2-eYFP or eArch3.0-eYFP under control of the EF1 α promoter (AAV5-EF1 α -DIO-hChR2(H134R)-eYFP and AAV5-EF1 α -DIO-eArch3.0-eYFP) to transduce BNST-GABAergic neurons (*Vgat*^{BNST-LH::ChR2} and *Vgat*^{BNST-LH::eArch3.0} mice). In the same surgery, bilateral optical fibers were implanted in the LH using the following stereotactic coordinates: - 1.7 mm posterior to bregma, +/- 0.9 mm lateral to midline, and - 4.75 mm ventral to skull surface. To photoactivate *Vgat*^{BNST-VTA} projections during *in vivo* behavioral experiments, male *Vgat-ires-Cre* positive and negative littermates were bilaterally microinjected in the BNST as described above and implanted with optical fibers in the VTA (*Vgat*^{BNST-VTA::ChR2}) using the following stereotactic coordinates: - 3.2 mm posterior to bregma, +/- 0.5 mm lateral to midline, and - 4.69 mm ventral to skull surface. For all slice electrophysiology experiments, male *Vgat-ires-Cre* positive mice were bilaterally microinjected with 0.3 μ l of the Cre-inducible ChR2-eYFP virus into the BNST using the same coordinates as described above. For direct LH soma photostimulation and photoinhibition behavioral experiments, male *Vglut2-ires-Cre* positive and negative littermates were bilaterally microinjected with 0.3 μ l of purified and concentrated adeno-associated virus (~10¹² infections units per ml) into the LH using the following stereotactic coordinates: - 1.7 mm posterior to bregma, +/- 0.9 mm lateral to midline, and - 4.95 mm ventral to skull surface. Each LH microinjection consisted of an AAV5 viral construct coding Cre-inducible ChR2-eYFP or eArch3.0-eYFP under control of the EF1 α promoter to transduce LH-glutamatergic neurons (*Vglut2*^{LH::ChR2} and *Vglut2*^{LH::eArch3.0}). During the same surgery, bilateral optical fibers were implanted in the LH using the following stereotactic coordinates: - 1.7 mm posterior to bregma, +/- 0.9 mm lateral to midline, and - 4.75 mm ventral to skull surface. The time from virus injection to the start of behavioral and slice electrophysiology experiments was approximately 4 to 6 weeks. For monosynaptic tracing of LH neurons, male *Vglut2-ires-Cre* and *Vgat-ires-Cre*

mice were bilaterally microinjected in the LH with 0.3 μ l of a viral cocktail including AAV5 (3×10^{12} particles/ml) encoding TVA-mCherry under control of the EF1 α promoter (AAV5-EF1 α -FLEX-TVA-mCherry) to allow for initial infection of LH starter neurons as well as an AAV8 (2×10^{12} particles/ml) coding for the rabies virus envelope glycoprotein (RG) under control of the CA promoter (AAV8-CA-FLEX-RG) to allow for transsynaptic spread of LH-glutamatergic and -GABAergic neurons, respectively. Two weeks later, the same mice were bilaterally microinjected with 0.5 μ l of the pseudotyped rabies virus, SAD Δ G-GFP(EnvA) (4×10^8 particles/ml) into the same region of the LH. One week later, the same mice were sacrificed and brains were collected for confocal imaging. See (Watabe-Uchida et al., 2012; Wickersham et al., 2007) for additional details on this method. To determine if BNST-GABAergic neurons project to LH-GABAergic neurons, a subset of male *Vgat-ires-Cre* mice ($n = 2$) received the same rabies microinjections in the LH as described above, as well as bilateral BNST microinjections (0.3 μ l) of an AAV5 virus ($\sim 10^{12}$ infections units per ml) coding Cre-inducible mCherry under control of the EF1 α promoter (AAV5-EF1 α -DIO-mCherry) to transduce BNST-GABAergic neurons.

Histology, microscopy, and image analysis

Mice were anesthetized with pentobarbital, and transcardially perfused with phosphate buffered saline (PBS) followed by 4% paraformaldehyde (weight/volume) in PBS for 24 hr and transferred to 30% sucrose in ddH₂O for 48 hr. 40- μ m brain sections were obtained and counterstained with DAPI for Nissl labeling (Vector Laboratories). Z-stack and tiled images of mounted brain sections were captured on a Zeiss LSM 710 confocal microscope using a 10x, 20x, or 63x objective. To determine optical fiber placement, tissue was imaged at 10x and 20x on an upright epi-fluorescent microscope. For quantifying neurons targeted with rabies and quantifying fluorescence intensity in the BNST, 10x confocal images were acquired using

identical pinhole size, gain level, axial section (z) depth, and laser intensity settings for all brain regions. ImageJ software was used to quantify the number of GFP-labeled neurons within the BNST (LH-projecting neurons) and mCherry-expressing neurons in the LH (starter neurons).

Patch-clamp electrophysiology

Mice were deeply anesthetized with pentobarbital and transcardially perfused with ice-cold modified artificial cerebrospinal fluid containing (in mM): 225 sucrose, 119 NaCl, 1.0 NaH₂PO₄, 4.9 MgCl₂, 0.1 CaCl₂, 26.2 NaHCO₃, 1.25 glucose. Brains were then rapidly removed and placed in the perfusion solution at ~ 0°C. Coronal slices containing the LH (200 µm) were cut on a Vibratome. Following slicing, brain slices were placed in a holding chamber containing a bicarbonate-buffered solution saturated with 95% O₂ and 5% CO₂ and containing (in mM): 119 NaCl, 2.5 KCl, 1.0 NaH₂PO₄, 1.3 MgCl₂, 2.5 CaCl₂, 26.2 NaHCO₃, and 11 glucose (at 32-34°C) and allowed to recover for at least 30 min before being placed in a recording chamber and superfused with the bicarbonate-buffered solution. Neurons were visualized using infrared differential interference contrast microscopy and BNST-GABAergic afferents expressing ChR2-eYFP were visualized using fluorescence microscopy. Whole-cell voltage-clamp recordings of LH neurons were made using a microelectrode amplifier. Patch electrodes (2.0 – 3.0 MW) were autoclaved to remove any possible contaminants and then backfilled with a potassium chloride internal solution containing (in mM): 135 KCL, 0.5 EGTA, 10 HEPES, 1.5 MgCl₂ in RNase- and DNase-free water. 2 - 10 ml of RNase inhibitor was added per 1 ml of the internal solution. Access resistance was monitored online with a 5-mV hyperpolarizing step delivered between stimulation sweeps. Cells that showed a > 20% change in the holding current or access resistance were excluded from analysis to avoid possible contamination. All data were filtered at 2 kHz, digitized at 5 – 10 kHz, and collected using pClamp10 software. For paired pulse measurements, membrane potentials were maintained at -70 mV, and blue light pulses (5 ms, 1 - 2 mW, 473 nm) were delivered through a 40x objective

via a LED every 20 s to evoke neuronal firing. Optically evoked inhibitory postsynaptic current (eIPSC) amplitudes were calculated by measuring the peak current from the average response from 4 sweeps. The cytoplasm of the recorded cell was then aspirated by applying negative pressure and the integrity of the seal was monitored during aspiration to prevent extracellular contamination. Cells that showed more than a 100 pA change in holding current were discarded. Immediately following aspiration, the pipette tip was removed from the tissue and broken into an RNase-free PCR tube. ~5 - 10 ml of internal solution containing cytoplasmic material was then injected into the RNase-free PCR tube using positive pressure. Total recording time did not exceed 4 min in order to minimize potential mRNA degradation. The silver wire located inside the recording pipette was wiped thoroughly with alcohol wipes in between each cell recording to minimize cross sample contamination. Furthermore, to control for pipette contamination, after each 5 consecutive recordings, a pipette was lowered into the tissue without aspirating (tissue-stick control) and then processed for qPCR (see below).

Single-cell gene expression profiling

Extracted cell samples were profiled using the Single Cell-to-C_t Kit (Life Technologies). Briefly, cell contents were prepared individually in lysis solution with DNase. The volume of lysis solution and DNase was reduced from the normal protocol to compensate for the added volume of internal solution accompanying each sample. Reverse transcription of RNA to complementary DNA (cDNA) was then performed, followed by a multiplexed preamplification of all target genes using TaqMan Gene Expression Assays. The assays used to detect the 8 target genes in the LH, were the recommended exon-spanning assays for *Slc17ab* (*Vglut2*), *Slc32a1* (*Vgat*), *Pdyn* (Dynorphin), *PMCH* (Melanin-concentrating hormone), *Nts* (Neurotensin), *Hcrt* (Orexin), *TH* (Tyrosine hydroxylase), and *Rn18s* (Control). The house-keeping gene, *Rn18s*, was not preamplified in order to avoid reduced amplification of the other genes in the sample due to its high abundance in all cells. Therefore, its cycle number was adjusted

accordingly during analysis. Next, qPCR was performed to obtain the C_t values of each target gene by using a StepOnePlus qPCR instrument using recommended amplification parameters for TaqMan based probes. Technical replicates from each individual cell was performed as well as those from tissue-stick control on the same 96-well plate. Thus, each 96 well plate contained 5 consecutively recorded cells and their 1 subsequent tissue-stick control sample. Lastly, a tissue punch (calibrator) of the LH (200 μ m thick) was obtained and ran through the same procedure for single-cell gene profiling across the entire LH.

Single-cell gene analysis

Gene expression results obtained from a given recorded neuron were not included for analysis if their qPCR amplification curves were not consistent across technical replicates. In addition, tissue-stick controls did not display any gene expression following qPCR. Gene expression for each sample was normalized to the sample's *Rn18s* expression in order to account for the volume of each collected sample. Fold expression values were calculated as the difference between normalized gene expression of each sample and normalized expression of that gene in the tissue punch calibrator. These fold expression values for each gene were log transformed and analyzed with a non-parametric t test (Mann-Whitney). Neurons were segregated into two groups based on their optically eIPSC amplitudes. Neurons were classified as strongly innervated ($n = 25$ cells) if their eIPSC amplitude was greater than the median split value of -330 pA, while weakly innervated neurons ($n = 23$ cells) ranged from 0 to -330 pA. This categorization allowed us to correlate LH-postsynaptic gene expression patterns with functional connectivity strength within the *Vgat*^{BNST→LH} circuit. However, it is important to consider that some “weakly” innervated neurons might be due to limited ChR2 expression in BNST neurons that innervate them.

In vivo anesthetized electrophysiology

Vgat^{BNST→LH::eArch3.0} and *Vglut2*^{LH::eArch3.0} mice were anesthetized with choral hydrate (4% w/v, 480 mg/kg i.p.) and supplemental doses were administered as needed (4% w/v, 120 mg/kg i.p.). Once anesthetized, mice were placed into a stereotactic frame and body temperature was maintained at ~ 37°C with a homeothermic heating blanket. Tail pinches were performed frequently to monitor the efficacy of the anesthetic and lidocaine (2%) was applied to the incision site. A reference electrode was fixed inside brain tissue, approximately 2 mm from both the BNST and LH. Extracellular neural activity was recorded using glass recording electrodes (5 - 10 MΩ: and filled with 0.5 M NaCl). The recording electrode was lowered into the LH (-1.7 mm posterior to bregma, +/-0.9 mm lateral to midline, and - 4.95 mm ventral to skull surface) by a motorized micromanipulator. Recordings were amplified, bandpass filtered between 300 Hz and 16 kHz and sampled up to 40 kHz. For both terminal and soma inhibition within the LH, an optical fiber coupled to a solid state laser (532 nm) was fed through the side port of the electrode holder to terminate near the tip of the glass recording electrode, which allowed for delivery of ~ 10 mW light pulses into the LH. To inhibit either BNST-GABAergic terminals (*Vgat*^{BNST→LH::eArch3.0}) or glutamatergic cell bodies (*Vglut2*^{LH::eArch3.0}) within the LH, a 5-s light pulse was delivered to the LH every 10 s for 20 trials (each trial having 5-s pre-photoinhibition and 5-s post-photoinhibition periods; Off, On, Off). Recorded neurons were only included for analysis if they responded to the delivery of light. Data acquisition and analysis was performed using pCLAMP software and placements of recording electrode tips within the LH were verified with histological examination of brain tissue following the experiments.

Real-time place preference

Vgat^{BNST→LH::ChR2}, *Vglut2*^{LH::ChR2}, *Vgat*^{BNST→VTA::ChR2}, *Vgat*^{BNST→LH::eArch3.0}, *Vglut2*^{LH::eArch3.0}, and littermate controls were run in the real-time place preference paradigm. For the *Vgat*^{BNST→LH::ChR2} and *Vgat*^{BNST→VTA::ChR2} mice, one chamber was paired with constant

20-Hz photostimulation (10 – 15 mW, 473 nm), while the *Vglut2^{LH}::ChR2* mice received constant 5-Hz photostimulation (10 – 15 mW, 473 nm) in the photostimulation-paired chamber.

Vgat^{BNST→LH}::eArch3.0 and *Vglut2^{LH}::eArch3.0* mice received constant light delivery (10 – 15 mW, 532 nm) when crossing into the photoinhibition-paired side. Percent time spent in the photostimulation- and photoinhibition-paired chambers and velocity was recorded via a CCD camera interfaced with Ethovision software. See (Stamatakis and Stuber, 2012) for additional details on this method.

Photostimulation of *Vgat^{BNST→LH}::ChR2* and *Vgat^{BNST→VTA}::ChR2* mice during feeding behavioral assays

Well-fed *Vgat^{BNST→LH}::ChR2*, *Vgat^{BNST→VTA}::ChR2*, and littermate control mice were placed in a 20" X 10" box with two communicating chambers. On contralateral corners of the box, two 5" side square plastic cups were placed, one of them (food zone) containing standard grain-based chow (20 mg Dustless Precision Pellets) and the other containing no food (non-food zone). Each zone's location was counterbalanced between each animal. The animals were then run through three consecutive paradigms (20 min each): pre-photostimulation, constant 20-Hz photostimulation (10 – 15 mW of 473-nm light delivery via an optical fiber connected to a solid state laser) and post-photostimulation, for a total of 1 hr session. For evoked feeding latency experiments, each *Vgat^{BNST→LH}::ChR2* subject ($n = 9$) received 3 trials of each frequency (5, 10, 20, and 40 Hz) in a counterbalanced fashion with food available in the chamber. The timestamp was marked once the subject picked up the food and displayed chewing behavior. The recording was terminated if the trial exceeded 60 s.

Photoinhibition of *Vgat^{BNST→LH}::eArch3.0* and *Vglut2^{LH}::eArch3.0* mice during feeding behavioral assays

Five to 7 days prior to testing, *Vgat^{BNST→LH}::eArch3.0* and littermate control mice were placed on the food restriction schedule described above. *Vglut2^{LH}::eArch3.0* and littermate

control mice were fed *ad libitum*. Using the same box and cups previously described, mice were run through a 40-min session consisting of 10 min no photoinhibition, 10 min constant photoinhibition (10 – 15 mW of 532-nm light delivery via an optical fiber connected to a solid state laser), 10 min no photoinhibition, and 10 min photoinhibition periods.

Photostimulation of *Vglut2^{LH}::ChR2* and *Vglut2^{LH}::Control* mice during feeding behavioral assays

Vglut2^{LH}::ChR2 and *Vglut2^{LH}::Control* mice were also placed on the same food restriction schedule for 5 - 7 days and were subsequently run through a 40-min session consisting of 10 min no photostimulation, 10 min 5-Hz photostimulation (10 – 15 mW of 473-nm light delivery), 10 min no photostimulation, and 10 min 5-Hz photostimulation periods.

Food preference based on caloric content

Preference for different types of chow was assessed in the same conditions described, placing two different types of chow, one in each plastic cup (counterbalanced between animals). *Vgat^{BNST→LH}::ChR2* and *Vglut2^{LH}::eArch3.0* mice were respectively stimulated (20-Hz 10 – 15 mW 473-nm light delivery) and inhibited (constant inhibition 10 – 15 mW 532-nm light delivery) during a 20-min session following a 10-min habituation period. The standard grain based chow (3.35 kcal/g) was compared to a high-fat chow (5.49 kcal/g), a sugar chow (3.58 kcal/g), and plastic control pellets (equivalent in size and shape) with no caloric value. The plastic control pellets were used to demonstrate that the evoked feeding responses were not due to general gnawing behavior. The preference between the high-fat and sugar chow was also directly assessed in the *Vgat^{BNST→LH}::ChR2* mice. The same food preference paradigms were applied to littermate genotype negative naïve mice to observe their natural preference both in an energy-depleted state and under an *ad libitum* feeding regime. For all feeding paradigms, percent time spent in each designated zone was recorded via a CCD camera interfaced with Ethovision software and the plastic food cups were weighed between each time period for quantifying the

amount consumed. All mice were pre-exposed to each type of chow in their homecage 3 days prior to testing.

Optical self-stimulation of $Vgat^{BNST \rightarrow LH}::ChR2$ projections

$Vgat^{BNST \rightarrow LH}::ChR2$ mice were trained in 30 min daily sessions to nose poke on a fixed ratio (FR-1) schedule for optical self-stimulation of the $Vgat^{BNST \rightarrow LH}::ChR2$ pathway in standard mouse operant chambers. Each active nose poke resulted in a single 3 s 40 Hz optical pulse train. Following 3 days of training, the mice were run on a 60 min daily session consisting of 15 minutes of self-stimulation with each of four different frequencies (5 Hz, 10 Hz, 20 Hz and 40 Hz) on a randomized order, for 6 consecutive days. During the first 2 days of testing mice were free fed standard chow. The next two days, the mice were placed on the same food restriction schedule (2.5 to 3.0 g of standard chow was provided immediately following the cessation of each experiment). For the last two experimental days, the mice were put back on free access to standard chow, but were also given 2 hr access to high-fat food immediately prior to the start of the self-stimulation experiment. All feeding experiments were performed between 12 pm and 2 pm, during the middle of the animals' dark cycle to ensure that food-restricted mice were hungry and that well-fed mice were adequately fed.

Results

$Vgat^{BNST \rightarrow LH}$ circuit activation induces feeding in well-fed mice

We targeted a Cre-inducible viral construct coding for Channelrhodopsin-2 fused to enhanced yellow fluorescent protein (ChR2-eYFP) into the BNST of $Vgat-ires-Cre$ mice and positioned optical fibers above the LH for *in vivo* photostimulation of $Vgat^{BNST \rightarrow LH}$ projection fibers (**Figures 3.1 A-E**). Optogenetic activation of this inhibitory pathway rapidly produced voracious feeding behavior in well-fed mice (**Figures 3.1 F-I**). We explored the motivational valence of this pathway by testing mice in real-time place preference and self-stimulation assays.

$Vgat^{BNST \rightarrow LH}::ChR2$ mice exhibited a significant place preference for a photostimulation-paired chamber (**Figure 3.1 J**) and actively nose poked for photoactivation of the circuit. Food deprivation significantly augmented, while satiety significantly attenuated $Vgat^{BNST \rightarrow LH}::ChR2$ self-stimulation (**Figure 3.1 K**). The evoked feeding response was specific to the $Vgat^{BNST \rightarrow LH}$ pathway. Photoactivation of $Vgat^{BNST \rightarrow VTA}$ projections did not elicit feeding behavior (**Figure 3.2**). Because high-caloric diets can facilitate overeating (Johnson and Kenny, 2010), we determined whether consumption induced by $Vgat^{BNST \rightarrow LH}$ circuit activation was directed towards palatable energy-dense foods. Well-fed $Vgat^{BNST \rightarrow LH}::ChR2$ mice showed a strong preference for high-fat food during photostimulation exposure, suggesting that activation of the $Vgat^{BNST \rightarrow LH}$ circuit is sufficient for eliciting feeding that is preferential for calorie-dense substances even when energy requirements are satisfied.

$Vgat^{BNST \rightarrow LH}$ circuit inhibition diminishes feeding in food-deprived mice and is aversive

To examine whether endogenous activity of the $Vgat^{BNST \rightarrow LH}$ pathway is important for feeding, we transduced BNST-GABAergic neurons (**Figure 3.3 A**) and their axons that innervate the LH (**Figure 3.3 B**) with the inhibitory opsin, archaerhodopsin (eArch3.0-eYFP) (Chow et al., 2010; Mattis et al., 2012). Suppression of presynaptic BNST-GABAergic signaling via eArch3.0 activation resulted in enhanced LH-postsynaptic neuronal activity during anesthetized extracellular recordings (**Figures 3.3 C-E**). Despite the influence of hunger, photoinhibition of the $Vgat^{BNST \rightarrow LH}$ circuit reduced feeding in food-deprived mice (**Figures 3.3 F-J**). Furthermore, photoinhibition of $Vgat^{BNST \rightarrow LH}$ projections led to a significant avoidance of a photoinhibition-paired chamber (**Figure 3.3 K**).

$Vgat^{BNST \rightarrow LH}$ projections preferentially target LH glutamatergic neurons

The hypothalamus contains numerous genetically distinct neuronal populations (Atasoy et al., 2012; Karnani et al., 2013; Knight et al., 2012; Leininger et al., 2011; Sakurai et al., 1998; Sharf et al., 2010; Swanson et al., 2005). We thus characterized the molecular

phenotype of the postsynaptic LH neuronal targets that receive functional $Vgat^{BNST \rightarrow LH}$ innervation. We paired photostimulation of $Vgat^{BNST \rightarrow LH}$ inputs with whole-cell recordings in conjunction with multiplexed gene expression profiling of individual LH neurons in brain slices (**Figure 3.4 A**). We focused on a set of genes known to be heterogeneously expressed in the LH and whose products have been implicated in feeding (Berthoud and Münzberg, 2011). BNST-GABAergic inputs formed strong functional connections with postsynaptic LH neurons that expressed significantly higher levels of $Vglut2$. In contrast, weakly innervated LH neurons displayed significantly lower levels of $Vglut2$ and higher levels of $Vgat$ expression (**Figures 3.4 B and C**).

We confirmed these findings by utilizing modified rabies virus tracing techniques to identify the monosynaptic inputs to glutamatergic and GABAergic neurons in the LH (**Figure 3.4 D**). In $Vglut2-ires-Cre$ and $Vgat-ires-Cre$ mice, we targeted Cre-inducible TVA (AAV5-FLEX-TVA-mCherry) and RG (AAV8-FLEX-RG) proteins that allow for rabies virus infection and subsequent transsynaptic viral propagation, respectively (Watabe-Uchida et al., 2012; Wickersham et al., 2007), to LH-glutamatergic or -GABAergic neurons. Two weeks after AAV transduction, the modified rabies virus, SADΔG-GFP(EnvA), was injected into the LH, and BNST-containing slices were obtained 7 days later for confocal imaging. $Vglut2^{LH}::$ Rabies tracing revealed dense populations of transsynaptically labeled BNST neurons (**Figures 3.4 E and F**), while $Vgat^{LH}::$ Rabies tracing resulted in minimal BNST labeling (**Figures 3.4 G-I**).

Photoactivation of $Vglut2^{LH}$ neurons suppresses feeding in food-deprived mice and is aversive

Because BNST-GABAergic projection neurons promote feeding and selectively target LH glutamatergic neurons, we considered $Vglut2^{LH}$ neurons as a critical downstream circuit node for regulating food intake. Photoactivation of $Vglut2^{LH}$ neurons (**Figure 3.5 A**) suppressed

feeding in food-deprived mice (**Figures 3.5 B-F**) and produced aversion (**Figure 3.5 G**). In contrast, photoinhibition of *Vglut2*^{LH} neurons induced feeding and aversion in well-fed mice (**Figure 3.6**).

Discussion

Until now, the precise neurocircuit elements responsible for the feeding and reinforcement phenomena observed five decades ago by electrical stimulation of the LH (DELGADO and ANAND, 1953; Hoebel and Teitelbaum, 1962; OLDS and MILNER, 1954) have remained a mystery. Inhibitory inputs from the BNST specifically innervate and suppress LH glutamatergic neurons to promote feeding. Further unraveling of the specific patterns of gene expression and projection targets of LH glutamatergic neurons could identify novel points for therapeutic intervention within these circuits for the treatment of eating disorders and obesity.

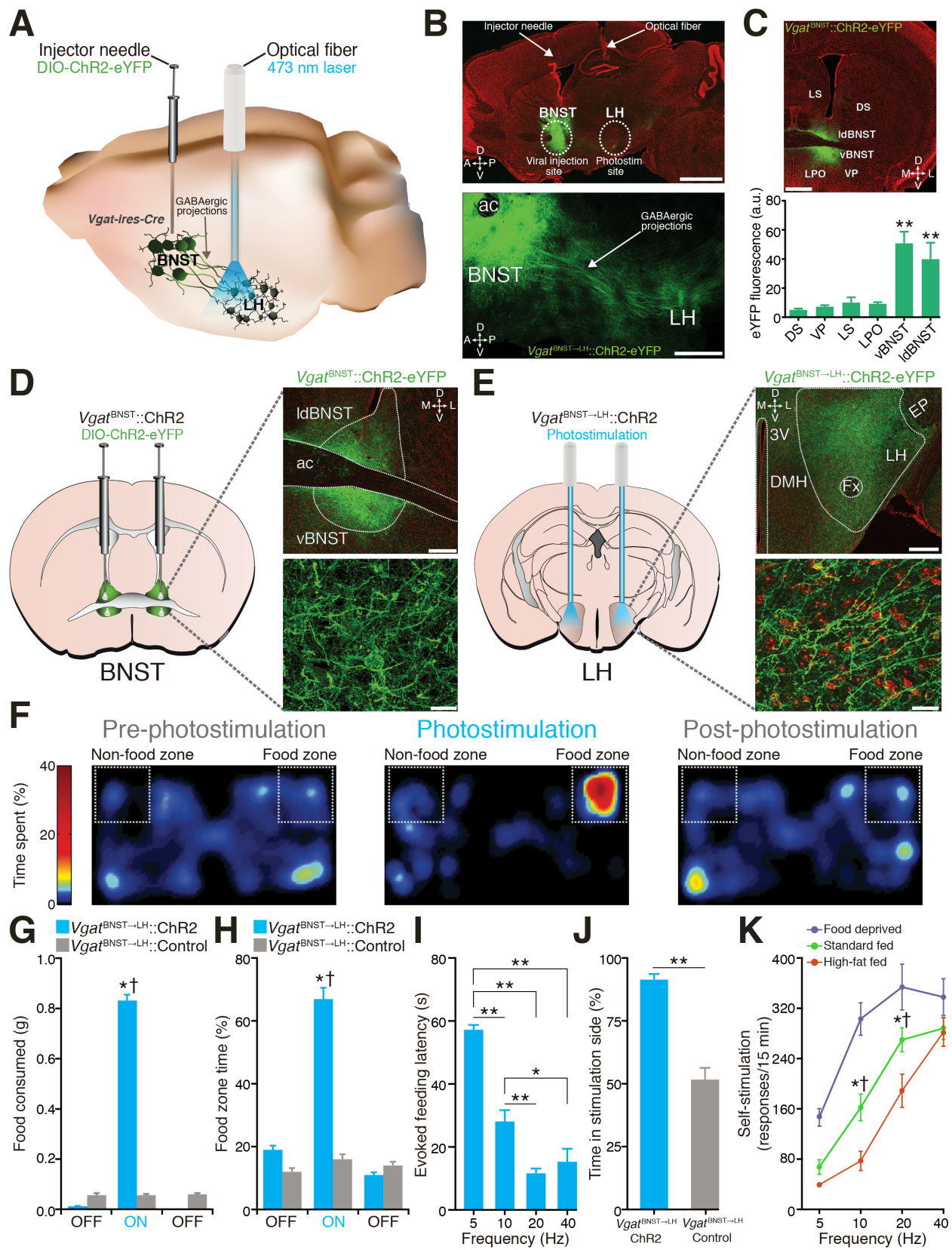


Figure 3.1: *Vgat*^{BNST→LH} circuit activation induces feeding in well-fed mice. (A) *Vgat*^{BNST→LH} circuit targeting. (B) 10x (top) and 20x (bottom) images of the *Vgat*^{BNST→LH}::ChR2-eYFP circuit (scale bars = 1 mm (top), 500 μm (bottom)). (C) Localized ChR2-eYFP expression in the BNST (top) and quantified eYFP fluorescence intensity (bottom) is significantly greater in the BNST compared to surrounding regions ($F_{5,29} = 11.22$, $P < 0.001$, $n = 5$ sections from $n = 5$ mice; ac, anterior commissure; lDBNST, lateral-dorsal BNST; vBNST, ventral BNST; LS, lateral septum; LPO, lateral preoptic area; VP, ventral pallidum; DS, dorsal striatum; scale bar = 200 μm). (D and E) ChR2-eYFP expression in the BNST (D) and axonal projections in the LH (E) in *Vgat-ires-Cre* mice (LH, lateral hypothalamus; Fx, fornix; EP, entopeduncular nucleus; DMH, dorsomedial hypothalamus; 3V, third ventricle; D, dorsal; V, ventral; L, lateral; M, medial; green = ChR2-eYFP; red = Nissl stain; scale bars = 200 μm (top), 20 μm (bottom)). (F) Spatial location heat maps in 20 min epochs before, during, and after 20-Hz photostimulation-induced feeding. (G and H) Photostimulation of *Vgat*^{BNST→LH} projections significantly increased grain-based (standard) food intake ($F_{2,24} = 201.6$, $P < 0.001$) (G) and food zone time ($F_{2,24} = 18.61$, $P < 0.001$, $n = 5$ mice per group) (H). (I) Higher photostimulation frequencies significantly decreased evoked feeding latencies ($F_{3,56} = 48.89$, $P < 0.001$, $n = 9$ mice). (J) *Vgat*^{BNST→LH}::ChR2 mice spent significantly more time in the photostimulation-paired side compared to controls ($P < 0.001$, $n = 5$ mice per group). (K) Food-deprived *Vgat*^{BNST→LH}::ChR2 mice nose poked significantly more for 10- and 20-Hz photostimulation when compared to 2 days of standard fed *ad libitum* and to 2 days of standard fed *ad libitum* supplemented with 2 hr of high-fat food exposure before the self-stimulation session ($F_{2,204} = 40.87$, $P < 0.001$, $n = 9$ mice). All values for all figures represent mean ± s.e.m. * $P < 0.05$, ** $P < 0.001$ (Student's t-test or ANOVA followed by Bonferroni post-hoc comparisons, where applicable). Dagger symbol denotes significance compared to all manipulations.

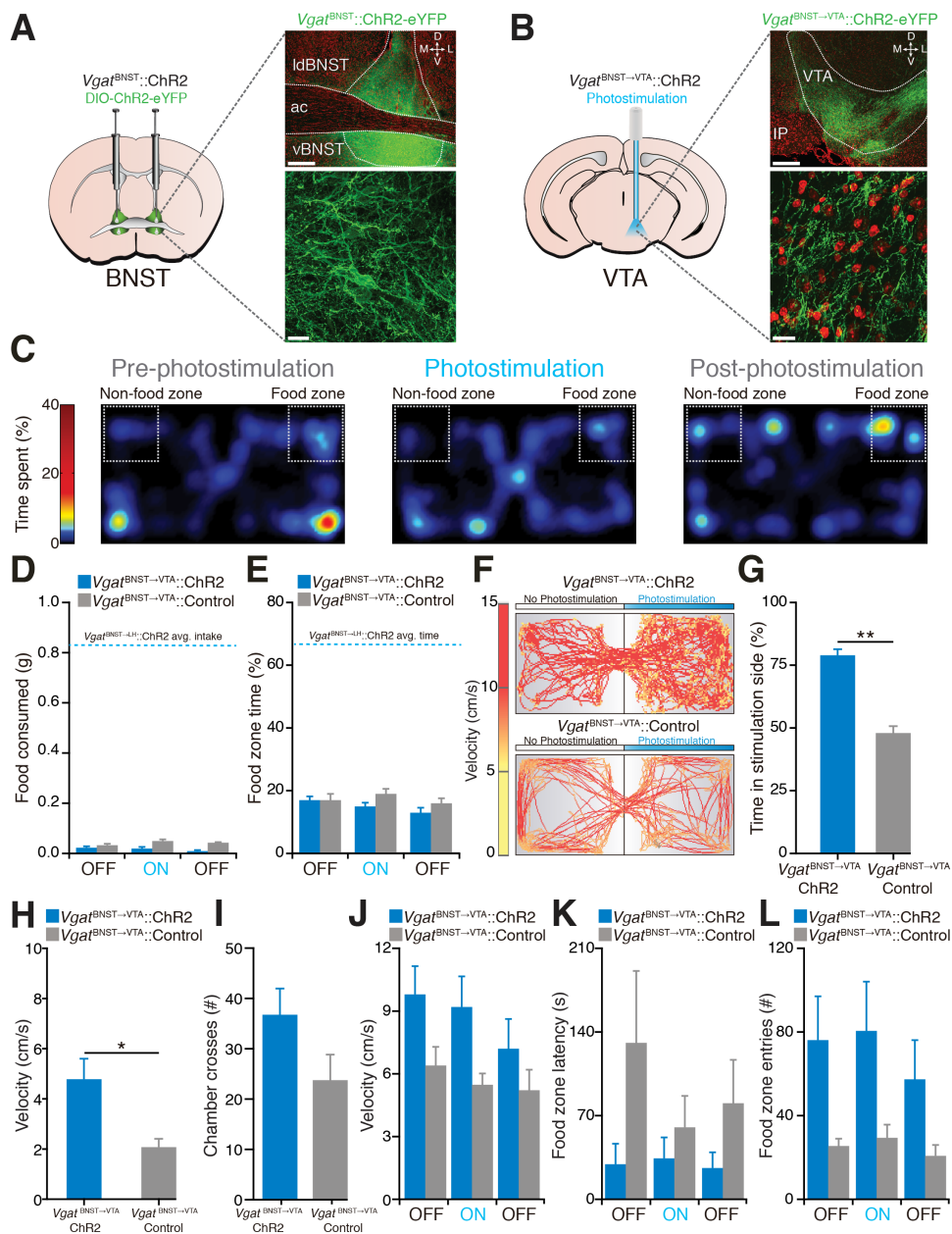


Figure 3.2: Photoactivation of the *Vgat*^{BNST→VTA} pathway is rewarding, but does not produce feeding behavior. (A and B) 10x (top) and 63x (bottom) confocal images depicting ChR2-eYFP expression in the BNST (A) and axonal projections in the VTA (B) of a *Vgat-ires-Cre* mouse (VTA, ventral tegmental area; IP, interpeduncular nucleus; green = ChR2-eYFP; red = Nissl stain; scale bars = 200 μm (top), 20 μm (bottom)). (C) Representative heat maps

displaying average time spent in a chamber containing standard chow before (left), during (middle), and after (right) constant 20-Hz photostimulation from a well-fed $Vgat^{BNST \rightarrow VTA}::ChR2$ mouse. (D and E) Off, On, Off: before, during, after constant 20-Hz photostimulation (20 min each). Photostimulation of $Vgat^{BNST \rightarrow VTA}$ projections does not increase food intake ($F_{2,30} = 0.48$, $P > 0.05$) (D) or food zone time (E) compared to controls and time epochs without photostimulation ($F_{2,30} = 0.18$, $P > 0.05$, $n = 6$ mice per group). (F) Representative real-time place preference tracks from $Vgat^{BNST \rightarrow VTA}::ChR2$ (top) and control (bottom) mice. (G) $Vgat^{BNST \rightarrow VTA}::ChR2$ mice spent significantly more time in the photostimulation-paired side when compared to controls ($P < 0.001$, $n = 6$ mice per group). (H) Average velocity of $Vgat^{BNST \rightarrow VTA}::ChR2$ mice is significantly increased during 20-Hz photostimulation exposure when compared to controls ($P = 0.02$, $n = 6$ mice per group). (I) The number of chamber crosses during real-time place preference testing for $Vgat^{BNST \rightarrow VTA}::ChR2$ and control mice is not significantly different ($P > 0.05$). (J) The velocity during each time epoch of the feeding paradigm was not significantly altered between groups ($F_{2,24} = 0.32$, $P = 0.73$, $n = 6$ mice per group). (K) The latency to enter the food zone was not significantly different between each time epoch ($F_{2,24} = 0.68$, $P = 0.51$, $n = 6$ mice per group). (L) Food zone entries were not significantly different between each time epoch ($F_{2,24} = 0.14$, $P = 0.87$, $n = 6$ mice per group).

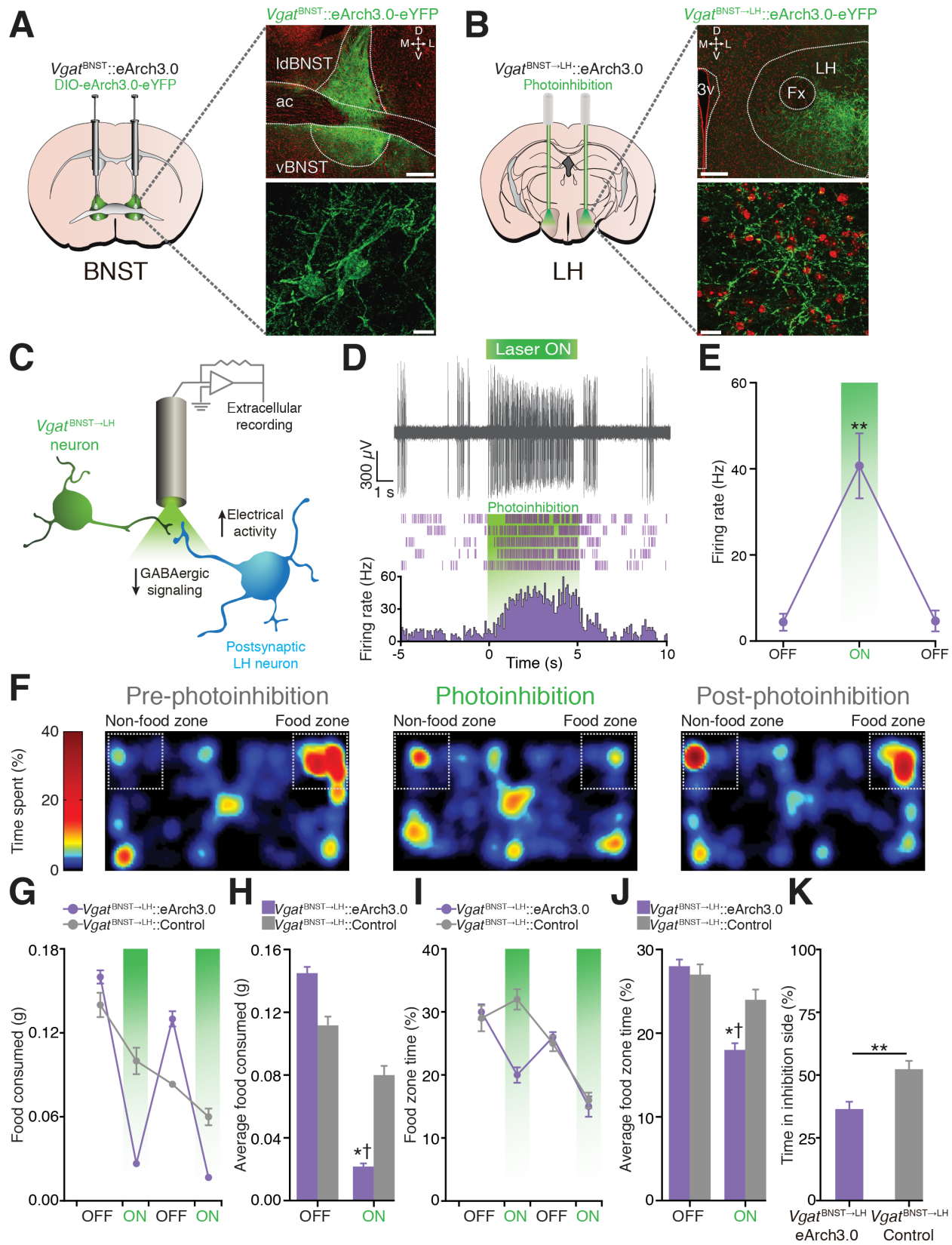


Figure 3.3: $Vgat^{BNST \rightarrow LH}$ circuit inhibition diminishes feeding in food-deprived mice and is aversive. (A and B) eArch3.0-eYFP expression in the BNST (A) and axonal projections in the LH (B) in $Vgat-ires-Cre$ mice (scale bars = 200 μm (top), 20 μm (bottom)). (C) Schematic for anesthetized *in vivo* extracellular recordings in the LH. (D) Example trace from a single LH unit (top) and its representative peri-event histogram and raster (bottom). (E) The average firing rate of light-responsive LH units significantly increased during the 5-s photoinhibition trials ($F_{2,12} = 19.52$, $P < 0.001$, $n = 5$ units from $n = 3$ mice). (F) Spatial location heat maps in 10 min epochs before, during, and after photoinhibition. (G and H) Photoinhibition of $Vgat^{BNST \rightarrow LH}$ projections significantly decreased standard food intake ($F_{1,44} = 16.30$, $P < 0.001$) and time spent in the food zone (I and J) ($F_{1,44} = 2.43$, $P = 0.028$, $n = 6$ mice per group). (K) $Vgat^{BNST \rightarrow LH}::eArch3.0$ mice spent significantly less time in the photoinhibition-paired side when compared to controls ($P = 0.004$, $n = 6$ mice per group).

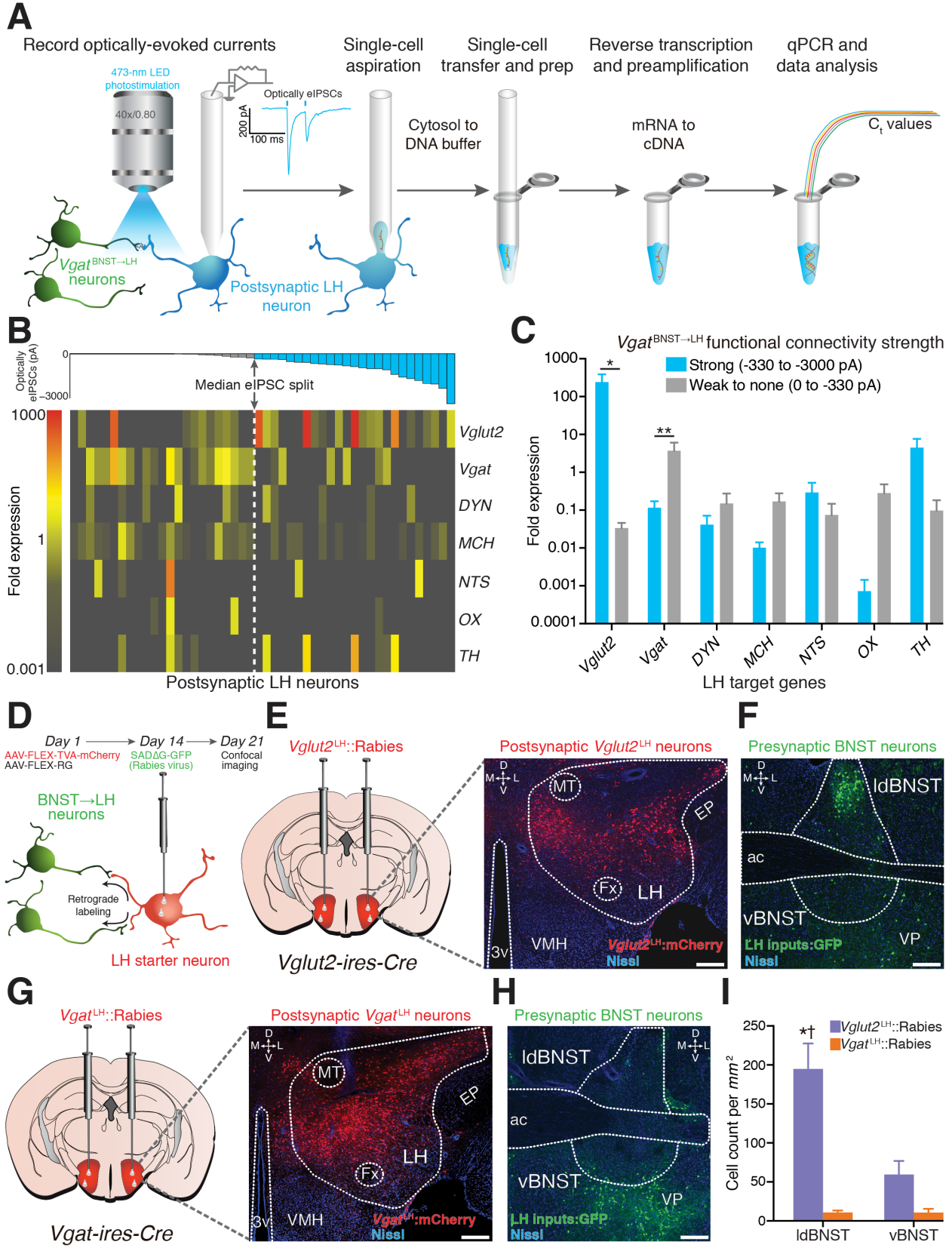


Figure 3.4: *Vgat*^{BNST→LH} projections preferentially target LH glutamatergic neurons. (A) Schematic for ChR2-assisted circuit mapping with single-cell gene expression profiling. (B) Color-coded fold expression of all target genes from all recorded LH neurons (*Vglut2*, vesicular glutamate transporter-2; *Vgat*, vesicular GABA transporter; *DYN*, dynorphin; *MCH*, melanin-concentrating hormone; *NTS*, neurotensin; *OX*, orexin/hypocretin; *TH*, tyrosine hydroxylase). The average fold expression for *Vglut2* was significantly higher in postsynaptic LH neurons that display large optically-evoked inhibitory postsynaptic current amplitudes (strongly innervated) compared to weakly innervated LH neurons ($U = 169.0$, $P = 0.016$, $n = 6$ mice, $n = 48$ cells). (D) Schematic for modified rabies virus tracing. (E and F) Images from a *Vglut2-ires-cre* mouse showing FLEX-TVA-mCherry expression in LH glutamatergic neurons (E) and appreciable SADΔG-GFP labeling of BNST neurons (F). (G and H) FLEX-TVA-mCherry expression in LH GABAergic neurons (G) and minimal SADΔG-GFP labeling of BNST neurons (H) (green = SADΔG-GFP; red = FLEX-TVA-mCherry; blue = Nissl stain; scale bars = 200 μm). (I) Significantly more BNST neurons innervate LH glutamatergic neurons compared to LH GABAergic neurons ($F_{1,20} = 38.50$, $P < 0.001$, $n = 3$ mice per group).

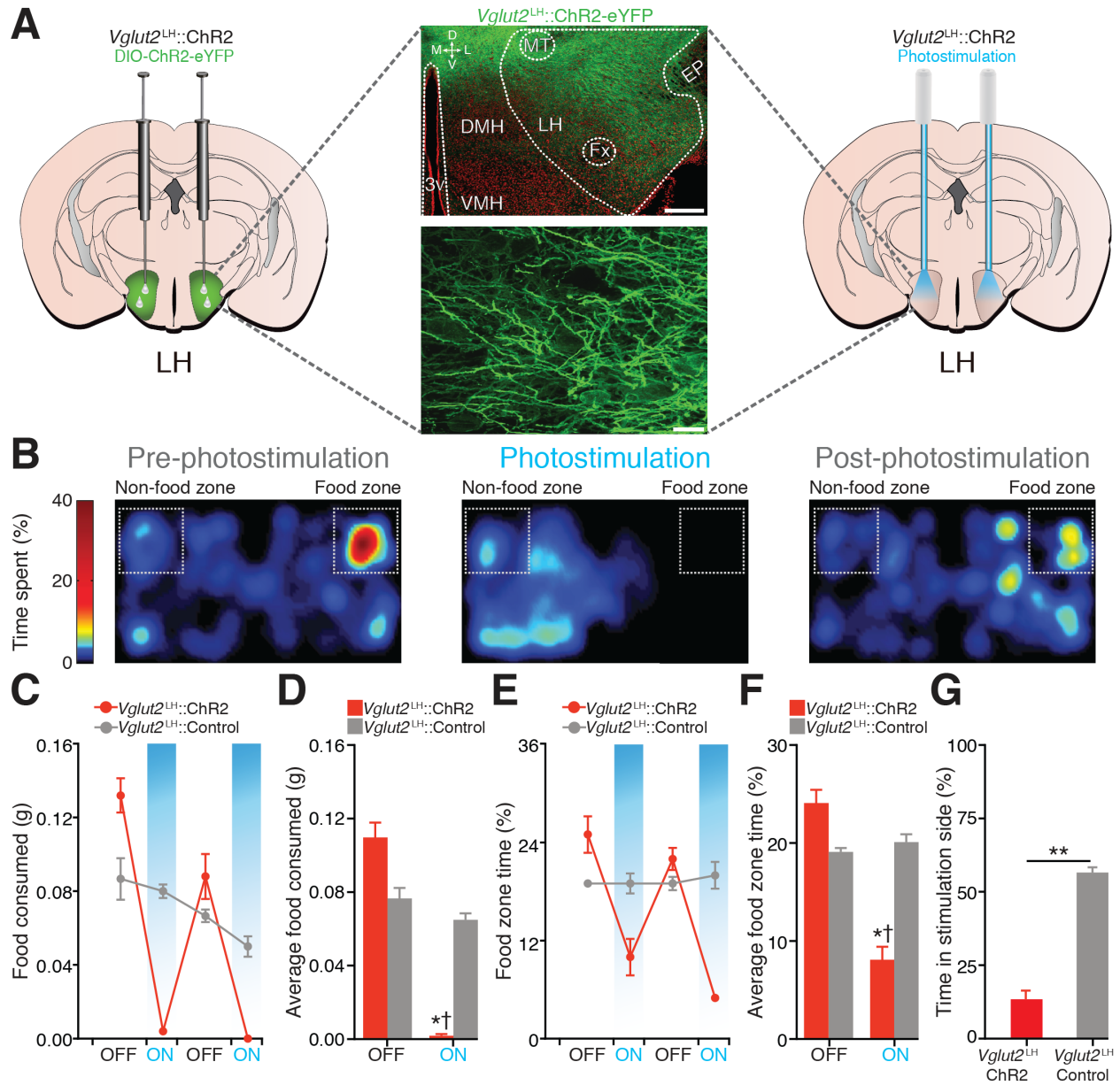


Figure 3.5: Photoactivation of *Vglut2*^{LH} neurons suppresses feeding in food-deprived mice and is aversive. (A) ChR2-eYFP expression in the LH of a *Vglut2-ires-Cre* mouse (scale bars = 200 μm (top), 20 μm (bottom)). (B) Spatial location heat maps in 10 min epochs before, during, and after 5-Hz photostimulation. (C and D) Photostimulation of *Vglut2*^{LH} neurons

significantly decreased food intake ($F_{1,36} = 13.31, P < 0.001$) and food zone time (**E** and **F**) ($F_{1,36} = 13.12, P < 0.001, n = 5$ mice per group). (**G**) *Vglut2*^{LH::}ChR2 mice spent significantly less time in the photostimulation-paired side when compared to controls ($P < 0.001, n = 5$ mice per group).

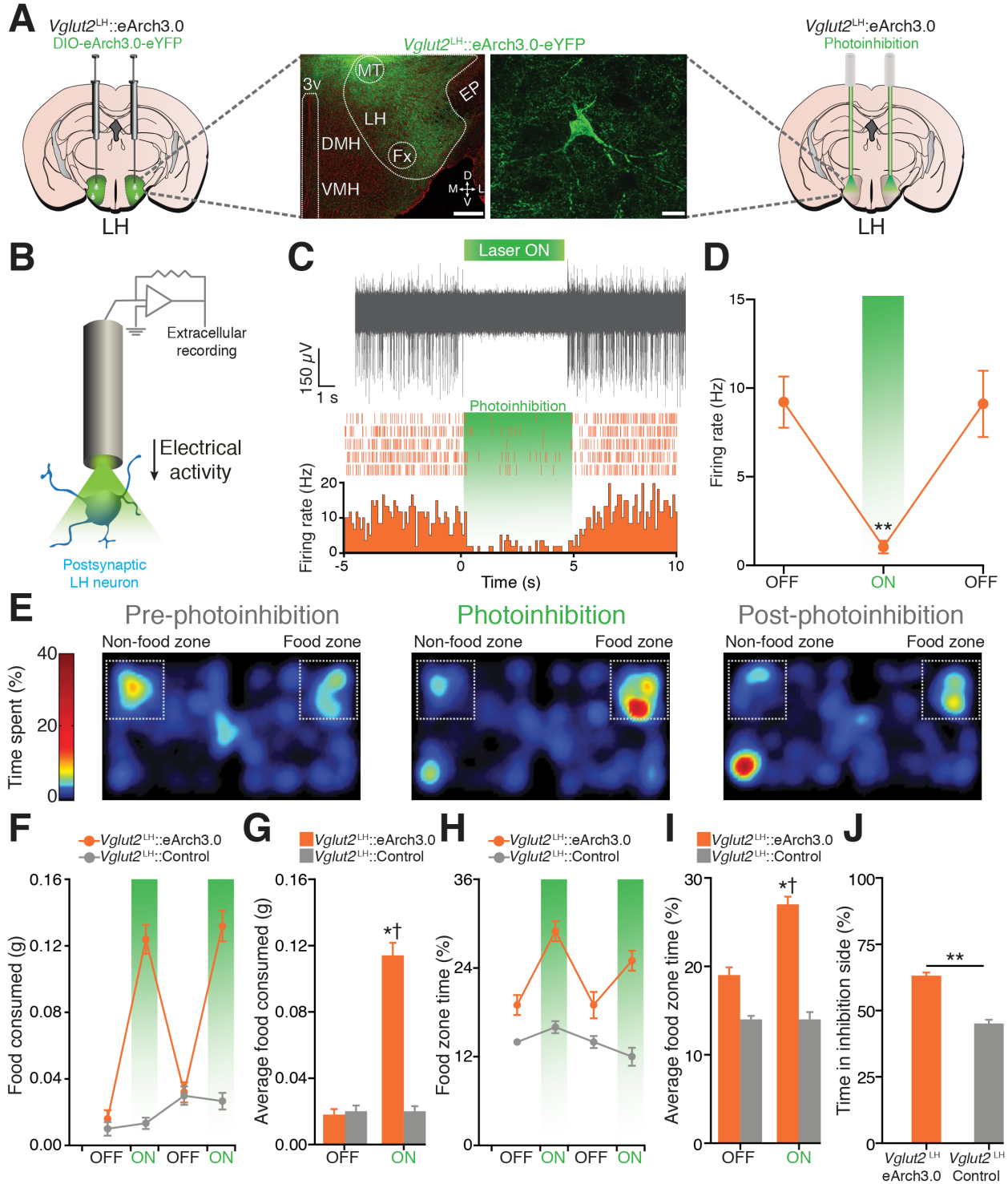


Figure 3.6: Photoinhibition of *Vglut2^{LH}* neurons promotes feeding and is rewarding. (A)

10x (left) and 63x (right) confocal images showing eArch3.0-eYFP expression in the LH of a *Vglut2-ires-Cre* mouse (LH, lateral hypothalamus; Fx, fornix; 3V, third ventricle; DMH,

dorsomedial hypothalamus; VMH, ventromedial hypothalamus; EP, entopeduncular nucleus; MT, medial terminal nucleus of the accessory optic tract; D, dorsal; V, ventral; L, lateral; M, medial; green = eArch3.0-eYFP; red = Nissl stain; scale bars = 200 μm (left), 20 μm (right)). **(B)** Schematic for anesthetized *in vivo* extracellular recordings in the LH. **(C)** An example trace from a single LH unit (top) and its representative peri-event histogram and raster (bottom) demonstrates time-locked inhibition to 5 s photoinhibition. **(D)** Average firing rate of LH units significantly decreased during the 5-s photoinhibition trials ($F_{2,15} = 29.81$, $P < 0.001$, $n = 3$ mice, $n = 6$ units). **(E)** Representative heat maps displaying average time spent in a chamber containing standard chow before (left), during (middle), and after (right) constant 10-min photoinhibition from a *Vglut2^{LH}::eArch3.0* mouse. **(F and G)** Photoinhibition of *Vglut2^{LH}* neurons significantly increased food intake ($F_{1,36} = 35.59$, $P < 0.001$) and time spent in the food zone (**H and I**) compared to controls and time epochs without photoinhibition ($F_{1,36} = 4.17$, $P = 0.04$, $n = 5$ mice per group). Off, On, Off, On: before, during, after constant photoinhibition (10 min each). **(J)** *Vglut2^{LH}::eArch3.0* mice spent significantly more time in the inhibition-paired side compared to controls ($P < 0.01$, $n = 5$ mice per group).

CHAPTER 4: VISUALIZING HYPOTHALAMIC NETWORK DYNAMICS FOR MOTIVATION AND CONSUMPTION⁴

Introduction

The lateral hypothalamus (LH) is a heterogeneous brain area containing numerous genetically distinct cell populations that utilize various signaling modalities (Berthoud and Münzberg, 2011). Gene expression patterns within the LH suggest that individual neurons likely release either inhibitory or excitatory neurotransmitters, γ -aminobutyric acid (GABA) and glutamate (Lein et al., 2007), implying that identifiable subdivisions within the global LH neuronal network can be genetically targeted. Electrical stimulation of the LH, which non-specifically activates many cell types and processes, evokes voracious feeding and reward-related behaviors (Hoebel and Teitelbaum, 1962; Margules and Olds, 1962; Olds and Milner, 1954), signifying that this multifunctional brain region is critical for producing motivated behaviors important for feeding and reinforcement processes. However, given the heterogeneous cellular composition of the LH (Adamantidis and de Lecea, 2009; Karnani et al., 2013; Knight et al., 2012; Leininger et al., 2011), and the fact that multiple fibers of passage traverse this region (Hahn and Swanson, 2012), electrical stimulation or lesion studies cannot determine whether genetically defined cell types, such as LH GABAergic neurons, encode and regulate precise aspects of food-seeking and/or consummatory behaviors.

Neural circuit tracing and manipulation experiments revealed that optogenetic activation of inhibitory synapses within the LH produces feeding and motivated behavioral responding

⁴This chapter is currently in revision in the journal *Cell*: Jennings JH^{*}, Ung RL^{*}, Resendez SL, Stamatakis AM, Taylor JG, Huang J, Veleta K, Kantak P, Aita M, Ramakrishnan C, Deisseroth K, Otte S, and Stuber GD (2014; *In revision*). Visualizing hypothalamic network dynamics for motivation and consumption. *Cell*.

(Jennings et al., 2013a). Specifically, photostimulation of GABAergic inputs to the LH from the bed nucleus of the stria terminalis (BNST) evoked voracious feeding in well-fed mice as well as robust optical self-stimulation behavior, suggesting that inhibitory input to the LH is critical for feeding and positive reinforcement behavior. Moreover, inhibitory inputs from the BNST preferentially target and functionally inhibit postsynaptic glutamatergic neurons in the LH. Consistent with this, direct photoactivation of LH glutamatergic neurons suppressed food intake and produced aversion, while photoinhibition of LH glutamatergic neurons promoted feeding and reward-related phenotypes. These previous findings suggest that distinct circuit elements in the LH may regulate opposing behavioral phenotypes, i.e. reward/aversion and hyper/hypophagia. In the current study, we examined if molecularly defined LH neurons that synthesize and release GABA, function in an opposite fashion to promote feeding and reward-related behaviors. First, we manipulated the activity of LH GABAergic neurons with optogenetic and chemogenetic applications during various feeding-related behaviors to determine whether these neurons play a causal role in regulating motivation and/or consumption. In addition, we employed a cell-type specific ablation strategy to test if the long-term loss of LH GABAergic neurons modulated these behavioral processes. All together, these functional assays demonstrated that activation of LH GABAergic neurons is sufficient to promote feeding *and* reward-seeking behaviors, while LH GABAergic neuronal inactivation or ablation disrupts food-seeking *and* consummatory behaviors. Lastly, we utilized recently developed miniature microscope systems (Ghosh et al., 2011; Ziv et al., 2013) in combination with the genetically encoded calcium (Ca^{2+}) indicator, GCaMP6m (Chen et al., 2013), to image Ca^{2+} activity dynamics from large populations of LH GABAergic neurons in freely moving mice. Using this approach, we optically detected separate neuronal ensembles within the LH GABAergic network that selectively responded to aspects of either motivation or consumption, highlighting the intrinsic computational diversity with the larger LH GABAergic neuronal population. Therefore, individual subsets of LH GABAergic neurons possess a unique signature, which reaffirms the

observation that this neuronal network, as a conglomerate, serves a dual role in controlling food-motivated behaviors. Collectively, these data begin to provide a framework for understanding how a single neuronal population within one brain area can orchestrate distinct aspects of behavior. Furthermore, these experiments outline a viable approach for visualizing the natural activity dynamics and spatial topography of a defined cell population, located deep within the brain, during complex behaviors.

Methods

Animal Subjects

All procedures were conducted in accordance with the Guide for the Care and Use of Laboratory Animals, as adopted by the NIH, and with approval of the Institutional Animal Care and Use Committee at the University of North Carolina at Chapel Hill (UNC). Adult (25 – 30 g) male *Vgat-IRES-Cre* (Vong et al., 2011) mice were used to target LH GABAergic neurons. Mice were maintained on a reverse 12-hr light cycle (lights off at 07:00) with *ad libitum* access to food and water unless placed on a food restriction schedule for certain feeding experiments. All food-deprived mice were restricted to 85 to 90% of their initial body weight by administering one daily feeding of ~ 2.5 to 3.0 g of standard grain-based chow (immediately following behavioral experiment, if performed). All feeding-related behavioral experiments were conducted the same time in the middle of the animals' dark cycle (at approximately 14:00).

Viral Constructs

Purified and concentrated adeno-associated viruses coding for Cre-inducible ChR2-eYFP (AAV5-EF1 α -DIO-hChR2(H134R)-eYFP), eArch3.0-eYFP (AAV5-EF1 α -DIO-eArch3.0-eYFP), hM3Dq-mCherry (AAV8-hSyn-DIO-hM3D(Gq)-mCherry), and taCasp3 (AAV2-FLEX-taCasp3-TEVp) were all packaged by the UNC Vector Core Facility at titers of ~ 2 x 10¹² cfu per ml. The Cre-dependent GCaMP6m viral construct (AAVDJ-EF1 α -DIO-GCaMP6m) was

packaged in the laboratory of Dr. Karl Deisseroth (Stanford University, CA) at a titer of 9.7×10^{12} cfu per ml. To avoid overexpression and cell death via excessive Ca^{2+} buffering, the viral aliquots were diluted with sterile saline to a final titer of $\sim 2 \times 10^{12}$ cfu per ml.

Stereotactic Surgeries

All mice used in this study were anesthetized with 1.5 to 2.0% isoflurane (mixed with 1 L per min of oxygen) for surgical procedures and placed into a stereotactic frame (David Kopf Instruments, Tujunga, CA). Body temperature was maintained at 37 °C with a homoeothermic heating blanket (Harvard Apparatus, Holliston, MA), and ophthalmic ointment (Akorn, Lake Forest, IL) was used periodically to maintain eye lubrication. 2% lidocaine (Akorn, Lake Forest, IL) was applied to the sterilized incision site as an analgesic, while subcutaneous saline injections were administered throughout each surgical procedure to prevent dehydration. In addition, acetaminophen was administered for 2 days post-surgery in the animals' drinking water.

Adult male *Vgat-IRES-Cre* positive and negative littermates (Controls) were bilaterally microinjected with 0.3 μl of virus into the LH using the following stereotactic coordinates: -1.3 mm posterior to bregma, ± 0.9 mm lateral to midline, and -5.3 mm ventral to skull surface. For LH GABAergic somata photostimulation and photoinhibition experiments, mice were bilaterally implanted with optical fibers aimed directly above the LH at -1.3 mm posterior to bregma, ± 0.9 mm lateral to midline, and -4.85 mm ventral to skull surface.

To prepare animals for *in vivo* Ca^{2+} imaging experiments, each subject underwent two separate surgical procedures. First, mice received a unilateral 0.3 μl microinjection of AAVDJ-EF1 α -DIO-GCaMP6m into the LH using the same stereotactic coordinates described above (-1.3 mm posterior to bregma, ± 0.9 mm lateral to midline, and -5.3 mm ventral to skull surface). Two weeks later, the microendoscope (a pair of gradient refractive index lenses fused together with a relay lens) was implanted above the previous injection site. For the procedure, a

craniotomy was performed with a trephine bit (1.8-mm diameter tip; Fine Science Tools, Foster City, CA), and saline was repeatedly applied to the exposed tissue to prevent drying. The dura was then carefully removed with a 30-gauge beveled syringe needle bent at a 90° angle, and portions around the edges of the craniotomy were aspirated (300 to 400 µm of tissue was removed) in a circular motion with a 30-gauge beveled syringe needle attached to a vacuum pump to create a clear entry point. The microendoscope (0.44 pitch, 0.47 NA, 0.5 mm in diameter, and 8.2 mm in length; Inscopix, Palo Alto, CA) was slowly lowered into tissue with a modified mini bulldog serrefine (Fine Science Tools, Foster City, CA) attached to a stereotactic arm. The microendoscope was retracted +500 µm every -1 mm ventral increment to allow penetrated tissue to properly settle around the lens. These steps were repeated until the bottom of the lens was situated approximately 200 to 300 µm directly above the LH (-5.1 mm ventral from the skull surface) as the focal plane is ~ 300 µm below the bottom of the lens (Ziv et al., 2013). Next, the portion of the lens extending ~ 2 to 3 mm above the skull surface was fixed with dental cement (Lang Dental Manufacturing Co., Inc., Wheeling, IL) and anchored by 3 skull screws (Fine Science Tools, Foster City, CA) evenly spaced around the lens. A silicone elastomer (Kwik-Cast; World Precision Instruments, Sarasota, FL) was applied to the top of the lens to protect the imaging surface from external damage.

To support the miniaturized microscope on animals' head, a baseplate (Inscopix, Palo Alto, CA) was adjoined to the dental cement previously formed. For the procedure, two weeks after lens implantation, mice were anesthetized with isoflurane, and the silicone mold around the lens was carefully detached with forceps (Fine Science Tools, Foster City, CA). Debris was removed from the exposed lens with compressed air canisters (Staples Inc., Framingham, MA), and lens paper (Thorlabs Inc., Newton, New Jersey) with ddH₂O was used to clean the top of the lens. Next, the miniature microscope (2 g, 900 x 650 µm max field of view, single-channel epifluorescence: 475-nm blue LED; Inscopix, Palo Alto, CA) with the baseplate attached was

positioned above the implanted lens with an adjustable gripper (Inscopix, Palo Alto, CA). The microscope was lowered towards the top of the lens by a motorized micromanipulator (Scientifica, Uckfield, East Sussex) until the field of view was in focus, i.e., when tissue landmarks such as blood vessels or cells appeared sharp and in focus. To ensure that the objective lens was completely parallel and aligned with the microendoscope, the angle of the microscope's position was slightly adjusted within the gripper by manually tilting the scope about x,y axes. Once the field of view was in focus and the scope was parallel with the lens, the magnetic baseplate was cemented around the microendoscope. Finally, a cover implant (Inscopix, Palo Alto, CA) was secured into the baseplate with a set screw to protect the lens until imaging.

Histology and Confocal Microscopy

For immunohistochemical detection of Fos, LH^{GABA::hM3Dq} and LH^{GABA::Control} mice received an intraperitoneal (i.p.) injection of CNO (1 mg/kg) and placed back in their home cage for 2 hr prior to sacrifice. All mice were deeply anesthetized with Euthasol (100 mg/kg), and transcardially perfused with phosphate-buffered saline (PBS) and 4% paraformaldehyde (weight/volume) in PBS (PFA). Brains were incubated in PFA at 4 °C for 24 hr then transferred to 30% sucrose in ddH₂O for 48 hr at 4 °C. 40- μ m brain sections were obtained with a cryostat (CM3050; Leica Biosystems, Richmond, VA) and blocked in 3% normal donkey serum for 1 hr. Sections were then incubated in primary antibody (rabbit anti-cFos 1:6,000, Calbiochem, La Jolla, CA) for 48 hr at 4 °C. Following 4 x 10 min washes, the sections were incubated in secondary (Alexa Fluor donkey anti-rabbit 488, 1:500, Jackson Laboratories, West Grove, PA) for 2 hr at 21 °C.

For MCH and ORX immunostaining, 40- μ m LH sections (n = 3 brain slices per subject) from LH^{GABA::hM3Dq}, LH^{GABA::GCaMP6m}, LH^{GABA::taCasp3}, LH^{GABA::ChR2}, and *Vgat-IRE5-Cre*; Ai3 (eYFP) mice (n = 3 mice per group) were incubated in either goat anti-proMCH (sc-14509;

1:1,000; Santa Cruz Biotechnology, Dallas, Texas) or goat anti-orexin-A (sc-8070; 1:1,000; Santa Cruz Biotechnology) for 48 hr at 4 °C. Following four 10-min PBS washes, sections were then incubated in Alexa 647-conjugated donkey anti-goat (1:800; Jackson Laboratories) or in Alexa 488-conjugated donkey anti-goat (1:800; Jackson Laboratories) for LH^{GABA::hM3Dq} sections containing mCherry for 2 hr at 21 °C. Lastly, all sections underwent four consecutive PBS washes and then coverslipped with ProLong Diamond Antifade Mountant with DAPI (Molecular Probes; Life Technologies, Grand Island, NY).

Z-stacks and tiled images of mounted brain sections were captured on a confocal microscope (Zeiss LSM 710) using a 10x, 20x, or 63x objective. For quantifying Fos-positive neurons in LH^{GABA::hM3Dq} and LH^{GABA::Control} brain slices, 10x confocal images were acquired using identical pinhole size, gain level, axial (z) depth, and laser intensity settings for all brain regions. ImageJ software (NIH, Bethesda, MD) was used by a blind observer to quantify the number of Fos-positive neurons within the LH. For determining whether *Vgat*-eYFP and virally-transduced *Vgat* neurons colocalize with either MCH or Orx in the LH, 20x confocal images of anterior to posterior LH (-1.1 to -1.6 mm posterior to bregma) were acquired and then quantified for colocalization between each cell type. To identify optical fiber and lens placements, brain sections were imaged at 10x and 20x on an upright epi-fluorescent microscope (Olympus, Center Valley, PA).

Fluorescence In Situ Hybridization

Mice were rapidly decapitated, and brains were snap frozen with dry ice in an embedding mold of O.C.T Compound (Fisher Scientific, Pittsburgh, PA). Fresh, frozen brains were sectioned at 20 µm on a cryostat (CM3050; Leica Biosystems, Richmond, VA) onto charged slides (Leica Biosystems, Richmond, VA). A given set was hybridized to *Gad1* antisense and sense riboprobes. A 950-bp riboprobe complementary to *Gad1*-sense cDNA that was inserted into the pcrII-TOPO vector (Life Technologies, Carlsbad, CA). Plasmid DNA was

cut with either EcoRV or Asp718 in order to create a template for *in vitro* transcription. All probes were created using digoxigenin (DIG)-labeled nucleotides for detection. The EcoRV template was transcribed with Sp6 RNA Polymerase to generate the sense riboprobe, and the Asp718 template was transcribed with T7 RNA polymerase to generate the antisense riboprobe. Fluorescence in situ hybridization (FISH) was performed at room temperature unless otherwise indicated. Tissue was dried at 50 °C, fixed in 4% DEPC-PFA for 15 min, and washed in DEPC-PBS 3 x 5 min. The tissue was then acetylated in 1X triethanolamine-HCl with 0.25% acetic anhydride for 10 min and subsequently washed in DEPC-PBS 3 x 5 min each. Next, the tissue was prehybridized for 3 hr at 65 °C in hybridization buffer containing 5X saline sodium citrate (SSC), 50% formamide, 1-mg/mL yeast tRNA, 0.1-mg/mL heparin, 0.1% tween-20, 0.005-M EDTA (pH 8.0), and 0.1% CHAPS. Following prehybridization, the tissue was hybridized by incubating in hybridization buffer containing a probe for *Gad1* (DIG-labeled). Post-hybridization stringency washes were performed sequentially at 65 °C in pre-warmed buffers: 1 x 15 min in 2X SSC, 3 x 20 min in 0.2X SSC buffer. Following stringency washes, tissue was further washed at room temperature 2 x 10 min in TS7.5 (0.1-M TRIS-HCl, pH 7.5, 0.15-M NaCl). Tissue was then incubated in 3% H₂O₂ in methanol and washed 3 x 5 min in TS7.5 to eliminate endogenous hydrogen peroxidase activity. Sections were then incubated for 1 hr in 1% blocking buffer (Perkin Elmer, Waltham, MA), followed by incubation for 24 hr at 4 °C in anti-DIG-POD (1:100 dilution in 1% blocking buffer). The following day, after washing 3 x 10 min in TNT wash buffer (0.1-M TRIS-HCl, pH 7.5, 0.15-M NaCl, 0.05% Tween-20), sections underwent a tyramide signal amplification with TSA plus DNP 1:50 in amplification diluent. Following a 4-min incubation, sections were vigorously washed with TNT wash buffer 4 x 10 min and incubated in a DNP primary antibody conjugated with Alexa Fluor 488 (1:500 dilution in TNT; Molecular Probes, Eugene, Oregon) at 4 °C overnight. Sections were then washed 3 x 10 min with TNT wash buffer and coverslipped with a mounting media containing DAPI as a counterstain (Life Technologies, Carlsbad, CA)

Patch-clamp Electrophysiology

LH^{GABA}::hM3Dq mice were anesthetized with Euthazol (100 mg/kg) and perfused transcardially with modified artificial cerebrospinal fluid (aCSF) containing (in mM): 225 sucrose, 119 NaCl, 1.0 NaH₂PO₄, 4.9 MgCl₂, 0.1 CaCl₂, 26.2 NaHCO₃, and 1.25 glucose. Brains were then rapidly removed and placed in the same aCSF at ~0 °C. Coronal slices (200 μm) containing the LH were cut on a Vibratome (VT-1200; Leica Microsystems, Buffalo Grove, IL). Following slicing, brain sections were placed in a holding chamber and allowed to recover for at least 30 min before being placed in the recording chamber and superfused with bicarbonate-buffered solution containing (in mM): 119 NaCl, 2.5 KCl, 1.0 NaH₂PO₄, 1.3 MgCl₂, 2.5 CaCl₂, 26.2 NaHCO₃, and 11 glucose (at 32 – 34 °C) and saturated with 95% O₂ and 5% CO₂. Cells were visualized using infrared differential contrast and fluorescence microscopy. Whole-cell recordings were performed using patch electrodes (3 – 5 MΩ) backfilled with a potassium-gluconate internal solution containing (in mM): 130 K-gluconate, 10 KCl, 10 HEPES, 10 EGTA, 2 MgCl₂, 2 ATP, 0.2 GTP; pH = 7.35, 270 – 285 mOsm. Whole-cell recordings of LH GABAergic neurons expressing hM3Dq-mCherry were performed using an Axopatch 700B amplifier (Molecular Devices, Sunnyvale, CA). All data were filtered at 2 kHz, digitized at 5 – 10 kHz, and collected using pClamp10 software (Molecular Devices, Sunnyvale, CA). Following stable 5-min whole-cell recordings (baseline), aCSF solution containing 5-μM CNO was perfused onto the brain slice.

Optogenetic Manipulations

All photostimulation experiments used 5-ms, 473-nm light pulses at 10 – 15 mW and 20 Hz. Constant 532-nm light delivery at 10 – 15 mW was used for all photoinhibition experiments. All *in vivo* optogenetic manipulations used a solid-state laser for light delivery (Shanghai Laser & Optics Century, Shanghai, China).

Chemogenetic Manipulations

For *in vivo* chemogenetic activation experiments, LH^{GABA::}hM3Dq and LH^{GABA::}Control mice received i.p. injections of either CNO (1 mg/kg in 0.5% DMSO/saline) or vehicle (0.5% DMSO/saline) 45 min prior to the start of all behavioral paradigms. Injections were counterbalanced and occurred 3 days apart from each other.

Free-access Feeding Task

Animals were placed in a custom two-chamber, 25 x 50 x 25 cm arena to assess the amount of food consumed and time spent in a designated food zone area. The arena contained two 160-cm² food cups in two outer corners of separate chambers. One cup contained standard grain-based chow (Harlan, Indianapolis, IN), while the other cup remained empty. Mice were free to explore the arena, and spatial locations were tracked using EthoVision XT 10 (Noldus, Leesburg, VA) and CCD cameras (SuperCircuits, Austin, TX). The initial and final weight of the food was recorded to determine the total amount of food consumed (g) after each session.

For optogenetic stimulation experiments, well-fed mice received 20 min each of pre-photostimulation, photostimulation, and post-photostimulation. Photoinhibition experiments were run with food-deprived mice that received 10 min each of pre-photoinhibition and photoinhibition twice (Laser: Off, On, Off, On). For chemogenetic manipulations, 45 min after receiving either vehicle or CNO, well-fed mice were run for 1 hr, while taCasp3 ablation experiments involved food-deprived animals that were also tested for 1 hr.

For Ca²⁺ imaging experiments, the arena contained two food cups (designated food zones) in the outer corners along with two non-food cups in the other corners. Cups contained a high-fat chow (Bio-Serv, Flemington, NJ), standard grain-based chow (Harlan, Indianapolis, IN), a non-food object (custom made with 3-D printer to imitate chow; MakerBot Replicator 2, Brooklyn, NY) or nothing. High-fat and grain-based chow were placed in opposite chambers and the arrangement of cups between animals were randomized. Food-restricted

LH^{GABA}::GCaMP6m mice freely explored the arena while spatial location and Ca²⁺ activity were recorded for 30 min.

Real-time Place Preference

LH^{GABA}::ChR2, LH^{GABA}::eArch3.0, and littermate control mice were tested in the real-time place preference assay. LH^{GABA}::ChR2 mice received constant 20-Hz photostimulation in the photostimulation-paired side, while LH^{GABA}::eArch3.0 mice received constant light delivery when crossing into the photoinhibition-paired side. Sessions ran for 20 min, and location was assessed with Ethovision XT 10 (Noldus, Leesburg, VA). See reference (Stamatakis and Stuber, 2012) for more information regarding this method.

Optical Self-Stimulation of LH GABAergic Neurons

LH^{GABA}::ChR2 mice were trained in a 20 x 17 x 12 cm operant chamber (Med Associates, St Albans, VT) to nose poke for photostimulation (3-s, 40-Hz optical pulse train) in a 1-hr fixed-ratio (FR1) session. Following training, LH^{GABA}::ChR2 mice were run in the same paradigm the next day to assess optical (3-s, 20-Hz optical pulse train) self-stimulation responses. Behavioral recording and experimental parameters were recorded and controlled by MED-PC IV (Med Associates, St Albans, VT). See reference (Jennings et al., 2013a, 2013b) for more details on this behavioral paradigm.

Free-access Caloric Consumption Assay

Food-restricted LH^{GABA}::hM3Dq, LH^{GABA}::taCasp3, and littermate control mice were placed in a 20 x 17 x 12 cm operant chamber (Med Associates) with free access to a bottle containing a calorie-dense reward (Ensure; Chicago, Illinois) for 1 hr. Each lick (consummatory response) was detected and recorded by MED-PC IV (Med Associates). LH^{GABA}::hM3Dq and LH^{GABA}::Control mice received either CNO or saline once stable licking was achieved (3 consecutive days of daily average lick responses within $\pm 10\%$).

Progressive-ratio 3 Task

Food restricted LH^{GABA::hM3Dq}, LH^{GABA::taCasp3}, and LH^{GABA::GCaMP6m} mice were trained on a daily FR1 schedule to nose poke for a calorie-dense solution (Ensure) in the same operant chamber described above. Following completion of FR1 training, mice were then tested in a progressive-ratio 3 (PR3) paradigm (1-hr duration) to assay motivational behavioral responses. The first nose poke resulted in the presentation of a neutral cue (light and tone for 3 s) followed by delivery of the caloric reward. Subsequent reward delivery required an additional three nose pokes from the previous cue's nose poke requirement, i.e., 1, 4, 7. Behavioral data (i.e., nose pokes, licks, and breakpoints) and session parameters were recorded and controlled with MED-PC IV. Breakpoint was defined as the highest number of successive nose pokes reached by an animal.

In vivo Ca²⁺ Imaging

Food-restricted LH^{GABA::GCaMP6m} mice underwent two imaging sessions (the free-access feeding assay and the PR3 motivation task), which were separated across multiple days. Before each imaging session, the microscope was connected to the magnetic baseplate on the cranium and fixed in place by the baseplate set screw while the animals were briefly anesthetized with isoflurane. Each animal was placed back into their home cage for 20 min to acclimate and recover from anesthesia prior to the start of both imaging sessions. In addition, the field of view was matched and measured across sessions for each animal by capturing a snapshot image of a micrometer slide (MicroBrightField Bioscience, Williston, VT) upon completion of each recording. Compressed grayscale tiff images (12 bit) were collected at 15 frames per second with an average exposure time of 66.56 ms using the Inscopix nVista *HD V2* software (Inscopix, Palo Alto, CA). Further, the analog gain on the image sensor was set between 2 and 4 while the LED power was maintained within the 10 to 20% transmission range (0.1 to 0.2 mW of blue light).

Image Processing

All image processing was performed using the Mosaic software (version 1.0.0b; Inscopix, Palo Alto, CA). First, a spatial downsampling of 16x (spatial binning factor of 4) was applied to each video sequence to reduce the large file size and decrease the processing time. To correct for lateral brain movement, each video sequence was registered to a single reference frame, which accurately represented the overall appearance of the entire video, by using the registration engine TurboReg (Ghosh et al., 2011; Thevenaz et al., 1998; Ziv et al., 2013). Next, a sub-region within the field of view was cropped within each video in order to remove post-registration black borders. A basic percent-change-over-baseline ($\Delta F/F_0$) movie was generated using the mean z-projection image of the entire movie as the reference (F_0) to normalize fluorescence signals to the average fluorescence of the whole frame. The video file size was reduced again by using a temporal binning factor of 3. Single Ca^{2+} signals were isolated and identified with an automated cell-sorting algorithm that employs independent and principal component analyses on the ($\Delta F/F_0$) movies (Mukamel et al., 2009). The spatial configuration of each identified unit as well as the temporal properties of their Ca^{2+} activity traces were visually inspected for quality control and to determine if the identified set of units accurately represented Ca^{2+} dynamics from individual cell bodies. Following manual inspection, each image from the identified units was thresholded to remove background noise. Lastly, for the free-access feeding data set, Ca^{2+} transients were defined by a Ca^{2+} event detection algorithm, which searches for Ca^{2+} spikes that possess a large-amplitude peak with a fast rise time and a slow decay – characteristic traits of Ca^{2+} spiking.

Ca²⁺ Data Analysis

For the free-access feeding task, custom MATLAB (Mathworks, Natick, MA) functions were used to spatially map Ca^{2+} events onto the behavioral arena. Subjects' locations were

mapped onto 0.33 x 0.33 cm bins of the arena when a Ca^{2+} event is captured. Bins were normalized based on the total time spent in each bin and a Gaussian filter was applied to create the final map. Food zone:Non-food zone (FZ:NFZ) ratios were calculated as the ratio between Ca^{2+} event rate in FZ and NFZ and then log transformed. Food-zone excited (FZe) and Food-zone inhibited (FZi) cells were classified as such based on whether their log-transformed ratio fell outside ± 1 standard deviation (S.D.) of the mean. S.D. values were smoothed using a moving average window of 0.6 s. Ca^{2+} data was aligned to behavioral events (licks and nose pokes) during the PR3 task using custom MATLAB functions. Nose poke events were included for analysis if they occurred outside reward cues and were at least 1 s away from a recorded lick to avoid contamination from other external stimuli. The first licks occurring after reward and more than 1 s away from any nose poke were defined as lick events (consumption). Cells were classified as being excited or inhibited by either lick or nose poke if a significant difference existed between the average activity 1.5 s before and after the behavioral event using a paired t-test.

Cell Registration

Registration of matched cells between sessions was based on nearest neighbors between FZ and PR3 cell maps obtained from Mosaic. Utilizing spatial maps from the free-access feeding paradigm as the reference image, cell maps from the PR3 task were registered to the reference image with the MATLAB Image Processing Toolbox (Mathworks, Natick, MA). Registered coordinates for PR3 cells were calculated by applying the registering transformation to existing coordinates.

To calculate nearest-neighbor cell distances between imaging sessions of the same animal, distances were measured from each cell in the free-access feeding paradigm to the most proximate cell acquired from the PR3 task. Nearest-neighbor cell distances within sessions were calculated by finding each cell's nearest neighbor from within the same

behavioral recording session. Based on these two metrics, pairs of neurons between FZ and PR3 sessions with a distance greater than 5 μm were considered distinct neurons. To match neurons between behavioral sessions, pairwise distances between FZ and PR3 neurons were calculated and sorted. Beginning with the shortest pair distance, pairs were discarded if either neuron in the pair was previously matched during sorting or their distance was greater than 5 μm .

Results

Optogenetic Stimulation and Inhibition of LH GABAergic Neurons Bidirectionally Modulate Feeding and Reward-Seeking Behavior

Given that non-selective electrical stimulation of the LH produces multiple behavioral responses, including feeding and positive reinforcement (Hoebel and Teitelbaum, 1962; Margules and Olds, 1962), and that a large proportion of LH neurons are thought to synthesize and release GABA to control energy balance (Karnani et al., 2013; Leininger et al., 2009, 2011; Rosin et al., 2003), we first explored the functional role of LH GABAergic neurons in modulating feeding and reward-related behaviors by using optogenetic techniques. Applying established viral procedures (Jennings et al., 2013b), we first expressed channelrhodopsin-2 (Boyden et al., 2005) conjugated to enhanced yellow fluorescent protein (ChR2-eYFP) selectively in LH GABAergic neurons (**Figures 4.1 A and B**) of *Vgat-IRES-Cre* mice (Vong et al., 2011), and implanted optical fibers directly above the LH for somata photostimulation (**Figures 4.1 C and S1A**). Approximately 4 weeks after surgery, we tested whether direct photostimulation of LH GABAergic neurons influenced feeding and reward-related behavioral phenotypes in *ad lib* fed mice. Photoactivation of these neurons at 20 Hz produced significant increases in time spent in a designated food area (**Figures 4.1 D and E**), food consumption (**Figure 4.1 F**), time spent in a location paired with photostimulation (**Figure 4.1 G**), and self-stimulation behavior (**Figure 4.1 H**). Next, we tested whether photoinhibition of LH GABAergic

neurons disrupted feeding and reward-related behaviors in food-restricted mice. Utilizing similar procedures as described above, we targeted a modified variant (Mattis et al., 2012) of the inhibitory opsin, archaerhodopsin-3 (eArch3.0-eYFP; Chow et al., 2010), to LH GABAergic neurons in *Vgat-IRES-Cre* mice (**Figures 4.1 I-K and Figure 4.1 B**). Photoinhibition of LH GABAergic neurons led to significant reductions in time spent in a designated food area (**Figures 4.1 L and M**), food consumption (**Figure 4.1 N**), and time spent in a location paired with photoinhibition (**Figure 4.1 O**). These data indicate that selective optogenetic modulation of neurochemically distinct LH GABAergic neurons influences both feeding *and* reward-related behavioral phenotypes.

Chemogenetic Activation of LH GABAergic Neurons Enhances Consummatory Behaviors

To confirm and expand upon the acute behavioral effects observed from optogenetic manipulations (**Figure 4.1**), we investigated if sustained activation of LH GABAergic neurons, over a longer timescale, influenced consumption and motivation to earn caloric rewards. Thus, we virally targeted the G_q-coupled excitatory designer receptor exclusively activated by designer drugs (DREADD), hM3Dq, to LH GABAergic neurons by injecting the Cre-inducible viral construct, AAV8-hSyn-DIO-hM3D(Gq)-mCherry (Krashes et al., 2011), into the LH of *Vgat-IRES-Cre* mice (LH^{GABA}::hM3Dq; **Figures 4.2 A and B**). The inert molecule, clozapine-N-oxide (CNO), selectively binds to hM3Dq and activates neurons through G_q signaling pathways (Alexander et al., 2009). Therefore, to verify CNO-mediated activation in LH^{GABA}::hM3Dq neurons, we performed whole-cell recordings in brain slices and found that the spontaneous firing rate of a subset of LH^{GABA}::hM3Dq neurons significantly increased upon CNO (5 μM) bath application (**Figures 4.2 C and D**). Additionally, we examined whether *in vivo* stimulation of LH GABAergic neurons, via systemic CNO administration, enhanced the expression of Fos, a marker for neuronal activity, within the LH. Intraperitoneal (i.p.) injections of CNO (1 mg/kg) in LH^{GABA}::hM3Dq mice significantly increased Fos expression in the LH compared to

LH^{GABA}::Control mice injected with CNO (**Figures 4.2 E-I**). To determine whether DREADD-mediated activation of LH GABAergic neurons affected consummatory behavior, mice were trained in a free-access caloric consumption task (1 hr duration) that permitted the quantification of lick responses at the delivery spout for a palatable caloric liquid reward. Chemogenetic activation of LH GABAergic neurons in LH^{GABA}::hM3Dq mice via CNO (1 mg/kg, i.p.) injection led to significant increases in the number of lick (consummatory) responses when compared to controls (**Figures 4.2 J and K**). In addition, CNO administration 45 min prior to a 1 hr free-access feeding task (**Figure 4.2 L**) enhanced food intake in well-fed LH^{GABA}::hM3Dq mice (**Figure 4.2 M**).

To examine whether chemogenetic activation of LH GABAergic neurons altered motivation to earn caloric rewards, we initially trained mice on a fixed-ratio of 1 (FR1) schedule, where each active nose poke resulted in the delivery of a palatable and calorie-dense liquid. Following stable behavioral responding, on subsequent sessions, LH^{GABA}::hM3Dq and LH^{GABA}::Control mice were either administered saline or CNO (counterbalanced) 45 min prior to progressive ratio 3 (PR3) test sessions, which is an established behavioral assay for measuring an animal's motivation to obtain caloric rewards (Krashes et al., 2011). Intriguingly, activation of these cells significantly increased lick responses (metrics of consumption) (**Figures 4.2 N and O**), but did not alter the number of active nose pokes nor the break point (metrics of motivation; **Figures 4.2 P and Q**). Anecdotally, we observed that LH^{GABA}::hM3Dq mice treated with CNO spent majority of the time licking at the reward receptacle (despite reward delivery being contingent upon nose poke responding), suggesting that bulk chemogenetic activation of these neurons may over-ride optimal behavioral performance by biasing behavior towards aspects of consumption. Taken together, these data indicate that chemogenetic activation of LH GABAergic neurons enhances consummatory behaviors.

Vgat-expressing LH neurons are molecularly distinct from MCH and Orx cells

The LH exclusively houses two separate molecularly defined cell types, melanin-concentrating hormone (MCH) and orexin (Orx) neurons, that are commonly associated with food intake, metabolic processes, reward, and sleep-wakefulness regulation (Adamantidis et al., 2007; Alon and Friedman, 2006; Borgland et al., 2009; Burdakov and Alexopoulos, 2005; Burdakov et al., 2005; Chemelli et al., 1999; Domingos et al., 2013; Elias et al., 1998; Jego et al., 2013; Karnani et al., 2011; Ludwig et al., 2001; Shimada et al., 1998; Whiddon and Palmiter, 2013; Willie et al., 2003). Thus, we labeled these peptide-containing neuronal populations in *Vgat-IRES-Cre* mice that endogenously expressed eYFP in *Vgat* neurons to determine if Orx and/or MCH neurons colocalize with *Vgat*-expressing LH cells and to verify that the evoked feeding effects from our opto/chemogenetic approaches were not due to genetic cross talk among common cells within the LH. Strikingly, immunostaining for MCH and Orx in *Vgat*-eYFP (*Vgat-IRES-Cre* mice crossed to a Ai3 reporter line) (Madisen et al., 2010) subjects revealed that eYFP in *Vgat*-positive LH neurons does not coexpress with either of these neuropeptides, signifying that LH GABAergic neuronal populations expressing *Vgat* are neurochemically distinct from MCH and Orx cells (**Figure 4.3 A-I**).

Genetic Ablation of LH GABAergic Neurons Reduces Consummatory Behaviors and Motivation to Obtain Caloric Rewards

Since optogenetic and chemogenetic activation of molecularly distinct LH GABAergic neurons is sufficient to enhance aspects of motivation and consumption, we next assessed the necessity of LH GABAergic neurons for regulating these feeding-related behaviors with cell-type specific ablation methods. To selectively ablate LH GABAergic neurons, we injected a Cre-inducible viral construct coding for taCasp3-2A-TEVp (AAV-flex-taCasp3-TEVp) into the LH of *Vgat-IRES-Cre* mice (LH^{GABA}::taCasp3; **Figure 4.4 A**). This virus uses a designer procaspase 3 (pro-taCasp3), which is only cleaved into its active apoptosis-inducing form (taCasp3) by the presence of tobacco etch virus protease (TEVp). Thus, only Cre⁺ neurons expressing both

taCasp3 and TEVp will undergo apoptosis (Yang et al., 2013). In agreement with this, *in situ* hybridization for GAD67, a marker for GABAergic neurons (Erlander et al., 1991), revealed a significant reduction in the number of LH GABAergic neurons following bilateral LH injections of AAV-flex-taCasp3-TEVp, and no change in the number of GABAergic neurons within neighboring regions, including the entopeduncular nucleus (EP) and ventromedial hypothalamus (VMH; **Figures 4.4 B-D**). Previous studies demonstrated that chemical or electrolytic lesions of the LH can result in significant aphagia and weight loss (Von Der Porten and Davis, 1979; Harrell et al., 1975; Schallert and Whishaw, 1978). Therefore, we monitored the daily body weight of LH^{GABA}::taCasp3 and LH^{GABA}::Control mice while both groups were maintained on a calorie-dense diet for 60 days. Ablation of LH GABAergic neurons markedly attenuated weight gain, as LH^{GABA}::taCasp3 mice possessed significantly less changes in body weight compared to controls (**Figure 4.4 E**). Additionally, LH^{GABA}::taCasp3 mice displayed significant reductions in daily food intake measured at one month post virus injection (**Figure 4.4 F**).

We next tested the effects of LH GABAergic neuron ablation on acute feeding and motivation to obtain caloric rewards. Food-restricted LH^{GABA}::taCasp3 mice showed reduced food intake in the acute free-access feeding assay (**Figures 4.4 G and H**) and reduced lick responding in the free-access caloric consumption task (**Figure 4.4 I**). When tested on the PR3 motivational task, LH^{GABA}::taCasp3 mice exhibited reduced lick responding compared to controls (**Figures 4.4 J and K**). Additionally, LH^{GABA}::taCasp3 mice showed a significant reduction in metrics of motivation (active nose pokes and breakpoints) compared to controls (**Figures 4.4 L-N**). Lastly, the number of MCH or Orx cells in the LH was not significantly altered in the LH^{GABA}::taCasp3 mice nor was their general locomotor activity affected from the genetic removal of LH GABAergic neurons (**Figures 4.4 O-V**). Together, these data highlight a causal and

distinct role for LH GABAergic neurons in regulating motivation, consumption, and energy balance.

In Vivo Ca²⁺ Imaging in Large Populations of LH GABAergic Neurons

The optogenetic, chemogenetic, and cell ablation experiments outlined above clearly demonstrate that bulk modulation of LH GABAergic neurons causally regulates motivated and consummatory behavioral output. Though these approaches provide important causal information for linking cell-type specific function to behavior, bulk modulation of even genetically defined neurons fails to account for the high degree of functional diversity within a defined cell population, nor do they accurately reflect endogenous cellular activity dynamics that underlie complex behaviors. Therefore, it is unclear whether motivated and consummatory processes are orchestrated by functionally discrete subpopulations of LH GABAergic neurons or whether individual neurons are participant in aspects of both motivation and consumption. To examine this in detail, we applied *in vivo* microendoscopic imaging strategies (Barretto et al., 2011; Deisseroth and Schnitzer, 2013; Flusberg et al., 2008; Ghosh et al., 2011; Jennings and Stuber, 2014) to resolve somatic Ca²⁺ activity dynamics from hundreds of LH GABAergic neurons (~740 cells) in freely behaving mice. First, we expressed the green fluorescent sensor of neuronal activity, GCaMP6m, in LH GABAergic neurons by injecting a Cre-inducible AAV viral construct (AAVDJ-EF1 α -DIO-GCaMP6m) into the LH of *Vgat-IRES-Cre* mice (LH^{GABA::GCaMP6m}; **Figures 4.5 A-C**). To circumvent the optical aberrations typically observed in deep brain structures like the LH (~5 mm deep), we implanted 8 mm long microendoscopes (0.5 mm diameter; consisting of a relay lens fused to doublet gradient-index microlenses) directly above the LH for optical detection of GCaMP6m fluorescence emission (**Figures 4.5 D-F**). Next, we interfaced the implanted microendoscope with a detachable miniaturized fluorescence microscope (Ghosh et al., 2011; Ziv et al., 2013) to visualize Ca²⁺ signals from large populations of LH GABAergic neurons in freely-moving LH^{GABA::GCaMP6m} mice (**Figure 4.5 G**).

Furthermore, applying this technique in conjunction with established computational algorithms (Mukamel et al., 2009), we were able to identify and track the Ca^{2+} activity from individual LH GABAergic neurons both within single recording sessions and across multiple days and behavioral tasks (**Figures 4.5 H and I**).

Food-Location Coding Profiles of LH GABAergic Neurons

To characterize the response profiles of individual LH GABAergic neurons during the same free-access feeding task used above, we recorded Ca^{2+} signals as food-restricted LH^{GABA::GCaMP6m} mice freely explored an arena that possessed discrete food-containing zones (FZ) in two of the outer corners (**Figure 4.6 A**). This approach allowed for a visual representation of discrete spatial Ca^{2+} responses (**Figures 4.6 B and C**) with some neurons exhibiting increased Ca^{2+} spiking in the presence of food (**Figures 4.6 B and D**) and others showing decreased Ca^{2+} transients while the animal was in the FZ (**Figures 4.6 C and E**). Further, we calculated a response ratio for each LH GABAergic neuron based on the frequency of Ca^{2+} responses in the FZ over the frequency in non-food zones (FZ to NFZ; **Figure 4.6 F**). We categorized response profiles from individual neurons as food zone excited (FZe) or food zone inhibited (FZi) if their FZ/NFZ ratios were $> \pm 1$ standard deviation of the mean (0.0 ± 0.3) of the entire population ($n = 612$ cells). Average responses to FZ and NFZ areas within FZe and FZi neurons revealed significant differences in their respective directions (**Figure 4.6 G**), supporting the design of our classification model. To spatially represent the response profiles of each neuron, we pseudocolored individual cells from an example animal's cell map by its log-transformed response ratio and observed that cells of differing response profiles intermingled with each other rather than segregating into separate clusters (**Figure 4.6 H**). These data demonstrate that the natural activity dynamics of subsets of LH GABAergic neurons are preferentially modulated in environmental locations paired with food.

Individual LH GABAergic Neurons Selectively Encode Aspects of Motivation or Consumption

Next we sought to determine whether individual LH GABAergic neurons selectively encode aspects of motivation and/or consumption. Thus, we tracked Ca^{2+} dynamics in LH GABAergic neurons during the same PR3 task described above, where $\text{LH}^{\text{GABA}}::\text{GCaMP6m}$ mice worked to obtain a caloric liquid reward. Numerous individual LH GABAergic neurons showed time-locked Ca^{2+} transients in response to either the first lick after reward delivery (consummatory responses) or unreinforced active nose pokes (motivational responses; **Figures 4.7 A and B**). We profiled all imaged neurons based on their differences between average Ca^{2+} activity 1.5 s before and after each behavioral event to quantify their responses to aspects of feeding. Comparable to neuronal responses to food-associated areas (FZ), LH GABAergic neurons displayed a variety of classifiable response profiles, such as cells that were modulated during reward consumption or immediately following active nose pokes (**Figures 4.7 C and D**). Thus, we categorized these neurons as excited or inhibited to a particular behavioral event (Consumption or Nose poke) if their Ca^{2+} activity 1.5 s before and after both events were statistically enhanced or suppressed. Averaging responses within excited and inhibited neurons to consummatory licks revealed separate subpopulations of neurons with distinct Ca^{2+} responses to consummatory licks (**Figure 4.7 E**). A much larger population of LH GABAergic neurons displayed significant Ca^{2+} signals time-locked to nose pokes (**Figure 4.7 F**), although amplitudes of these responses were lower compared to consumption responses. LH GABAergic neurons covered a diverse range of responses to consummatory licks and nose pokes, but we found that individual neurons that significantly respond to reward consumption were largely separate from those that respond to nose pokes (**Figures 4.7 G and H**). Taken together, these data demonstrate that functionally segregated subpopulations of LH GABAergic neurons encode aspects of motivation (nose poke responsive cells) or consumption, but rarely both.

Lastly, we explored the Ca^{2+} dynamics of the same neurons between both behavioral paradigms (free-access feeding and the PR3 nose-poke task) to determine if the same neurons that respond to the presence of food during the free-access feeding task respond to consummatory licks and/or nose pokes during the PR3 task. To accomplish this, we registered cell maps from the same animal between sessions (**Figures 4.8 A-C**) and applied a 5- μm cutoff between center points of paired cells based on the distribution of cells from the same imaging session (**Figure 4.8 D**) and the distance between cells of different sessions (**Figure 4.8 E**). Using these stringent criteria, only a subset of neurons imaged during the free-access feeding behavior were also detected in the PR3 task ($n = 68$ paired cells; **Figure 4.8 F**). Neurons tracked in both sessions were not localized to any portion of the field of view and showed no distinct anatomical pattern or layout (**Figures 4.8 G-I**). However, paired cells displayed a high degree of functional overlap in the schematized cell maps between sessions. A large proportion of FZe neurons that also respond to PR3 behavioral events (28/40 cells) displayed increased activity to either nose pokes or consummatory licks in the PR3 task, while a smaller portion of FZi neurons responded to PR3 events (**Figure 4.8 J**). These data reveal that subsets of LH GABAergic neurons functionally overlap between tasks that require different behavioral processes to obtain nutrients, signifying the flexibility and complexity of these neurons for modulating feeding.

Discussion

Historically, the LH has been viewed as a critical modulator of both feeding and motivation (Hoebel and Teitelbaum, 1962; Margules and Olds, 1962). However, the precise cell types and dynamics underlying these distinct behavioral outputs have remained a mystery. Here, we defined a functional role for LH GABAergic neurons in regulating food-seeking and consummatory behaviors by employing an array of cell-type specific modulator tools. Specifically, optogenetic and chemogenetic activation of LH GABAergic neurons was sufficient

to produce both feeding and reinforcement behaviors, while genetic ablation of LH GABAergic neurons suppressed these behavioral phenotypes, implying that the dual function of the LH GABAergic network is essential for specific aspects of feeding. Thus, these data provide causal evidence that genetically distinct GABAergic neuronal populations in the LH contribute to these separate, yet intertwined behavioral phenotypes observed from previous seminal studies.

To explain the functional diversity within the global LH GABAergic network, we monitored the endogenous activity patterns from individual LH GABAergic neurons during motivational and consummatory behavioral tasks. To accomplish this, we adapted new miniaturized microscopy technology combined with genetically engineered fluorescence sensors to detect real-time Ca^{2+} responses from hundreds of neurons in freely moving mice. For the first time, we visualized and mapped the topography, as well as, the activity dynamics of genetically distinct neurons within the LH. This approach revealed discrete subpopulations of LH GABAergic neurons that contained unique spatial food-coding profiles, as some cells showed Ca^{2+} excitation in the presence of food, while other neurons displayed minimal Ca^{2+} spiking when the animal was in close proximity to food. Furthermore, separate subsets of motivation-coding and consumption-coding ensembles exist within the LH GABAergic network, suggesting that subpopulations of LH GABAergic neurons function individually to control certain behavioral outputs. Thus, the LH GABAergic network can be viewed as a mosaic of functionally and computationally distinct cell types, each of which will require further definition and characterization. Nevertheless, these important computational differences among individual LH GABAergic neurons would have gone unnoticed if only bulk neuromodulator tools were employed, further underscoring the necessity of identifying the natural activity dynamics within a network to better understand the precise neural underpinnings of complex behavioral states.

Previous retrograde and anterograde tracing studies demonstrate strong connectivity between the LH and other feeding- and reward-associated brain regions that are also important

for motivated behaviors, including the hypothalamus, midbrain, hindbrain, and striatal structures (Adamantidis et al., 2011; Betley et al., 2013; Chaudhury et al., 2013; Gutierrez et al., 2011; Hahn and Swanson, 2012; Kempadoo et al., 2013; Leininger et al., 2011), implying that the selective-coding properties within separate LH GABAergic subpopulations might be input- and projection-dependent. Future studies are needed to investigate this matter in more detail by selectively isolating and recording these neurons with projection-specific viral approaches and/or with fiber photometry technology (Gunaydin et al., 2014) in order to further define the natural LH-circuit dynamics of motivation and consumption.

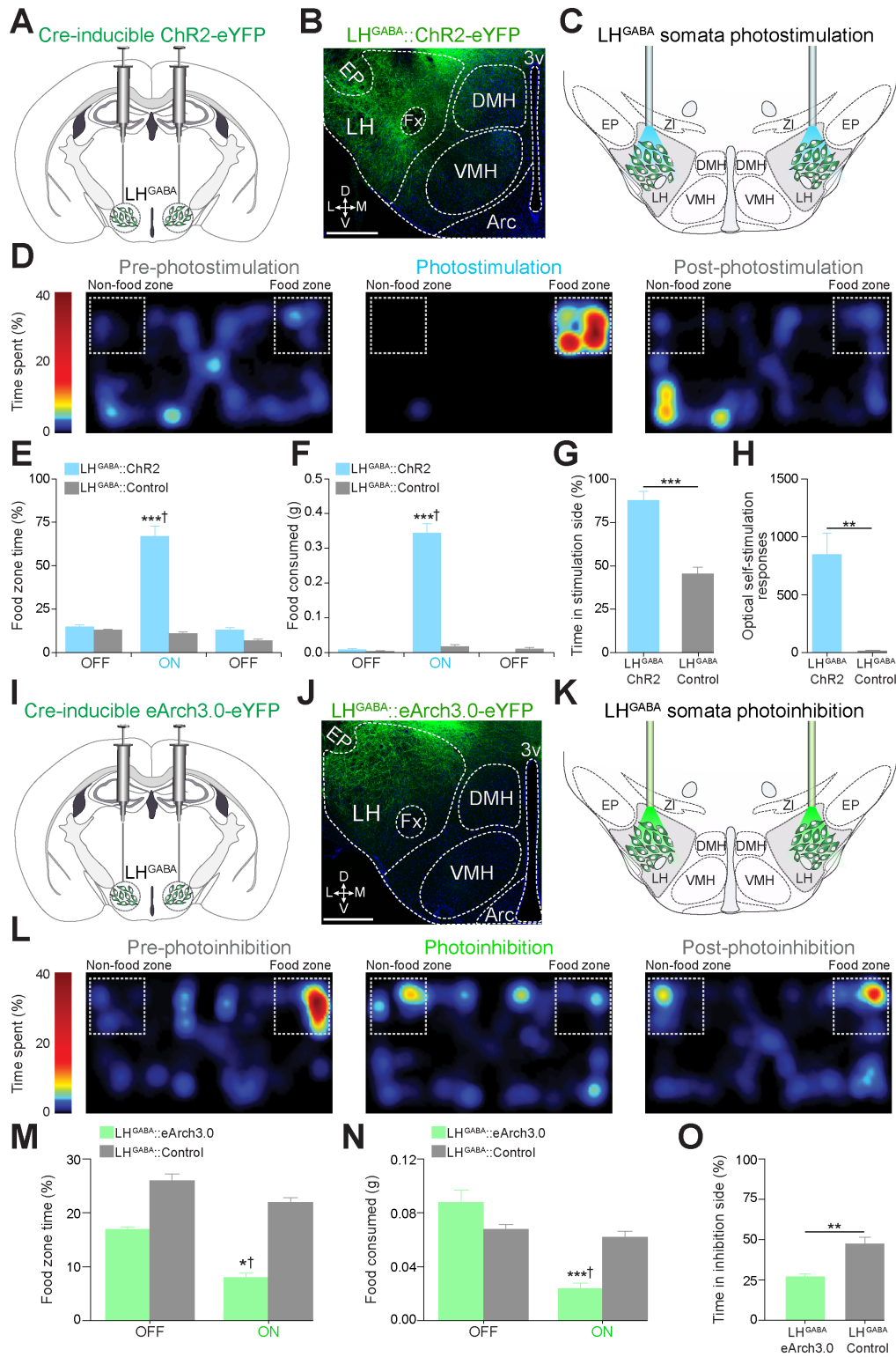


Figure 4.1: Optogenetic Modulation of LH GABAergic Neurons Bidirectionally Modulates Feeding and Reward-Related Behaviors. (A) Scheme for viral targeting of AAV5-EF1 α -DIO-ChR2-eYFP to the LH of *Vgat-IRES-Cre* animals. (B) 20x confocal image depicting localized ChR2-eYFP expression in LH GABAergic neurons. EP: entopeduncular nucleus, LH: lateral hypothalamus, Fx: fornix, DMH: dorsomedial hypothalamic nucleus, VMH: ventromedial hypothalamic nucleus, Arc: arcuate nucleus, 3v: third ventricle, D: dorsal, L: lateral, M: medial, V: ventral. Scale bar, 200 μ m. (C) Diagram for photostimulation of LH GABAergic neurons expressing ChR2-eYFP. EP: entopeduncular nucleus, ZI: zona incerta, LH: lateral hypothalamus, DMH: dorsomedial hypothalamic nucleus, VMH: ventromedial hypothalamic nucleus. (D) Color map encoding spatial location from a well-fed LH^{GABA::}ChR2 animal during a free-access feeding paradigm. Food and non-food zones are demarcated by white dashed lines. Color maps represent a 20-min pre-photostimulation phase (left), 20-min photostimulation (20 Hz) phase (middle), and 20-min post-photostimulation phase (right). (E) Photoactivation of LH GABAergic neurons significantly increased time spent in the food zone when compared to controls (n = 5 mice per group, $F_{2,27} = 86.24$, $p < 0.0001$). (F) Photostimulation significantly increased food intake in LH^{GABA::}ChR2 mice compared to controls (n = 5 mice per group, $F_{2,27} = 169.3$, $p < 0.0001$). (G) LH^{GABA::}ChR2 animals spent significantly more time in the chamber paired with photostimulation compared to controls (n = 5 mice per group, $t_8 = 6.796$, $p < 0.0001$). (H) LH^{GABA::}ChR2 animals nose poked significantly more for 20-Hz photostimulation compared to controls (n = 4 mice per group, $t_5 = 5.744$, $p = 0.0012$). (I) Schematic illustrating bilateral injections of AAV5-EF1 α -DIO-eArch3.0-eYFP into the LH of *Vgat-IRES-Cre* animals. (J) 20x confocal image showing eArch3.0-eYFP expression in the LH of a *Vgat-IRES-Cre* animal. EP: entopeduncular nucleus, LH: lateral hypothalamus, Fx: fornix, DMH: dorsomedial hypothalamic nucleus, VMH: ventromedial hypothalamic nucleus, Arc: arcuate nucleus, 3v: third ventricle, D: dorsal, L: lateral, M: medial, V: ventral. Scale bar, 200 μ m. (K) Illustration for somata LH GABAergic photoinhibition. EP: entopeduncular nucleus, ZI: zona incerta, LH: lateral

hypothalamus, DMH: dorsomedial hypothalamic nucleus, VMH: ventromedial hypothalamic nucleus. **(L)** Color map encoding spatial location of an example food-deprived LH^{GABA}::eArch3.0 animal during a free-access feeding paradigm. Food and non-food zones are demarcated by white dashed lines. Color maps represent 10-min pre-photoinhibition (left), 10-min photoinhibition (middle), and 10-min post-photoinhibition epochs (right). **(M)** Upon photoinhibition exposure, LH^{GABA}::eArch3.0 animals spent significantly less time in the food zone compared to controls (n = 5 mice per group, $F_{1,16} = 6.94$, $p = 0.018$). **(N)** Photoinhibition of LH GABAergic neurons significantly suppressed food intake in food-restricted LH^{GABA}::eArch3.0 mice when compared to controls (n = 5 mice per group, $F_{1,16} = 27.17$, $p < 0.0001$). **(O)** LH^{GABA}::eArch3.0 animals spent significantly less time in the photoinhibition-paired chamber compared to controls (n = 5 mice per group, $t_8 = 4.512$, $p = 0.002$). All values are mean SEM. Student's t-test or ANOVA followed by Bonferroni post-hoc comparisons, * $p < 0.05$, ** $p < 0.01$, *** $p < 0.001$. Dagger symbol denotes significance compared to all manipulations.

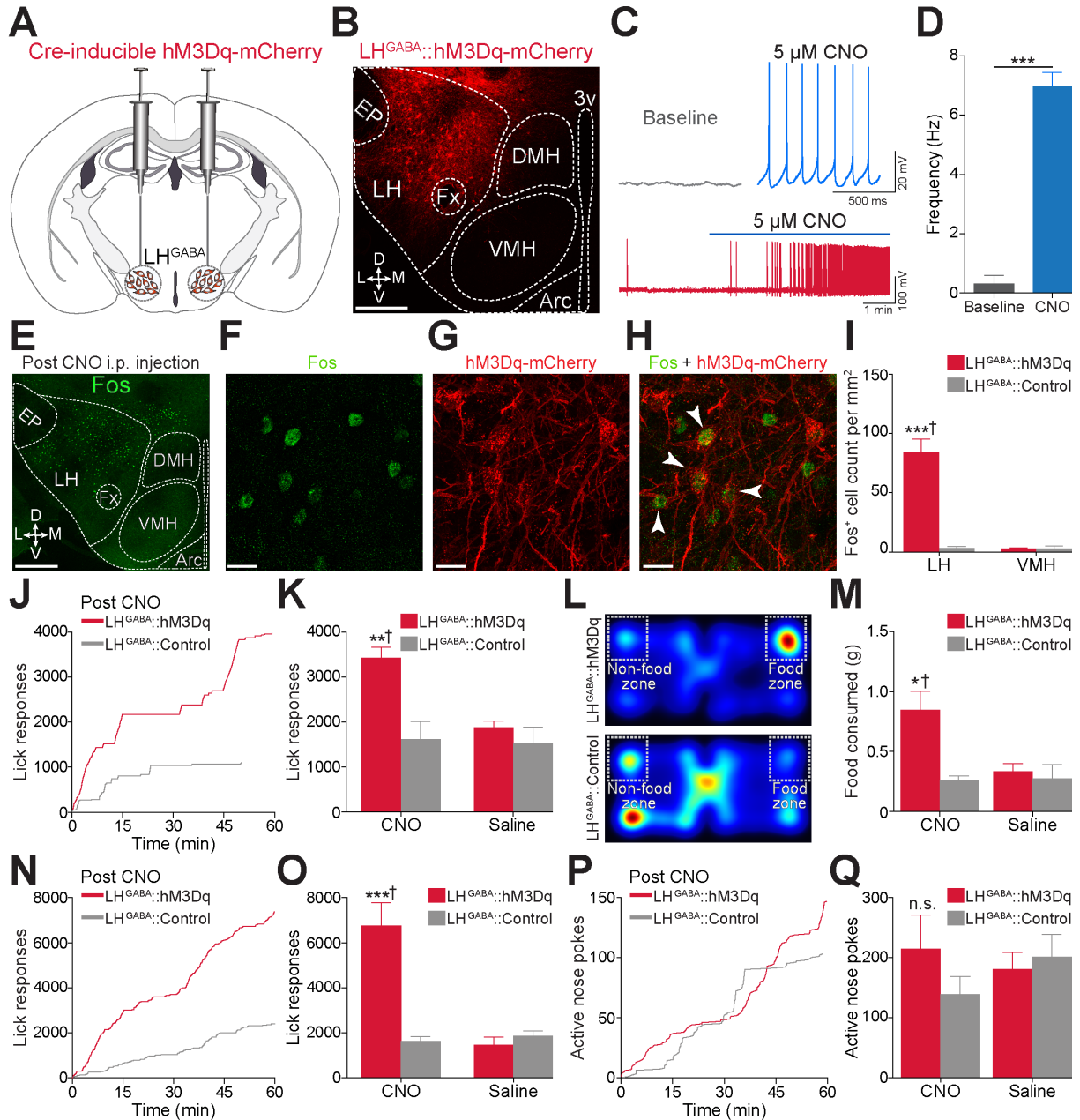


Figure 4.2: Bulk Chemogenetic Activation of LH GABAergic Neurons Enhances Consummatory Behaviors. (A) Schematic portraying viral injection of AAV8-hSyn-DIO-hM3D(Gq)-mCherry into the LH of *Vgat-IRES-Cre* mice. (B) 20x confocal image showing

hM3Dq-mCherry expression in the LH of a *Vgat-IRES-Cre* animal. EP: entopeduncular nucleus, LH: lateral hypothalamus, Fx: fornix, DMH: dorsomedial hypothalamic nucleus, VMH: ventromedial hypothalamic nucleus, Arc: arcuate nucleus, 3v: third ventricle, D: dorsal, L: lateral, M: medial, V: ventral. Scale bar, 200 μ m. **(C)** Example current-clamp traces from a LH^{GABA}::hM3Dq brain slice before (left) and after (right) CNO (5 μ M) bath application demonstrating DREADD-mediated action potentials (bottom). **(D)** CNO significantly increases spontaneous firing in LH^{GABA}::hM3Dq neurons (n = 3 cells, n = 3 mice, $t_4 = 12.370$, $p = 0.0002$). **(E)** 20x confocal image from an example LH^{GABA}::hM3Dq animal, where Fos-induction was assessed 2 hr after CNO (1 mg/kg; i.p.) injection. EP: entopeduncular nucleus, LH: lateral hypothalamus, Fx: fornix, DMH: dorsomedial hypothalamic nucleus, VMH: ventromedial hypothalamic nucleus, Arc: arcuate nucleus, 3v: third ventricle, D: dorsal, L: lateral, M: medial, V: ventral. Scale bar, 500 μ m. **(F-H)** 63x confocal images displaying Fos immunoreactivity **(F)** and hM3Dq-mCherry expression **(G)** in a LH^{GABA}::hM3Dq animal injected with CNO. **(H)** Merged image of **(F)** and **(G)** showing colocalization of Fos and hM3Dq-mCherry expression as indicated by white arrows. Scale bars, 20 μ m. **(I)** CNO administration in LH^{GABA}::hM3Dq mice significantly increases Fos expression in the LH compared to controls and neighboring regions (n = 3 mice per group, $F_{1,8} = 46.00$, $p < 0.0001$). **(J)** Cumulative lick responses from individual LH^{GABA}::hM3Dq and LH^{GABA}::Control mice during a single 1 hr free-access caloric consumption task. **(K)** Systemic CNO application significantly increases lick responses in LH^{GABA}::hM3Dq animals compared to LH^{GABA}::Control mice and saline injections during a free-access caloric consumption task (n = 6 mice per group, $F_{1,20} = 8.118$, $p = 0.009$). **(L)** Example color maps from LH^{GABA}::hM3Dq (top) and LH^{GABA}::Control mice (bottom) during the free-access feeding task. **(M)** Systemic application of CNO in LH^{GABA}::hM3Dq mice significantly increased food consumption during the free-access feeding task when compared to controls and saline injections (n = 6 mice per group, $F_{1,20} = 6.373$, $p = 0.020$). **(N)** Cumulative lick responses from example LH^{GABA}::hM3Dq and LH^{GABA}::Control animals during a single 1 hr progressive ratio 3

(PR3) session. **(O)** Systemic CNO application significantly increased lick responses in $LH^{GABA::hM3Dq}$ mice during the PR3 paradigm when compared to controls and saline injections ($n = 6$ mice per group, $F_{1,20} = 24.37$, $p < 0.0001$). **(P)** Nose poke responses from example $LH^{GABA::hM3Dq}$ and $LH^{GABA::Control}$ mice during a single PR3 session. **(Q)** CNO administration did not significantly affect nose poke responses during the PR3 session ($n = 6$ mice per group, $F_{1,20} = 1.471$, $p = 0.2393$). All values are mean SEM. Student's t-test or ANOVA followed by Bonferroni post-hoc comparisons, n.s. $p > 0.05$, * $p < 0.05$, ** $p < 0.01$, *** $p < 0.001$. Dagger symbol denotes significance compared to all manipulations.

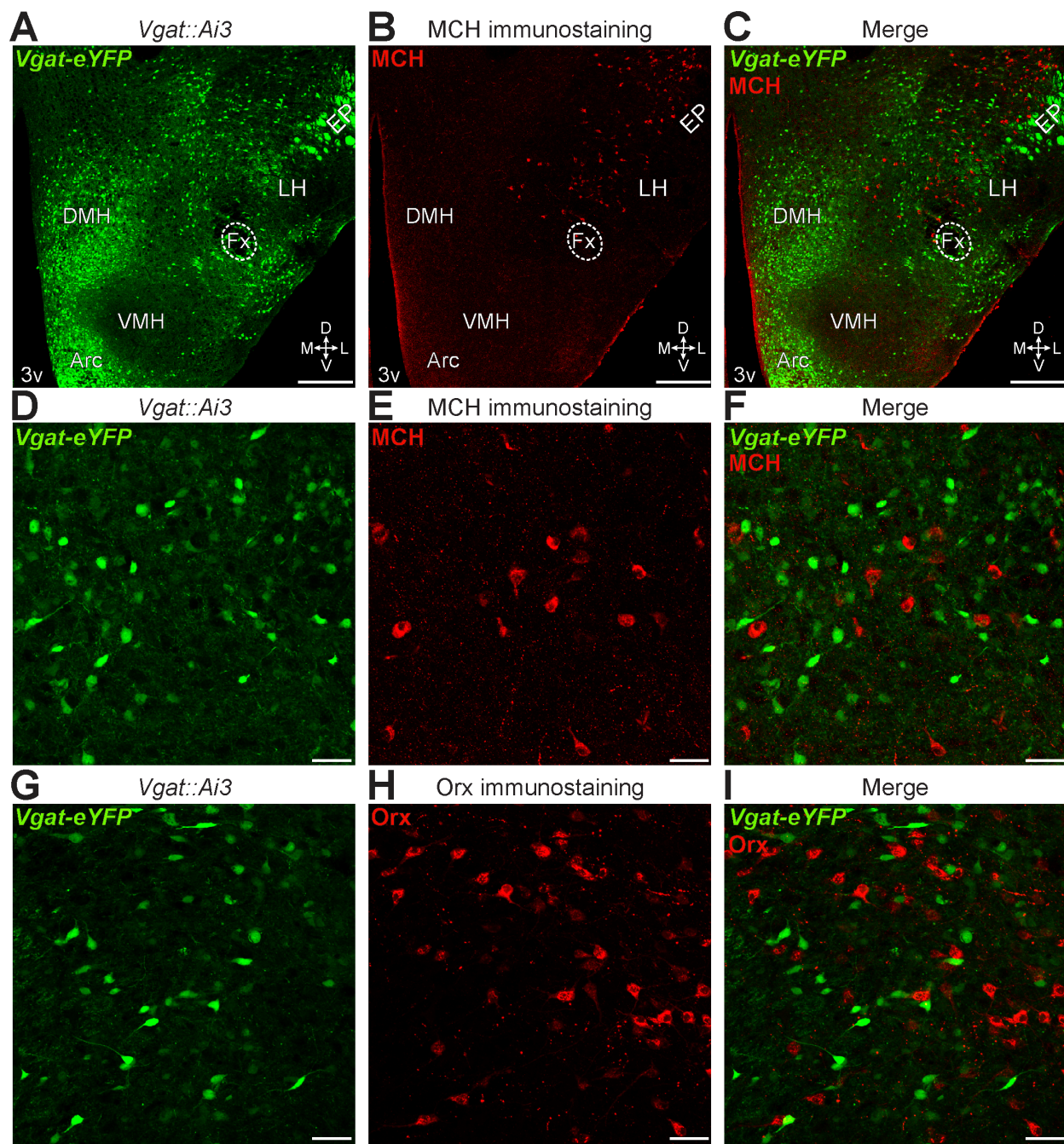


Figure 4.3: Neurochemically Distinct *Vgat* LH Neurons are Completely Separate From MCH and Orx Cells. (A and B) 20x confocal tile image from a *Vgat::Ai3* mouse expressing eYFP in all *Vgat*-positive neurons (A) with MCH immunolabeled in red (B). EP: entopeduncular nucleus, LH: lateral hypothalamus, Fx: fornix, DMH: dorsomedial hypothalamic nucleus, VMH: ventromedial hypothalamic nucleus, Arc: arcuate nucleus, 3v: third ventricle, D: dorsal, L:

lateral, M: medial, V: ventral. Scale bars, 200 μm . **(C)** Merge of **A** and **B** depicts the density and location of *Vgat* and MCH neurons within the LH. EP: entopeduncular nucleus, LH: lateral hypothalamus, Fx: fornix, DMH: dorsomedial hypothalamic nucleus, VMH: ventromedial hypothalamic nucleus, Arc: arcuate nucleus, 3v: third ventricle, D: dorsal, L: lateral, M: medial, V: ventral. Scale bar, 200 μm . **(D-F)** 20x confocal images of the dorsolateral LH represent no colocalization between *Vgat*-eYFP and MCH immunostaining (n = 223 +/- 13.77 *Vgat*-eYFP cells per mm^2 , n = 76 +/- 11.37 MCH cells per mm^2 , and 0% overlap, n = 3 sections, n = 3 mice). Scale bars, 200 μm . **(G-I)** A representative 20x confocal image from a *Vgat*-eYFP brain slice **(G)** immunostained for Orx **(H)** displays no overlap between *Vgat*-eYFP and Orx cells **(I)** (n = 3 sections, n = 3 mice). Scale bars, 200 μm .

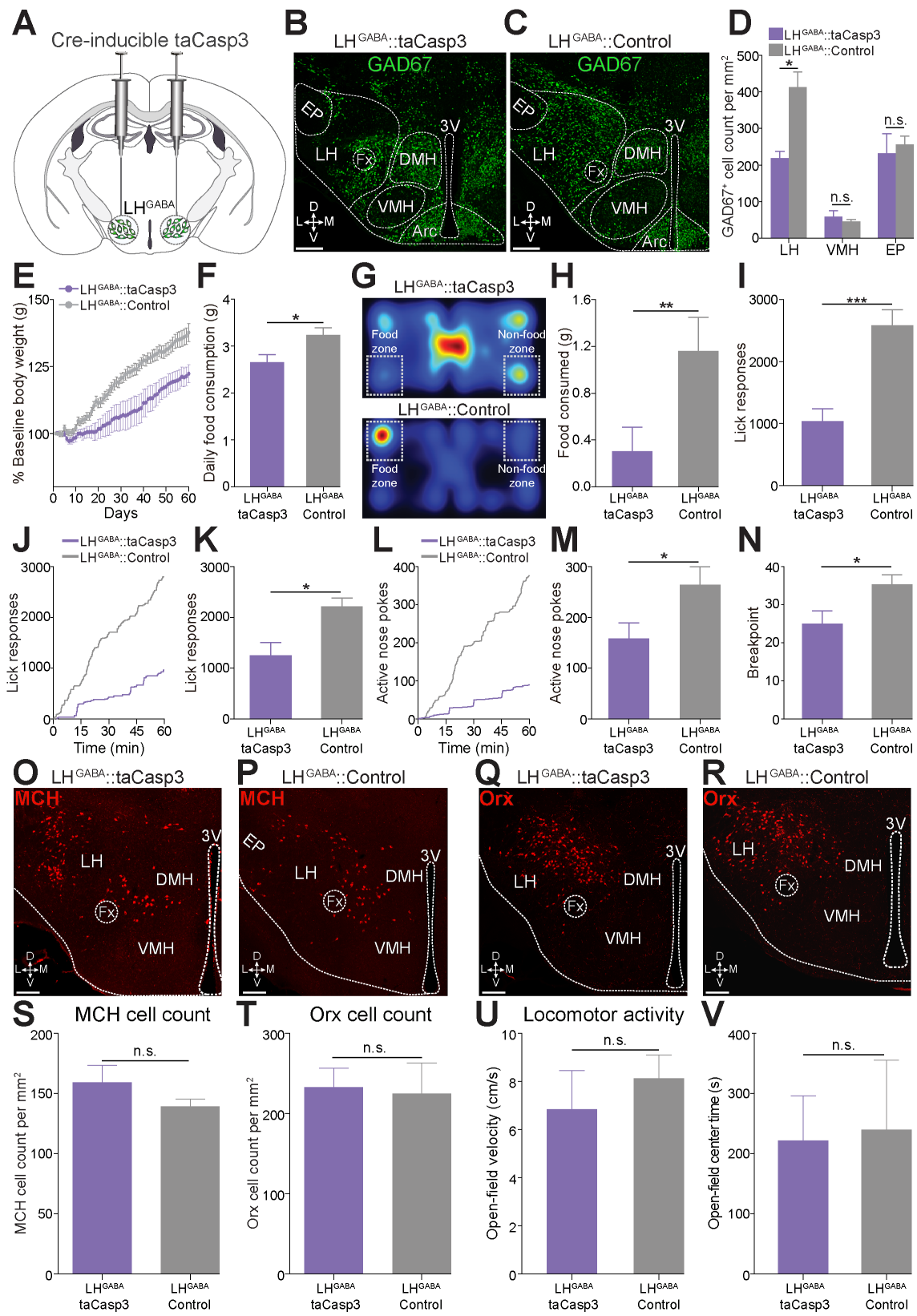


Figure 4.4: Genetic Ablation of LH GABAergic Neurons Attenuates Weight Gain, Food-seeking, and Consummatory Behaviors. (A) Schematic for viral injection of AAV2-flex-taCasp3-TEVp into the LH of *Vgat-IRES-Cre* animals. (B and C) 20x confocal images demonstrating decreased GAD67 expression in LH^{GABA::}taCasp3 mice (B) compared to LH^{GABA::}Control animals (C). EP: entopeduncular nucleus, LH: lateral hypothalamus, Fx: fornix, DMH: dorsomedial hypothalamic nucleus, VMH: ventromedial hypothalamic nucleus, Arc: arcuate nucleus, 3v: third ventricle, D: dorsal, L: lateral, M: medial, V: ventral. Scale bars, 200 μ m. (D) GAD67 expression is significantly decreased in the LH of LH^{GABA::}taCasp3 animals compared to LH^{GABA::}Controls (n = 3 mice per group, $t_4 = 3.860$, $p = 0.0182$). Ablation of LH GABAergic neurons does not significantly alter GAD67-expression levels within the VMH ($t_4 = 0.4559$, $p = 0.6721$) and EP ($t_4 = 0.01745$, $p = 0.98690$) of LH^{GABA::}taCasp3 and LH^{GABA::}Control mice. (E) Ablation of LH GABAergic neurons significantly blunted weight gain induced from a calorie-dense diet (n = 7 mice per group, $F_{1,720} = 377.01$, $p = 0.0174$). (F) Four weeks after taCasp3-TEVp viral injection, LH GABAergic cell death significantly reduced daily consumption of a calorie-dense diet (n = 7 mice per group, $t_{12} = 2.597$, $p = 0.0234$). (G) Color map locations from example LH^{GABA::}taCasp3 (top) and LH^{GABA::}Control (bottom) mice during the free-access feeding paradigm. (H) LH^{GABA::}taCasp3 mice display significant decreases in food consumption when compared to controls during the free-access feeding paradigm (n = 7 mice per group, $t_{12} = 3.239$, $p = 0.0071$). (I) LH GABAergic neuron ablation significantly decreases lick responses in LH^{GABA::}taCasp3 animals compared to controls during a free-access caloric consumption paradigm (n = 7 mice per group, $t_{12} = 5.3320$, $p = 0.0002$). (J) Lick responses from example LH^{GABA::}taCasp3 and LH^{GABA::}Control animals during a single (1 hr) PR3 session. (K) Ablation of LH GABAergic neurons significantly decreases lick responses in LH^{GABA::}taCasp3 animals compared to LH^{GABA::}Controls during the PR3 task (n = 6 mice per group, $t_{10} = 3.024$, $p = 0.012$). (L) Nose poke responses from example LH^{GABA::}taCasp3 and LH^{GABA::}Control animals during a single PR3 session. (M) Ablation of LH GABAergic neurons significantly decreases nose poke

responding in LH^{GABA}::taCasp3 animals compared to LH^{GABA}::Controls during the PR3 task (n = 6 mice per group, $t_{10} = 2.773$, $p = 0.019$). **(N)** LH^{GABA}::taCasp3 mice display significantly lower breakpoints when compared to LH^{GABA}::Controls during the PR3 session (n = 6 mice per group, $t_{10} = 2.692$, $p = 0.022$). **(O and P)** Representative 20x confocal images of the LH showing the lack of MCH cell removal in LH^{GABA}::taCasp3 **(O)** and LH^{GABA}::Control **(P)** mice. Scale bars, 50 μm . **(Q and R)** 20x confocal images of the LH depicting the absence of Orx cell death in LH^{GABA}::taCasp3 **(Q)** and LH^{GABA}::Control **(R)** mice. Scale bars, 50 μm . **(S)** Genetic ablation of LH GABAergic neurons does not significantly reduce the number of MCH neurons in the LH when compared to controls (n = 3 sections, n = 3 mice, $t_4 = 2.236$, $p = 0.089$). **(T)** Removal of LH GABAergic neurons does not significantly alter the Orx cell density in the LH when compared to controls (n = 3 sections, n = 3 mice, $t_4 = 0.3064$, $p = 0.7746$). **(U)** Open-field velocity was not significantly different between LH^{GABA}::taCasp3 and LH^{GABA}::Control animals (n = 6 mice per group, $t_{10} = 1.681$, $p = 0.1237$). **(V)** Open-field center time between LH^{GABA}::taCasp3 and LH^{GABA}::Control animals were not significantly different (n = 6 mice per group, $t_{10} = 0.3265$, $p = 0.7507$). Error bars represent SEM. Student's t-test, n.s. $p > 0.05$. All values are mean \pm SEM. Student's t-test or ANOVA followed by Bonferroni post-hoc comparisons, * $p < 0.05$, ** $p < 0.01$, *** $p < 0.001$.

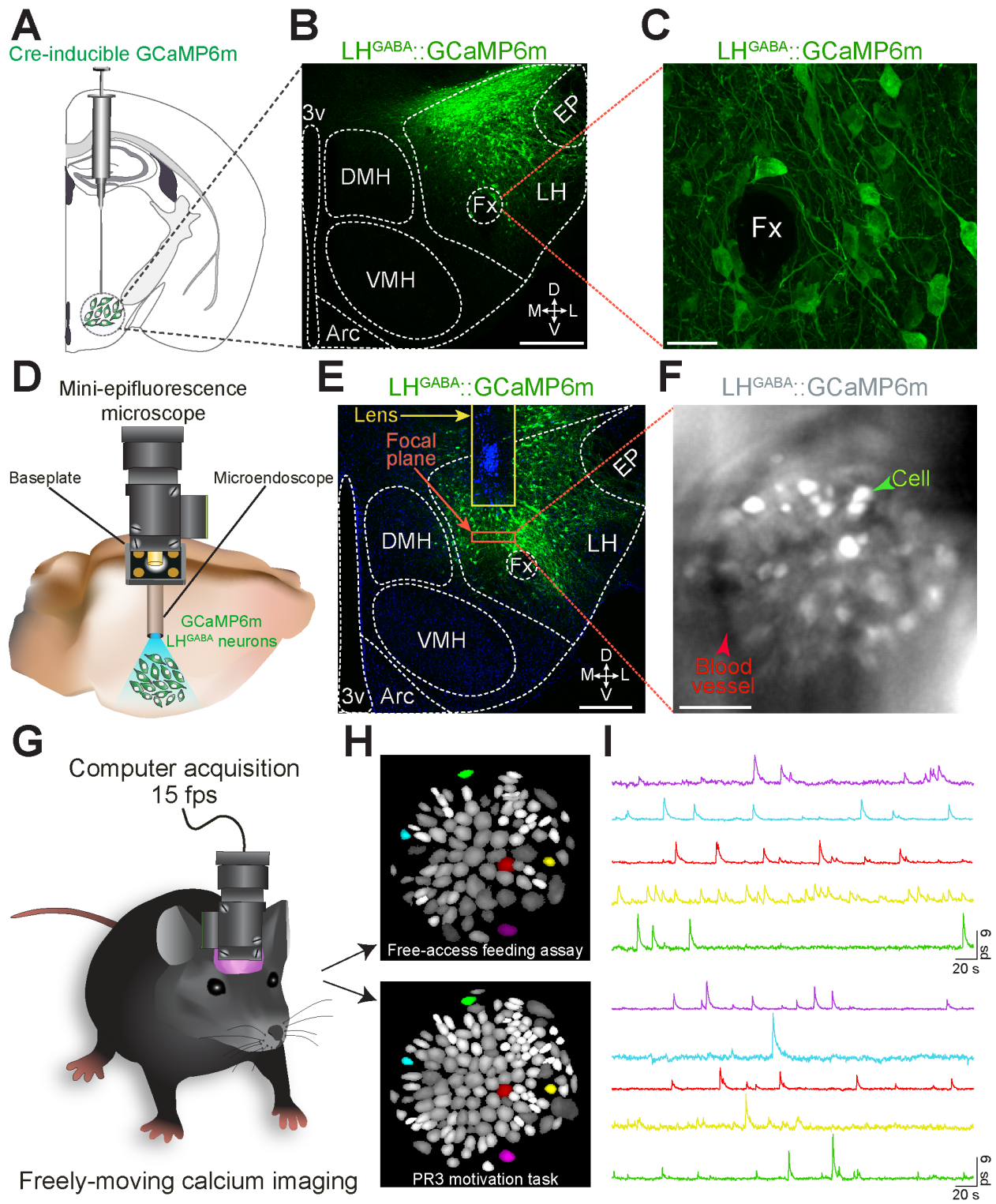


Figure 4.5: *In Vivo* Ca²⁺ Imaging of LH GABAergic Neurons in Freely Moving Mice. (A)

Diagram showing unilateral viral injection of AAVDJ-EF1 α -DIO-GCaMP6m into the LH of *Vgat-*

IRE5-Cre mice. (B) 10x confocal image of GCaMP6m expression in LH GABAergic neurons.

EP: entopeduncular nucleus, LH: lateral hypothalamus, Fx: fornix, DMH: dorsomedial

hypothalamic nucleus, VMH: ventromedial hypothalamic nucleus, Arc: arcuate nucleus, 3v: third

ventricle, D: dorsal, L: lateral, M: medial, V: ventral. Scale bar, 500 μ m. (C) 63x confocal image

demonstrating stable and healthy GCaMP6m expression in LH GABAergic neurons several

months after viral delivery. Fx: fornix. Scale bar, 20 μ m. (D) Integration of the mini-

epifluorescence microscope with the microendoscope for deep-brain imaging of LH GABAergic

neurons expressing GCaMP6m. (E) 20x confocal image showing lens (microendoscope)

placement and GCaMP6m-expressing neurons within the LH. Focal plane in tissue is 300 μ m

from the bottom of the lens as indicated by the dashed red box. EP: entopeduncular nucleus,

LH: lateral hypothalamus, Fx: fornix, DMH: dorsomedial hypothalamic nucleus, VMH:

ventromedial hypothalamic nucleus, Arc: arcuate nucleus, 3v: third ventricle, D: dorsal, L:

lateral, M: medial, V: ventral. Scale bar, 500 μ m. (F) *In vivo* mini-epifluorescence image of

GCaMP6m expression in the LH. Green arrow directs to a LH GABAergic neuron expressing

GCaMP6m. Red arrow highlights a blood vessel. Scale bar, 100 μ m. (G) Illustration of the *in*

vivo Ca²⁺ imaging setup. (H) Schematized cell map of an example animal's LH GABAergic

neurons visualized during free-access feeding and PR3 tasks. The same neurons can be

tracked between sessions (colored cells). (I) Ca²⁺ traces of individual neurons tracked in (H).

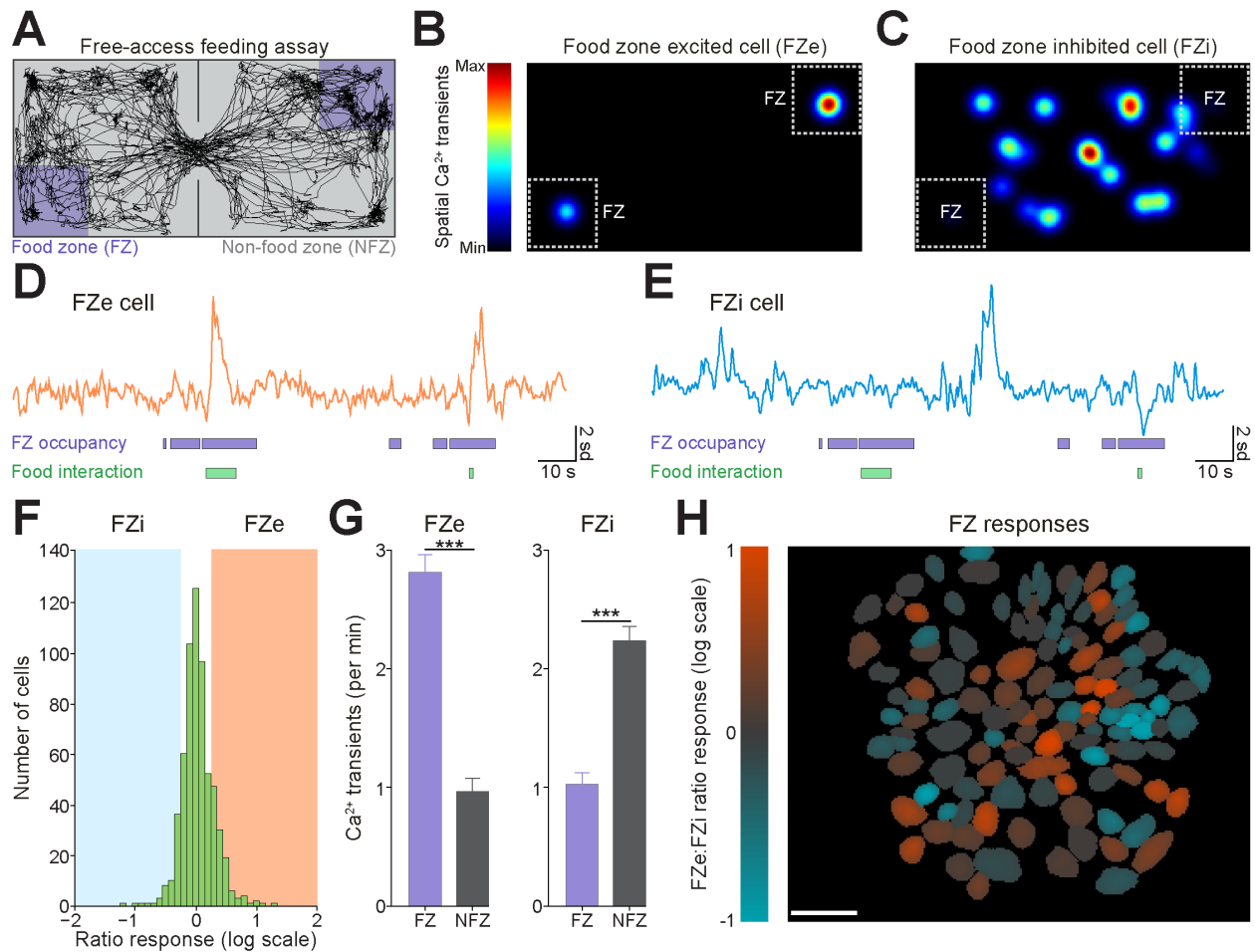


Figure 4.6: Subsets of LH GABAergic Neurons Display Enhanced or Reduced Activity to Environmental Locations Containing Food. (A) Example trace of animal's location during the free-access feeding task. (B and C) Spatial Ca^{2+} activity maps of a single FZe (B) and FZI (C) cell. Behavioral arena is divided into 0.33×0.33 cm bins, where number of Ca^{2+} events per unit time is represented in color. (D and E) Example Ca^{2+} traces from one FZe (orange; D) and one FZI (blue; E) cell during the free-access feeding task in relation to animal's location and state of interaction with food. (F) Distribution of food zone (FZ) responses from all detected

cells (mean = 0.0, sd = 0.3). FZe cells are classified as above one standard deviation (sd) from the mean. FZi cells fall below one standard deviation from the mean (n = 612 total cells imaged, n = 87 FZe cells, n = 73 FZi cells, n = 6 mice). **(G)** Average Ca^{2+} transients per min for FZe (left) and FZi (right) cells in each zone (n = 87 FZe cells, $t_{86} = 14.92$, $p < 0.0001$, n = 73 FZi cells, $t_{72} = 15.08$, $p < 0.0001$). **(H)** Example cell map with cells' color encoding response to FZ. Error bars represent SEM. Student's t-test, *** $p < 0.001$.

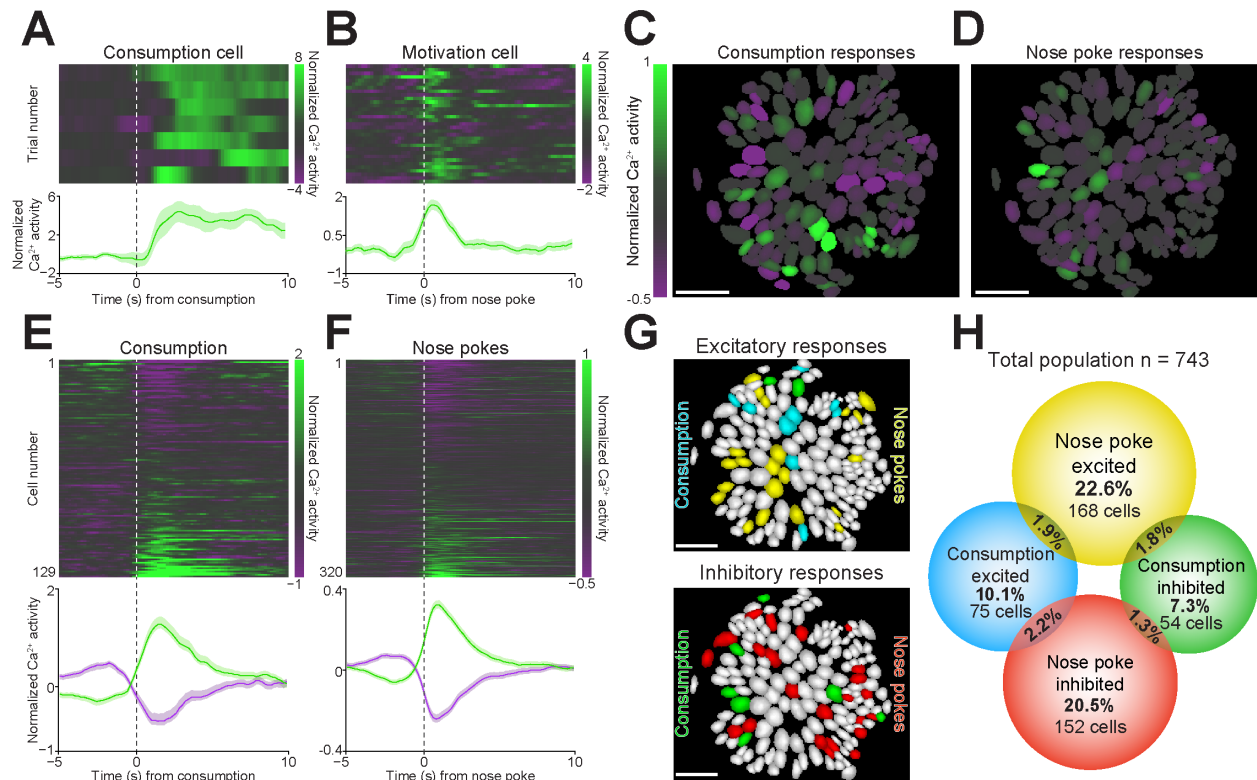


Figure 4.7: Separate LH GABAergic Neurons Selectively Encode Aspects of Motivation or Consumption. (A) Ca^{2+} response to consummatory licks from example animal. (Top) Ca^{2+} response to individual consummatory licks from an example cell. (Bottom) Average Ca^{2+} response to all consummatory licks from the example cell. (B) Ca^{2+} response to nose pokes from an example animal. (Top) Ca^{2+} response to individual nose pokes from an example cell. (Bottom) Average Ca^{2+} response to all nose pokes from the example cell. (C and D) Cell maps from example animal. Color codes consummatory lick response (average difference between Ca^{2+} signals from 1.5 s before and after lick) for each cell. Scale bars, 100 μm . (E) Average Ca^{2+} response to consummatory licks from all cells of all animals. (Top) Average Ca^{2+} response to consummatory licks from all cells. (Bottom) Ca^{2+} response to consummatory licks averaged

across either cells excited or inhibited by consummatory licks (n = 75 lick excited, n = 54 lick inhibited cells, n = 743 total cells). **(F)** Average Ca^{2+} response to nose pokes from all cells of all animals. (Top) Average Ca^{2+} response to nose pokes from all cells. (Bottom) Ca^{2+} response to nose pokes averaged across cells from either those excited or inhibited by nose pokes (n = 168 nose poke excited, n = 152 nose poke inhibited cells, n = 743 total cells). **(G)** Cell maps from example animal. (Top) Cells excited by consummatory licks (cyan), nose pokes (yellow), or both (green). (Bottom) Cells inhibited by consummatory licks (green), nose pokes (red), or both (yellow). Scale bars, 100 μm . **(H)** Venn diagram representing distribution and overlap of classified responsive cells in the PR3 task. Purple and green shaded regions represent SEM.

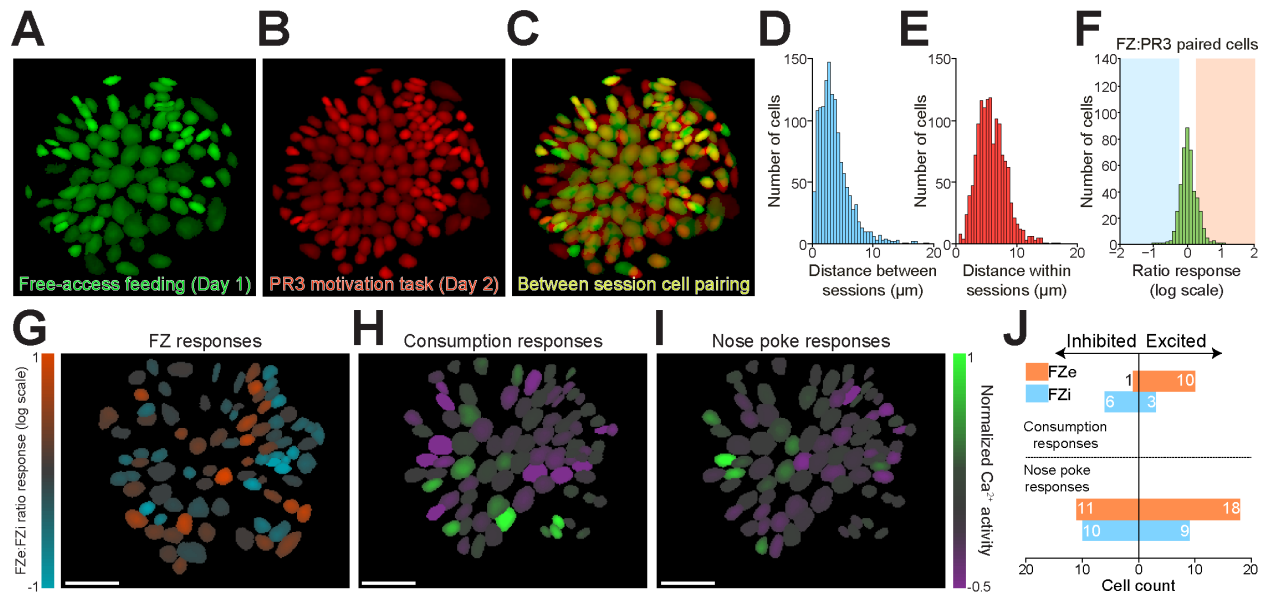


Figure 4.8: Tracking the Activity Dynamics of Individual LH GABAergic Neurons Across Separate Behavioral Tasks. (A) Cell map from example animal during free-access feeding task. (B) Cell map from same example animal during PR3 task. (C) Merge of free-access feeding and PR3 task cell maps from same example animal. (D) Distribution of nearest neighbor distances between cells of different behavioral tasks but same animal in all animals. (E) Distribution of nearest-neighbor distances between all cells within the same behavioral task and imaging session. (F) Distribution of cell responses in free-access feeding task of only paired cells ($n = 472$ cells from 6 mice, $n = 73$ FZe cells, $n = 52$ FZi cells.). (G-I) Maps of only paired cells from an example animal across the free-access feeding and PR3 tasks. Scale bars, $100 \mu\text{m}$. (J) Bar graph showing cells that respond in both the free-access feeding and PR3 tasks. Top portion shows cells that respond to FZ and consumption. Bottom portion shows cells that respond to FZ and nose pokes. Bars on the left represent cells that are inhibited by either consumption or nose pokes, while bars on the right represent cells that are excited by either consumption or nose pokes.

CHAPTER 5: DISCUSSION

General Discussion

Using ChR2 as a neuronal identifier and activator, we monitored and manipulated the activity of glutamatergic and GABAergic BNST-to-VTA neurons in freely moving mice. Optically-identified glutamatergic projection neurons displayed enhanced activity during aversive stimuli exposure, whereas the firing rate of GABAergic projection neurons was suppressed. ChR2-assisted circuit mapping revealed that both BNST-glutamatergic and -GABAergic projections preferentially innervate non-dopaminergic VTA neurons. Activation of BNST-glutamatergic projections resulted in aversive and anxiogenic behavioral phenotypes. In contrast, activation of BNST-GABAergic projections produced rewarding and anxiolytic phenotypes. Taken together, these data demonstrate that parallel, but functionally opposing, BNST-to-VTA circuits promote opposing behavioral states and serve as crucial circuit nodes for bidirectionally normalizing maladaptive behaviors.

Findings from this study will lay a foundation for investigating the precise neural circuit dynamics involved with addiction- and anxiety-related disorders. However, the limitations of *in vivo* extracellular recordings along with phototagging methods should be carefully recognized in future studies. The poor spatial resolution (~100 μm) of multielectrode arrays (Gray et al., 1995), which results in a low yield of detectable light-responsive units and thus limits the ability to record the neural activity from a large ensemble of neurons. For example, the small sample size obtained from extracellular recordings may not accurately represent the activity of the larger discrete neuronal population, as minor but important, subpopulations may exist within the

larger genetically defined network, leading to a plethora of various firing patterns to go unnoticed. The long-term performance of multielectrode arrays for chronic *in vivo* recordings can often diminish over time because of obstruction from scar tissue (gliosis), protein fouling, and increased electrode impedance (Cui et al., 2003; Edell et al., 1992; Turner et al., 1999). Also, the instability of the recording device in tissue prevents the unequivocal isolation of the same unitary signal on the same electrode across multiple recording sessions (Thompson and Best, 1990). This limitation in particular may greatly reduce insight into neural circuit function achieved by single unit recordings, as the activity patterns of unequivocally the same neuron cannot be observed over chronic time scales (days to months), where neuronal networks may adapt in response to stimuli or environmental demands. *In vivo* imaging of neuronal activity provides a complementary strategy to electrophysiological phototagging methods by defining the activity patterns of distinct participant neurons and axonal projections within a circuit over longer time scales. In particular, the development of fiber photometry offers a viable option for capturing projection-specific dynamics from genetically distinct circuits during complex freely-moving behavioral tasks. Importantly, this approach restricts *in vivo* measurements to a genetically and topologically distinct pathway, evading some of the unknown characteristics of antidromic phototagging methods, i.e. the possibility of photostimulating fibers of passage and not just terminal fields during extracellular recordings. Thus, future studies could employ fiber photometric approaches in combination with recently developed Ca^{2+} indicators to selectively monitor optical local field potentials (LFPs) from genetically distinct BNST to VTA projections (Gunaydin et al., 2014). We defined a causal role for the BNST to VTA pathway in regulating reward-related phenotypes, but we only recorded the activity of these projections during anxiety-related states. By employing photometric techniques, future investigations could monitor the activity dynamics of GABAergic and glutamatergic BNST to VTA projections during various reward-related behaviors to determine if these parallel circuits encode aspects of both anxiety and addiction in an opposite fashion. Based on our findings that GABAergic BNST neurons

decrease their firing rate in response to aversive stimuli and that activation of these projections is highly rewarding, I hypothesize that GABAergic BNST to VTA projections will display increased activity during reward-seeking tasks. An additional interesting follow-up study could involve the combination of fiber photometry with *in vivo* extracellular recordings for monitoring postsynaptic activity in the VTA, while concurrently detecting activity dynamics in their genetically-defined BNST inputs. To accomplish this, GCaMP6 is injected into the BNST and then a multielectrode array coupled to an optical fiber is inserted into the VTA. The only downside of this strategy is that the genetic identity of the postsynaptic cell type in the VTA would remain unknown and the temporal resolution between each method do not align, but it could serve as a starting point for understanding how behaviorally-relevant information is transmitted and integrated within a defined circuit.

The BNST also sends a dense projection to the LH, thus we sought to expand upon the functional roles of the BNST by dissecting its inhibitory projection to the LH. Whole-cell patch clamp recordings in conjunction with single-cell gene profiling of postsynaptic LH neurons revealed that BNST-GABAergic projection neurons predominantly target LH glutamatergic cells. Additionally, we used monosynaptic rabies viral strategies to further demonstrate that BNST neurons preferentially target LH glutamatergic cells. Activation of this inhibitory circuit rapidly evoked voracious feeding in sated mice and was highly reinforcing, while inhibition of the pathway suppressed feeding in hungry animals. These results reveal that inhibitory synaptic inputs from the extended amygdala preferentially innervate and suppress the activity of LH glutamatergic neurons to control food intake. Since the LH also contains a large population of GABAergic neurons (Karnani et al., 2013), we next aimed to determine whether this inhibitory network has an opposite role in feeding from LH glutamatergic neurons. Thus, do these neurons promote food-motivated and consummatory behavioral responses?

Optimally orchestrating complex behavioral states such as the pursuit and consumption of food is critical for an organism's survival. The LH is a multimodal brain region that is essential for both motivated and feeding behaviors, but whether individual neurons within the LH differentially contribute to aspects of feeding and motivation is unknown. We show that selective optogenetic or chemogenetic stimulation of LH GABAergic neurons enhances both motivation and feeding, while genetic ablation of these neurons reduced these behaviors. Using *in vivo* calcium imaging in freely behaving mice, we found that across hundreds of cells, individual LH GABAergic neurons preferentially encode aspects of either motivation or feeding, but rarely both. These tightly regulated, yet highly intertwined, processes are thus dissociable at the cellular level. Specific symptoms of a variety of neuropsychiatric disorders, therefore, may arise from maladaptive activity within select cellular subsets embedded within a larger genetically defined neuronal population.

Collectively, the toolsets and data provided here permit insight to previously inaccessible features of neural circuit dynamics and function, but several potential limitations underlying these methods hinder the specificity and temporal resolution of these findings. An important factor to consider is that numerous populations of LH neurons, including GABAergic cells, possess multiple traits and have diverse gene expression patterns that make them distinct from each other. Thus, targeting a cellular group based on one gene or feature is not sufficient for selectively perturbing or monitoring the discrete neural circuit elements underlying a particular behavior. An appropriate analogy describes a scenario where a detective is required to apprehend a criminal with only one minor description (brown hair) provided by a single witness. Obviously, the probability of identifying the culprit responsible for the crime increases when a witness and other environmental factors provide multiple details or descriptions.

Ideally, cell targeting based on multiple genetic factors could be utilized to isolate and refine the functional roles of these multifaceted neuronal networks within the LH. Recently,

Fenno and colleagues have made this possible by generating a versatile single-AAV system for selective expression that is conditional upon multiple genetic features of a particular cell type (Fenno et al., 2014). This method, also known as “intronic recombinase sites enabling combinatorial targeting” (INTRSECT) allows for targeting of cells that express two genes, which is useful for the LH since most of the peptide-containing LH neurons also coexpress *Vgat* or *Vglut2*. Therefore, applying this viral approach, future studies could parcel out the subsets of *Vgat* LH neurons that coexpress a certain peptide and compare their functional roles in feeding. Do these genetically distinct subtypes share similar functional and computational roles for feeding? Or do they have unique feeding-related processes that would otherwise go unnoticed with single gene targeting methods? Additional recombinases in transgenic mice, such as Flp or Dre, can be used to generate cell-type specific expression, and they can be combined with Cre-dependent targeting strategies to isolate genetically separate subpopulations within the same subject (Yizhar et al., 2011). However, this transgenic approach is less flexible than viral applications and requires a longer timescale for production, as new animal strains must be generated for each genetic tool.

Another crucial limitation to acknowledge is that optogenetic manipulations involve artificial stimulation parameters that produce unnatural physiological and behavioral responses. A more refined approach for establishing causality would involve stimulation parameters that are conditional upon natural activity dynamics of an adaptive or maladaptive behavioral state. In this context, if you mimic the precise activity patterns of a certain behavioral state, could you recapitulate the exact features of that state? If that is possible, then separate behavioral features could be parceled out further with specific activity-dependent stimulation of genetically defined circuits or networks. Also, is it possible to rescue a phenotype by only stimulating when the activity pattern passes below a certain threshold? Answering these types of questions for

anxiety and hunger circuits could reveal the precise causal signature of each state and possibly assist in the design of future therapeutic treatments for disorders related to these states.

Future additions to the color range of calcium indicator proteins (Akerboom et al., 2013), such as red fluorescent calcium indicators (RCaMP), will enable the integration of optogenetic neuronal activation and silencing manipulations with functional *in vivo* calcium imaging to control and monitor concurrently specific circuit interactions or connections (Akerboom et al., 2013). This integration will facilitate a biofeedback mechanism for controlling neurocircuit activity by allowing the natural circuit dynamics to direct the optogenetic manipulation parameters during behavioral tasks — frequency, duration, and the precise time point of stimulation or inhibition — instead of relying on the artificial control that is typically employed by the experimenter. The information provided by these types of experiments could inform future human applications that involve a biofeedback system paired with deep-brain stimulation, while also providing a real-time testable model of circuit function that encompasses both causal and correlative data. Advantageously, chromatic variants also allow for simultaneous multi-color activity imaging of multiple genetically distinct neuronal populations. As calcium transients can be detected in specific presynaptic terminals (Li et al., 2013), these new engineered set of chromatic variants may be utilized to simultaneously monitor the *in vivo* responses of a genetically defined postsynaptic neuron together with its presynaptic axon terminal input to reveal the precise mechanism by which information is transmitted and integrated between distinct cells within a circuit during a particular behavioral state. Moreover, these color-shifted indicators will further improve the imaging depth within intact brain tissue, since near-infrared light, containing longer wavelengths, scatters less through biological tissue (Jung et al., 2004).

Since the initial development of genetically encoded Ca^{2+} sensors (GCaMP) over a decade ago (Baird et al., 1999; Nakai et al., 2001), major improvements in both Ca^{2+} imaging devices and indicators have rapidly increased the possibility for *in vivo* visualization of neural

activity within genetically defined networks. Despite these advancements, Ca^{2+} indicators are still inadequate for accurately representing aspects of electrical activity. Currently, Ca^{2+} imaging approaches are unable to detect individual action potentials in fast-spiking neuronal populations since Ca^{2+} transients can persist for hundreds of milliseconds, even in the fastest Ca^{2+} indicator variant, GCaMP6f, which has a mean half decay time of approximately 140 ms (Chen et al., 2013). Furthermore, fluorescent protein-based Ca^{2+} sensors fail to account for sub-threshold membrane voltage dynamics. Sub-threshold membrane voltage dynamics may serve important computational roles in certain neuronal populations by acting as a 'neural activity gain' to influence synaptic responses on a gradient scale (Carter and Sabatini, 2004), but that remains to be determined with *in vivo* measurements. Lastly, these exogenous organic molecules buffer Ca^{2+} at an abnormal rate, which can disrupt natural neuronal function and increase the probability of cell death. In culmination, these limitations prevent Ca^{2+} imaging tactics from portraying a comprehensive mechanism for particular behavioral coding-schemes. Alternatively, fluorescent genetically encoded voltage sensors, such as "Accelerated Sensor of Action Potentials 1" (ASAP1; St-Pierre et al., 2014) and archaerhodopsin-based indicators (QuasAr1) (Hochbaum et al., 2014), are capable of reliably detecting rapid single action potentials (up to 200 Hz) and are suitable for acquiring sub-threshold voltage dynamics. Therefore, these recently developed techniques harvest great potential for diagramming a precise functional map of subcellular and circuit-level processing within defined and intact systems that were once considered as unattainable based on their fast activity profiles.

Lastly, the poor spatial resolution of existing *in vivo* imaging strategies prevents the acquisition of large-scale network information, which is imperative for attributing brain function to behavior. Circuit-level investigations are an important first step for identifying the neural underpinnings of certain disease states, but this microcosmic viewpoint limits our understanding of the brain. For instance, demonstrating that the connection between region A and B is

responsible for a single behavioral output only provides one small piece of the puzzle and does not account for all the other circuits that directly or indirectly alter this behavior. What upstream region/s are controlling A? And what is controlling that controller? Is there one master controller? Attempting to answer these questions one at a time at the A to B circuit level could result in a full circle, where we are left just as confused as when we first started the process. This process becomes extremely muddled since a lot of brain regions are reciprocally connected either directly or indirectly. Instead, the functional connection between A and B should be investigated in the context of all the other circuits. To achieve this goal, neuroscience must advance *in vivo* measurements to the level of the whole brain and not limit itself to one region or circuit connection. However, the turbidity of mammalian brain tissue makes this nearly impossible for current *in vivo* imaging applications. Conversely, Zebrafish (*Danio rerio*) are genetically tractable vertebrate model systems that offer optical clearance for visualizing *in vivo* whole-brain activity with cellular resolution (Ahrens et al., 2013). Thus, going forward I will take advantage of these key traits by imaging whole-brain activity in relevant zebrafish disease models with recently engineered light-field microscopy techniques.

The recent resurgence of light-field microscopy for imaging biological materials by the laboratories of Karl Deisseroth and Marc Levoy has generated tremendous potential for acquiring rapid three-dimensional data, as this technique does not require the traditional scanning methods used by other imaging systems, i.e. two-photon, confocal, and light-sheet microscopes. Critical neural processing information is most likely lost from the delay that is accompanied with each optical sectioning scan, but light-field devices prevent this scanning-induced delay. Light-field imaging involves an array of microlenses that are positioned at the intermediate image plane of a microscope (in front of the image sensor; Broxton et al., 2013). The array of small lenses captures three-dimensional structural data in a single snapshot and at a single time point by rendering angular rays into a field of light. These three-dimensional focal

stacks are then converted into a large three-dimensional volumetric image by using deconvolution algorithms (Levoy, 2010). This concept also holds true for hand-held consumer cameras and camera arrays, as they can generate a light field to reconstruct a three-dimensional scene observed in photos (Davis et al., 2012; Yang et al., 2002). Taken together, light-field microscopy can offer high-speed large volumetric information at the cellular level and may rapidly expand upon current imaging technology for acquiring structural- and activity-related information within an intact neurocircuit, since it can provide simultaneous three-dimensional data. Therefore, as a postdoctoral fellow, I plan to employ this cutting-edge technique to image *in vivo* large-scale neural activity in zebrafish, while also using novel opsins to simultaneously photomanipulate at the single cell level within a genetically defined network. I hope to manipulate single nodes within a circuit under the strict guidance of the natural activity dynamics detected during imaging. With this approach, it will be interesting to see how many neurons are required to generate one response or phenotype, and also to figure out how flexible and important specific activity patterns are for controlling not only certain behavioral outputs, but also for brain-wide functions.

In conclusion, the current renaissance in systems neuroscience has been fueled by innovative technologies that can synergistically be applied to dissect neural circuit function. These collaborative approaches will continue to transform our understanding of the function of genetically defined neural circuits. While the neurotechnology used and described here open the door to experimentation that would have been considered in the realm of science fiction a decade ago, the possibility exists that unforeseen limitations with these approaches will arise as they are more widely adopted. Thus, continued refinement of these tactics and scientific vigilance are critical to ensure these methods do not produce erroneous discoveries.

REFERENCES

- Abler, B., Grön, G., Hartmann, A., Metzger, C., and Walter, M. (2012). Modulation of frontostriatal interaction aligns with reduced primary reward processing under serotonergic drugs. *J. Neurosci. Off. J. Soc. Neurosci.* *32*, 1329–1335.
- Acuna-Goycolea, C., Tamamaki, N., Yanagawa, Y., Obata, K., and Pol, A.N. van den (2005). Mechanisms of Neuropeptide Y, Peptide YY, and Pancreatic Polypeptide Inhibition of Identified Green Fluorescent Protein-Expressing GABA Neurons in the Hypothalamic Neuroendocrine Arcuate Nucleus. *J. Neurosci.* *25*, 7406–7419.
- Adamantidis, A., and de Lecea, L. (2009). The hypocretins as sensors for metabolism and arousal. *J. Physiol.* *587*, 33–40.
- Adamantidis, A.R., Zhang, F., Aravanis, A.M., Deisseroth, K., and de Lecea, L. (2007). Neural substrates of awakening probed with optogenetic control of hypocretin neurons. *Nature* *450*, 420–424.
- Adamantidis, A.R., Tsai, H.-C., Boutrel, B., Zhang, F., Stuber, G.D., Budygin, E.A., Touriño, C., Bonci, A., Deisseroth, K., and de Lecea, L. (2011). Optogenetic interrogation of dopaminergic modulation of the multiple phases of reward-seeking behavior. *J. Neurosci. Off. J. Soc. Neurosci.* *31*, 10829–10835.
- Adelsberger, H., Garaschuk, O., and Konnerth, A. (2005). Cortical calcium waves in resting newborn mice. *Nat. Neurosci.* *8*, 988–990.
- Ahrens, M.B., Orger, M.B., Robson, D.N., Li, J.M., and Keller, P.J. (2013). Whole-brain functional imaging at cellular resolution using light-sheet microscopy. *Nat. Methods* *10*, 413–420.
- Akerboom, J., Rivera, J.D.V., Guilbe, M.M.R., Malavé, E.C.A., Hernandez, H.H., Tian, L., Hires, S.A., Marvin, J.S., Looger, L.L., and Schreier, E.R. (2009). Crystal Structures of the GCaMP Calcium Sensor Reveal the Mechanism of Fluorescence Signal Change and Aid Rational Design. *J. Biol. Chem.* *284*, 6455–6464.
- Akerboom, J., Chen, T.-W., Wardill, T.J., Tian, L., Marvin, J.S., Mutlu, S., Calderón, N.C., Esposti, F., Borghuis, B.G., Sun, X.R., et al. (2012). Optimization of a GCaMP Calcium Indicator for Neural Activity Imaging. *J. Neurosci.* *32*, 13819–13840.
- Akerboom, J., Carreras Calderon, N., Tian, L., Wabnig, S., Prigge, M., Tolo, J., Gordus, A., Orger, M.B., Severi, K.E., Macklin, J.J., et al. (2013). Genetically encoded calcium indicators for multi-color neural activity imaging and combination with optogenetics. *Front. Mol. Neurosci.* *6*.
- Alexander, G.M., Rogan, S.C., Abbas, A.I., Armbruster, B.N., Pei, Y., Allen, J.A., Nonneman, R.J., Hartmann, J., Moy, S.S., Nicoletis, M.A., et al. (2009). Remote control of neuronal activity in transgenic mice expressing evolved G protein-coupled receptors. *Neuron* *63*, 27–39.
- Alheid, G.F. (2003). Extended amygdala and basal forebrain. *Ann. N. Y. Acad. Sci.* *985*, 185–205.

- Alheid, G.F., and Heimer, L. (1988). New perspectives in basal forebrain organization of special relevance for neuropsychiatric disorders: the striatopallidal, amygdaloid, and corticopetal components of substantia innominata. *Neuroscience* 27, 1–39.
- Allen, G.V., and Cechetto, D.F. (1995). Neurotensin in the lateral hypothalamic area: origin and function. *Neuroscience* 69, 533–544.
- Allison, D.B., Fontaine, K.R., Manson, J.E., Stevens, J., and VanItallie, T.B. (1999). Annual deaths attributable to obesity in the United States. *JAMA J. Am. Med. Assoc.* 282, 1530–1538.
- Alon, T., and Friedman, J.M. (2006). Late-onset leanness in mice with targeted ablation of melanin concentrating hormone neurons. *J. Neurosci. Off. J. Soc. Neurosci.* 26, 389–397.
- ANAND, B.K., and BROBECK, J.R. (1951). Localization of a “feeding center” in the hypothalamus of the rat. *Proc. Soc. Exp. Biol. Med. Soc. Exp. Biol. Med. N. Y. N* 77, 323–324.
- Anand, B.K., and Brobeck, J.R. (1951). Hypothalamic Control of Food Intake in Rats and Cats. *Yale J. Biol. Med.* 24, 123–140.
- Ángeles-Castellanos, M., Mendoza, J., and Escobar, C. (2007). Restricted feeding schedules phase shift daily rhythms of c-Fos and protein Per1 immunoreactivity in corticolimbic regions in rats. *Neuroscience* 144, 344–355.
- Anstrom, K.K., and Woodward, D.J. (2005). Restraint Increases Dopaminergic Burst Firing in Awake Rats. *Neuropsychopharmacology* 30, 1832–1840.
- Anstrom, K.K., Miczek, K.A., and Budygin, E.A. (2009). Increased phasic dopamine signaling in the mesolimbic pathway during social defeat in rats. *Neuroscience* 161, 3–12.
- Armbruster, B.N., Li, X., Pausch, M.H., Herlitze, S., and Roth, B.L. (2007). Evolving the lock to fit the key to create a family of G protein-coupled receptors potently activated by an inert ligand. *Proc. Natl. Acad. Sci.* 104, 5163–5168.
- Atasoy, D., Aponte, Y., Su, H.H., and Sternson, S.M. (2008). A FLEX Switch Targets Channelrhodopsin-2 to Multiple Cell Types for Imaging and Long-Range Circuit Mapping. *J. Neurosci.* 28, 7025–7030.
- Atasoy, D., Betley, J.N., Su, H.H., and Sternson, S.M. (2012). Deconstruction of a neural circuit for hunger. *Nature* 488, 172–177.
- Back, S.E., and Brady, K.T. (2008). Anxiety Disorders with Comorbid Substance Use Disorders: Diagnostic and Treatment Considerations. *Psychiatr. Ann.* 38, 724–729.
- Baird, G.S., Zacharias, D.A., and Tsien, R.Y. (1999). Circular permutation and receptor insertion within green fluorescent proteins. *Proc. Natl. Acad. Sci. U. S. A.* 96, 11241–11246.
- Baker, P.F., Hodgkin, A.L., and Ridgway, E.B. (1971). Depolarization and calcium entry in squid giant axons. *J. Physiol.* 218, 709–755.

- Barretto, R.P.J., Ko, T.H., Jung, J.C., Wang, T.J., Capps, G., Waters, A.C., Ziv, Y., Attardo, A., Recht, L., and Schnitzer, M.J. (2011). Time-lapse imaging of disease progression in deep brain areas using fluorescence microendoscopy. *Nat. Med.* *17*, 223–228.
- Bayer, H.M., and Glimcher, P.W. (2005). Midbrain Dopamine Neurons Encode a Quantitative Reward Prediction Error Signal. *Neuron* *47*, 129–141.
- Berthoud, H.-R., and Münzberg, H. (2011). The lateral hypothalamus as integrator of metabolic and environmental needs: from electrical self-stimulation to opto-genetics. *Physiol. Behav.* *104*, 29–39.
- Betley, J.N., Cao, Z.F.H., Ritola, K.D., and Sternson, S.M. (2013). Parallel, redundant circuit organization for homeostatic control of feeding behavior. *Cell* *155*, 1337–1350.
- Bittencourt, J.C., Presse, F., Arias, C., Peto, C., Vaughan, J., Nahon, J.L., Vale, W., and Sawchenko, P.E. (1992). The melanin-concentrating hormone system of the rat brain: an immuno- and hybridization histochemical characterization. *J. Comp. Neurol.* *319*, 218–245.
- Van Bockstaele, E.J., and Pickel, V.M. (1995). GABA-containing neurons in the ventral tegmental area project to the nucleus accumbens in rat brain. *Brain Res.* *682*, 215–221.
- Borgland, S.L., Chang, S.-J., Bowers, M.S., Thompson, J.L., Vittoz, N., Floresco, S.B., Chou, J., Chen, B.T., and Bonci, A. (2009). Orexin A/hypocretin-1 selectively promotes motivation for positive reinforcers. *J. Neurosci. Off. J. Soc. Neurosci.* *29*, 11215–11225.
- Boyden, E.S., Zhang, F., Bamberg, E., Nagel, G., and Deisseroth, K. (2005). Millisecond-timescale, genetically targeted optical control of neural activity. *Nat. Neurosci.* *8*, 1263–1268.
- Briand, L.A., Vassoler, F.M., Pierce, R.C., Valentino, R.J., and Blendy, J.A. (2010). Ventral tegmental afferents in stress-induced reinstatement: the role of cAMP response element-binding protein. *J. Neurosci. Off. J. Soc. Neurosci.* *30*, 16149–16159.
- Brischoux, F., Chakraborty, S., Brierley, D.I., and Ungless, M.A. (2009). Phasic excitation of dopamine neurons in ventral VTA by noxious stimuli. *Proc. Natl. Acad. Sci. U. S. A.* *106*, 4894–4899.
- Bromberg-Martin, E.S., Matsumoto, M., and Hikosaka, O. (2010). Dopamine in motivational control: rewarding, aversive, and alerting. *Neuron* *68*, 815–834.
- Broxton, M., Grosenick, L., Yang, S., Cohen, N., Andalman, A., Deisseroth, K., and Levoy, M. (2013). Wave optics theory and 3-D deconvolution for the light field microscope. *Opt. Express* *21*, 25418–25439.
- Burdakov, D., and Alexopoulos, H. (2005). Metabolic state signalling through central hypocretin/orexin neurons. *J. Cell. Mol. Med.* *9*, 795–803.
- Burdakov, D., Gerasimenko, O., and Verkhatsky, A. (2005). Physiological changes in glucose differentially modulate the excitability of hypothalamic melanin-concentrating hormone and orexin neurons in situ. *J. Neurosci. Off. J. Soc. Neurosci.* *25*, 2429–2433.

- Caggiula, A.R., and Hoebel, B.G. (1966). "Copulation-reward site" in the posterior hypothalamus. *Science* 153, 1284–1285.
- Callaway, E.M. (2008). Transneuronal circuit tracing with neurotropic viruses. *Curr. Opin. Neurobiol.* 18, 617–623.
- Cardin, J.A. (2012). Dissecting local circuits in vivo: integrated optogenetic and electrophysiology approaches for exploring inhibitory regulation of cortical activity. *J. Physiol. Paris* 106, 104–111.
- Cardin, J.A., Carlén, M., Meletis, K., Knoblich, U., Zhang, F., Deisseroth, K., Tsai, L.-H., and Moore, C.I. (2009). Driving fast-spiking cells induces gamma rhythm and controls sensory responses. *Nature* 459, 663–667.
- Cardin, J.A., Carlén, M., Meletis, K., Knoblich, U., Zhang, F., Deisseroth, K., Tsai, L.-H., and Moore, C.I. (2010). Targeted optogenetic stimulation and recording of neurons in vivo using cell-type-specific expression of Channelrhodopsin-2. *Nat. Protoc.* 5, 247–254.
- Carter, A.G., and Sabatini, B.L. (2004). State-Dependent Calcium Signaling in Dendritic Spines of Striatal Medium Spiny Neurons. *Neuron* 44, 483–493.
- Chaudhury, D., Walsh, J.J., Friedman, A.K., Juarez, B., Ku, S.M., Koo, J.W., Ferguson, D., Tsai, H.-C., Pomeranz, L., Christoffel, D.J., et al. (2013). Rapid regulation of depression-related behaviours by control of midbrain dopamine neurons. *Nature* 493, 532–536.
- Chemelli, R.M., Willie, J.T., Sinton, C.M., Elmquist, J.K., Scammell, T., Lee, C., Richardson, J.A., Williams, S.C., Xiong, Y., Kisanuki, Y., et al. (1999). Narcolepsy in orexin knockout mice: molecular genetics of sleep regulation. *Cell* 98, 437–451.
- Chen, T.-W., Wardill, T.J., Sun, Y., Pulver, S.R., Renninger, S.L., Baohan, A., Schreiter, E.R., Kerr, R.A., Orger, M.B., Jayaraman, V., et al. (2013). Ultrasensitive fluorescent proteins for imaging neuronal activity. *Nature* 499, 295–300.
- Chow, B.Y., Han, X., Dobry, A.S., Qian, X., Chuong, A.S., Li, M., Henninger, M.A., Belfort, G.M., Lin, Y., Monahan, P.E., et al. (2010). High-performance genetically targetable optical neural silencing by light-driven proton pumps. *Nature* 463, 98–102.
- Christianson, J.P., Jennings, J.H., Ragole, T., Flyer, J.G.N., Benison, A.M., Barth, D.S., Watkins, L.R., and Maier, S.F. (2011). Safety signals mitigate the consequences of uncontrollable stress via a circuit involving the sensory insular cortex and bed nucleus of the stria terminalis. *Biol. Psychiatry* 70, 458–464.
- Chuhma, N., Tanaka, K.F., Hen, R., and Rayport, S. (2011). Functional connectome of the striatal medium spiny neuron. *J. Neurosci. Off. J. Soc. Neurosci.* 31, 1183–1192.
- Cohen, J.Y., Haesler, S., Vong, L., Lowell, B.B., and Uchida, N. (2012). Neuron-type-specific signals for reward and punishment in the ventral tegmental area. *Nature* 482, 85–88.
- Collin, M., Bäckberg, M., Ovesjö, M.-L., Fisone, G., Edwards, R.H., Fujiyama, F., and Meister, B. (2003). Plasma membrane and vesicular glutamate transporter mRNAs/proteins in hypothalamic neurons that regulate body weight. *Eur. J. Neurosci.* 18, 1265–1278.

- Cooke, J.H., Patterson, M., Patel, S.R., Smith, K.L., Ghatei, M.A., Bloom, S.R., and Murphy, K.G. (2009). Peripheral and central administration of xenin and neurotensin suppress food intake in rodents. *Obes. Silver Spring Md* 17, 1135–1143.
- Coward, P., Wada, H.G., Falk, M.S., Chan, S.D.H., Meng, F., Akil, H., and Conklin, B.R. (1998). Controlling signaling with a specifically designed Gi-coupled receptor. *Proc. Natl. Acad. Sci.* 95, 352–357.
- Cui, G., Jun, S.B., Jin, X., Pham, M.D., Vogel, S.S., Lovinger, D.M., and Costa, R.M. (2013). Concurrent activation of striatal direct and indirect pathways during action initiation. *Nature* 494, 238–242.
- Cui, X., Wiler, J., Dzaman, M., Altschuler, R.A., and Martin, D.C. (2003). In vivo studies of polypyrrole/peptide coated neural probes. *Biomaterials* 24, 777–787.
- Cullinan, W.E., Herman, J.P., and Watson, S.J. (1993). Ventral subicular interaction with the hypothalamic paraventricular nucleus: Evidence for a relay in the bed nucleus of the stria terminalis. *J. Comp. Neurol.* 332, 1–20.
- D'Ardenne, K., McClure, S.M., Nystrom, L.E., and Cohen, J.D. (2008). BOLD Responses Reflecting Dopaminergic Signals in the Human Ventral Tegmental Area. *Science* 319, 1264–1267.
- Davis, A., Levoy, M., and Durand, F. (2012). Unstructured Light Fields. *Comp Graph Forum* 31, 305–314.
- Davis, M., Walker, D.L., Miles, L., and Grillon, C. (2010). Phasic vs sustained fear in rats and humans: role of the extended amygdala in fear vs anxiety. *Neuropsychopharmacol. Off. Publ. Am. Coll. Neuropsychopharmacol.* 35, 105–135.
- Deisseroth, K., and Schnitzer, M.J. (2013). Engineering Approaches to Illuminating Brain Structure and Dynamics. *Neuron* 80, 568–577.
- DELGADO, J.M.R., and ANAND, B.K. (1953). Increase of food intake induced by electrical stimulation of the lateral hypothalamus. *Am. J. Physiol.* 172, 162–168.
- Von Der Porten, K., and Davis, J.R. (1979). Weight loss following LH lesions independent of changes in motor activity or metabolic rate. *Physiol. Behav.* 23, 813–819.
- Dombeck, D.A., Harvey, C.D., Tian, L., Looger, L.L., and Tank, D.W. (2010). Functional imaging of hippocampal place cells at cellular resolution during virtual navigation. *Nat. Neurosci.* 13, 1433–1440.
- Domingos, A.I., Sordillo, A., Dietrich, M.O., Liu, Z.-W., Tellez, L.A., Vaynshteyn, J., Ferreira, J.G., Ekstrand, M.I., Horvath, T.L., de Araujo, I.E., et al. (2013). Hypothalamic melanin concentrating hormone neurons communicate the nutrient value of sugar. *eLife* 2.
- Dong, H.-W., and Swanson, L.W. (2004). Organization of axonal projections from the anterolateral area of the bed nuclei of the stria terminalis. *J. Comp. Neurol.* 468, 277–298.

- Dong, H., Petrovich, G.D., and Swanson, L.W. (2000). Organization of projections from the juxtacapsular nucleus of the BST: a PHAL study in the rat. *Brain Res.* 859, 1–14.
- Dong, H.W., Petrovich, G.D., and Swanson, L.W. (2001a). Topography of projections from amygdala to bed nuclei of the stria terminalis. *Brain Res. Brain Res. Rev.* 38, 192–246.
- Dong, H.W., Petrovich, G.D., Watts, A.G., and Swanson, L.W. (2001b). Basic organization of projections from the oval and fusiform nuclei of the bed nuclei of the stria terminalis in adult rat brain. *J. Comp. Neurol.* 436, 430–455.
- Dumont, E.C., and Williams, J.T. (2004). Noradrenaline triggers GABAA inhibition of bed nucleus of the stria terminalis neurons projecting to the ventral tegmental area. *J. Neurosci. Off. J. Soc. Neurosci.* 24, 8198–8204.
- DuPont, R.L., Rice, D.P., Miller, L.S., Shiraki, S.S., Rowland, C.R., and Harwood, H.J. (1996). Economic costs of anxiety disorders. *Anxiety* 2, 167–172.
- Duvarci, S., Bauer, E.P., and Paré, D. (2009). The Bed Nucleus of the Stria Terminalis Mediates Inter-individual Variations in Anxiety and Fear. *J. Neurosci.* 29, 10357–10361.
- Edell, D.J., Toi, V.V., McNeil, V.M., and Clark, L.D. (1992). Factors influencing the biocompatibility of insertable silicon microshafts in cerebral cortex. *IEEE Trans. Biomed. Eng.* 39, 635–643.
- Edinger, H.M., Kramer, S.Z., and Siegel, A. (1977). Effect of hypothalamic stimulation on mesencephalic neurons. *Exp. Neurol.* 54, 91–103.
- Elias, C.F., Saper, C.B., Maratos-Flier, E., Tritos, N.A., Lee, C., Kelly, J., Tatro, J.B., Hoffman, G.E., Ollmann, M.M., Barsh, G.S., et al. (1998a). Chemically defined projections linking the mediobasal hypothalamus and the lateral hypothalamic area. *J. Comp. Neurol.* 402, 442–459.
- Elias, C.F., Saper, C.B., Maratos-Flier, E., Tritos, N.A., Lee, C., Kelly, J., Tatro, J.B., Hoffman, G.E., Ollmann, M.M., Barsh, G.S., et al. (1998b). Chemically defined projections linking the mediobasal hypothalamus and the lateral hypothalamic area. *J. Comp. Neurol.* 402, 442–459.
- Elias, C.F., Sita, L.V., Zambon, B.K., Oliveira, E.R., Vasconcelos, L.A.P., and Bittencourt, J.C. (2008). Melanin-concentrating hormone projections to areas involved in somatomotor responses. *J. Chem. Neuroanat.* 35, 188–201.
- Erb, S., Shaham, Y., and Stewart, J. (2001). Stress-induced relapse to drug seeking in the rat: role of the bed nucleus of the stria terminalis and amygdala. *Stress Amst. Neth.* 4, 289–303.
- Erlander, M.G., Tillakaratne, N.J., Feldblum, S., Patel, N., and Tobin, A.J. (1991). Two genes encode distinct glutamate decarboxylases. *Neuron* 7, 91–100.
- Ettenberg, A., and Camp, C.H. (1986). Haloperidol induces a partial reinforcement extinction effect in rats: implications for a dopamine involvement in food reward. *Pharmacol. Biochem. Behav.* 25, 813–821.
- Fenko, L., Yizhar, O., and Deisseroth, K. (2011). The development and application of optogenetics. *Annu. Rev. Neurosci.* 34, 389–412.

- Fenno, L.E., Mattis, J., Ramakrishnan, C., Hyun, M., Lee, S.Y., He, M., Tucciarone, J., Selimbeyoglu, A., Berndt, A., Grosenick, L., et al. (2014). Targeting cells with single vectors using multiple-feature Boolean logic. *Nat. Methods* 11, 763–772.
- Fields, H.L., Hjelmstad, G.O., Margolis, E.B., and Nicola, S.M. (2007). Ventral tegmental area neurons in learned appetitive behavior and positive reinforcement. *Annu. Rev. Neurosci.* 30, 289–316.
- Flegal KM, Carroll MD, Ogden CL, and Johnson CL (2002). PRevalence and trends in obesity among us adults, 1999-2000. *JAMA* 288, 1723–1727.
- Flusberg, B.A., Nimmerjahn, A., Cocker, E.D., Mukamel, E.A., Barretto, R.P.J., Ko, T.H., Burns, L.D., Jung, J.C., and Schnitzer, M.J. (2008). High-speed, miniaturized fluorescence microscopy in freely moving mice. *Nat. Methods* 5, 935–938.
- Fouriez, G., Hansson, P., and Wise, R.A. (1978). Neuroleptic-induced attenuation of brain stimulation reward in rats. *J. Comp. Physiol. Psychol.* 92, 661–671.
- Fuller, J.H., and Schlag, J.D. (1976). Determination of antidromic excitation by the collision test: Problems of interpretation. *Brain Res.* 112, 283–298.
- Geisler, S., and Zahm, D.S. (2005a). Afferents of the ventral tegmental area in the rat-anatomical substratum for integrative functions. *J. Comp. Neurol.* 490, 270–294.
- Geisler, S., and Zahm, D.S. (2005b). Afferents of the ventral tegmental area in the rat-anatomical substratum for integrative functions. *J. Comp. Neurol.* 490, 270–294.
- Geisler, S., and Zahm, D.S. (2005c). Afferents of the ventral tegmental area in the rat-anatomical substratum for integrative functions. *J. Comp. Neurol.* 490, 270–294.
- Georges, F., and Aston-Jones, G. (2001a). Potent Regulation of Midbrain Dopamine Neurons by the Bed Nucleus of the Stria Terminalis. *J. Neurosci.* 21, RC160–RC160.
- Georges, F., and Aston-Jones, G. (2001b). Potent regulation of midbrain dopamine neurons by the bed nucleus of the stria terminalis. *J. Neurosci. Off. J. Soc. Neurosci.* 21, RC160.
- Georges, F., and Aston-Jones, G. (2002). Activation of Ventral Tegmental Area Cells by the Bed Nucleus of the Stria Terminalis: A Novel Excitatory Amino Acid Input to Midbrain Dopamine Neurons. *J. Neurosci.* 22, 5173–5187.
- Ghosh, K.K., Burns, L.D., Cocker, E.D., Nimmerjahn, A., Ziv, Y., Gamal, A.E., and Schnitzer, M.J. (2011a). Miniaturized integration of a fluorescence microscope. *Nat. Methods* 8, 871–878.
- Ghosh, K.K., Burns, L.D., Cocker, E.D., Nimmerjahn, A., Ziv, Y., Gamal, A.E., and Schnitzer, M.J. (2011b). Miniaturized integration of a fluorescence microscope. *Nat. Methods* 8, 871–878.
- Göbel, W., Kerr, J.N.D., Nimmerjahn, A., and Helmchen, F. (2004). Miniaturized two-photon microscope based on a flexible coherent fiberbundle and a gradient-index lens objective. *Opt. Lett.* 29, 2521–2523.

- Goforth, P.B., Leininger, G.M., Patterson, C.M., Satin, L.S., and Myers, M.G. (2014). Leptin Acts via Lateral Hypothalamic Area Neurotensin Neurons to Inhibit Orexin Neurons by Multiple GABA-Independent Mechanisms. *J. Neurosci.* *34*, 11405–11415.
- Gradinaru, V., Mogri, M., Thompson, K.R., Henderson, J.M., and Deisseroth, K. (2009). Optical deconstruction of parkinsonian neural circuitry. *Science* *324*, 354–359.
- Gradinaru, V., Zhang, F., Ramakrishnan, C., Mattis, J., Prakash, R., Diester, I., Goshen, I., Thompson, K.R., and Deisseroth, K. (2010). Molecular and cellular approaches for diversifying and extending optogenetics. *Cell* *141*, 154–165.
- Gray, T.S., and Magnuson, D.J. (1987). Neuropeptide neuronal efferents from the bed nucleus of the stria terminalis and central amygdaloid nucleus to the dorsal vagal complex in the rat. *J. Comp. Neurol.* *262*, 365–374.
- Gray, C.M., Maldonado, P.E., Wilson, M., and McNaughton, B. (1995). Tetrodes markedly improve the reliability and yield of multiple single-unit isolation from multi-unit recordings in cat striate cortex. *J. Neurosci. Methods* *63*, 43–54.
- Greer, M.A. (1955). Suggestive evidence of a primary drinking center in hypothalamus of the rat. *Proc. Soc. Exp. Biol. Med. Soc. Exp. Biol. Med. N. Y.* *N 89*, 59–62.
- Griffond, B., and Risold, P.Y. (2009). MCH and feeding behavior-interaction with peptidic network. *Peptides* *30*, 2045–2051.
- Grilo, C.M., White, M.A., and Masheb, R.M. (2009). DSM-IV Psychiatric Disorder Comorbidity and Its Correlates in Binge Eating Disorder. *Int. J. Eat. Disord.* *42*, 228–234.
- Gunaydin, L.A., Grosenick, L., Finkelstein, J.C., Kauvar, I.V., Fenno, L.E., Adhikari, A., Lammel, S., Mirzabekov, J.J., Airan, R.D., Zalocusky, K.A., et al. (2014). Natural Neural Projection Dynamics Underlying Social Behavior. *Cell* *157*, 1535–1551.
- Gutierrez, R., Lobo, M.K., Zhang, F., and de Lecea, L. (2011). Neural integration of reward, arousal, and feeding: Recruitment of VTA, lateral hypothalamus, and ventral striatal neurons. *IUBMB Life* *63*, 824–830.
- Hahn, J.D., and Swanson, L.W. (2012). Connections of the lateral hypothalamic area juxtadorsomedial region in the male rat. *J. Comp. Neurol.* *520*, 1831–1890.
- Hammack, S.E., Richey, K.J., Watkins, L.R., and Maier, S.F. (2004). Chemical lesion of the bed nucleus of the stria terminalis blocks the behavioral consequences of uncontrollable stress. *Behav. Neurosci.* *118*, 443–448.
- Hammack, S.E., Mania, I., and Rainnie, D.G. (2007). Differential expression of intrinsic membrane currents in defined cell types of the anterolateral bed nucleus of the stria terminalis. *J. Neurophysiol.* *98*, 638–656.
- Hara, J., Beuckmann, C.T., Nambu, T., Willie, J.T., Chemelli, R.M., Sinton, C.M., Sugiyama, F., Yagami, K., Goto, K., Yanagisawa, M., et al. (2001). Genetic ablation of orexin neurons in mice results in narcolepsy, hypophagia, and obesity. *Neuron* *30*, 345–354.

- Harrell, L.E., Decastro, J.M., and Balagura, S. (1975). A critical evaluation of body weight loss following lateral hypothalamic lesions. *Physiol. Behav.* *15*, 133–136.
- Harris, G.C., Wimmer, M., and Aston-Jones, G. (2005). A role for lateral hypothalamic orexin neurons in reward seeking. *Nature* *437*, 556–559.
- Harrold, J.A., and Halford, J.C.G. (2006). The hypothalamus and obesity. *Recent Patents CNS Drug Discov.* *1*, 305–314.
- Harthoorn, L.F., Sañé, A., Nethé, M., and Heerikhuizen, J.J. (2005). Multi-Transcriptional Profiling of Melanin-Concentrating Hormone and Orexin-Containing Neurons. *Cell. Mol. Neurobiol.* *25*, 1209–1223.
- Haynes, A.C., Chapman, H., Taylor, C., Moore, G.B.T., Cawthorne, M.A., Tadayyon, M., Clapham, J.C., and Arch, J.R.S. (2002). Anorectic, thermogenic and anti-obesity activity of a selective orexin-1 receptor antagonist in ob/ob mice. *Regul. Pept.* *104*, 153–159.
- Heimer, L., and Alheid, G.F. (1991). Piecing together the Puzzle of Basal Forebrain Anatomy. In *The Basal Forebrain*, T.C. Napier, P.W. Kalivas, and I. Hanin, eds. (Springer US), pp. 1–42.
- Hernandez, L., and Hoebel, B.G. (1988). Feeding and hypothalamic stimulation increase dopamine turnover in the accumbens. *Physiol. Behav.* *44*, 599–606.
- Hill, J.O., Wyatt, H.R., Reed, G.W., and Peters, J.C. (2003). Obesity and the Environment: Where Do We Go from Here? *Science* *299*, 853–855.
- Hochbaum, D.R., Zhao, Y., Farhi, S.L., Klapoetke, N., Werley, C.A., Kapoor, V., Zou, P., Kralj, J.M., Maclaurin, D., Smedemark-Margulies, N., et al. (2014). All-optical electrophysiology in mammalian neurons using engineered microbial rhodopsins. *Nat. Methods* *11*, 825–833.
- Hoebel, B.G., and Teitelbaum, P. (1962a). Hypothalamic Control of Feeding and Self-Stimulation. *Science* *135*, 375–377.
- Hoebel, B.G., and Teitelbaum, P. (1962b). Hypothalamic control of feeding and self-stimulation. *Science* *135*, 375–377.
- Huber, D., Gutnisky, D.A., Peron, S., O'Connor, D.H., Wiegert, J.S., Tian, L., Oertner, T.G., Looger, L.L., and Svoboda, K. (2012). Multiple dynamic representations in the motor cortex during sensorimotor learning. *Nature* *484*, 473–478.
- Hudson, J.I., Hiripi, E., Pope Jr., H.G., and Kessler, R.C. (2007). The Prevalence and Correlates of Eating Disorders in the National Comorbidity Survey Replication. *Biol. Psychiatry* *61*, 348–358.
- Ikemoto, S. (2007). Dopamine reward circuitry: Two projection systems from the ventral midbrain to the nucleus accumbens-olfactory tubercle complex. *Brain Res. Rev.* *56*, 27–78.
- Jalabert, M., Aston-Jones, G., Herzog, E., Manzoni, O., and Georges, F. (2009). Role of the bed nucleus of the stria terminalis in the control of ventral tegmental area dopamine neurons. *Prog. Neuropsychopharmacol. Biol. Psychiatry* *33*, 1336–1346.

Javaras, K.N., Pope, H.G., Lalonde, J.K., Roberts, J.L., Nillni, Y.I., Laird, N.M., Bulik, C.M., Crow, S.J., McElroy, S.L., Walsh, B.T., et al. (2008). Co-occurrence of binge eating disorder with psychiatric and medical disorders. *J. Clin. Psychiatry* 69, 266–273.

Jego, S., Glasgow, S.D., Herrera, C.G., Ekstrand, M., Reed, S.J., Boyce, R., Friedman, J., Burdakov, D., and Adamantidis, A.R. (2013). Optogenetic identification of a rapid eye movement sleep modulatory circuit in the hypothalamus. *Nat. Neurosci.* 16, 1637–1643.

Jennings, J.H., and Stuber, G.D. (2014). Tools for Resolving Functional Activity and Connectivity within Intact Neural Circuits. *Curr. Biol. CB* 24, R41–R50.

Jennings, J.H., Sparta, D.R., Stamatakis, A.M., Ung, R.L., Pleil, K.E., Kash, T.L., and Stuber, G.D. (2013a). Distinct extended amygdala circuits for divergent motivational states. *Nature* 496, 224–228.

Jennings, J.H., Rizzi, G., Stamatakis, A.M., Ung, R.L., and Stuber, G.D. (2013b). The Inhibitory Circuit Architecture of the Lateral Hypothalamus Orchestrates Feeding. *Science* 341, 1517–1521.

Johnson, P.M., and Kenny, P.J. (2010). Dopamine D2 receptors in addiction-like reward dysfunction and compulsive eating in obese rats. *Nat. Neurosci.* 13, 635–641.

Johnson, S.W., and North, R.A. (1992). Two types of neurone in the rat ventral tegmental area and their synaptic inputs. *J. Physiol.* 450, 455–468.

Johnston, J.B. (1923). Further contributions to the study of the evolution of the forebrain. *J. Comp. Neurol.* 35, 337–481.

Jordan, J., Joyce, P.R., Carter, F.A., Horn, J., McIntosh, V.V.W., Luty, S.E., McKenzie, J.M., Mulder, R.T., and Bulik, C.M. (2003). Anxiety and psychoactive substance use disorder comorbidity in anorexia nervosa or depression. *Int. J. Eat. Disord.* 34, 211–219.

Ju, G., and Swanson, L.W. (1989). Studies on the cellular architecture of the bed nuclei of the stria terminalis in the rat: I. cytoarchitecture. *J. Comp. Neurol.* 280, 587–602.

Jung, J.C., Mehta, A.D., Aksay, E., Stepnoski, R., and Schnitzer, M.J. (2004). In Vivo Mammalian Brain Imaging Using One- and Two-Photon Fluorescence Microendoscopy. *J. Neurophysiol.* 92, 3121–3133.

Kahn, D., Abrams, G.M., Zimmerman, E.A., Carraway, R., and Leeman, S.E. (1980). Neuropeptide Y neurons in the rat hypothalamus: an immunocytochemical study. *Endocrinology* 107, 47–54.

Karnani, M.M., Apergis-Schoute, J., Adamantidis, A., Jensen, L.T., de Lecea, L., Fugger, L., and Burdakov, D. (2011). Activation of central orexin/hypocretin neurons by dietary amino acids. *Neuron* 72, 616–629.

Karnani, M.M., Szabó, G., Erdélyi, F., and Burdakov, D. (2013a). Lateral hypothalamic GAD65 neurons are spontaneously firing and distinct from orexin- and melanin-concentrating hormone neurons. *J. Physiol.* 591, 933–953.

- Karnani, M.M., Szabó, G., Erdélyi, F., and Burdakov, D. (2013b). Lateral hypothalamic GAD65 neurons are spontaneously firing and distinct from orexin- and melanin-concentrating hormone neurons. *J. Physiol.* *591*, 933–953.
- Kash, T.L., and Winder, D.G. (2006). Neuropeptide Y and corticotropin-releasing factor bi-directionally modulate inhibitory synaptic transmission in the bed nucleus of the stria terminalis. *Neuropharmacology* *51*, 1013–1022.
- Kaye, W.H., Bulik, C.M., Thornton, L., Barbarich, N., Masters, K., and the Price Foundation Collaborative Group (2004). Comorbidity of Anxiety Disorders With Anorexia and Bulimia Nervosa. *Am. J. Psychiatry* *161*, 2215–2221.
- Kelly, R.M., and Strick, P.L. (2000). Rabies as a transneuronal tracer of circuits in the central nervous system. *J. Neurosci. Methods* *103*, 63–71.
- Kempadoo, K.A., Tourino, C., Cho, S.L., Magnani, F., Leininger, G.-M., Stuber, G.D., Zhang, F., Myers, M.G., Deisseroth, K., de Lecea, L., et al. (2013a). Hypothalamic neurotensin projections promote reward by enhancing glutamate transmission in the VTA. *J. Neurosci. Off. J. Soc. Neurosci.* *33*, 7618–7626.
- Kempadoo, K.A., Tourino, C., Cho, S.L., Magnani, F., Leininger, G.-M., Stuber, G.D., Zhang, F., Myers, M.G., Deisseroth, K., de Lecea, L., et al. (2013b). Hypothalamic neurotensin projections promote reward by enhancing glutamate transmission in the VTA. *J. Neurosci. Off. J. Soc. Neurosci.* *33*, 7618–7626.
- Kenny, P.J. (2011). Reward mechanisms in obesity: new insights and future directions. *Neuron* *69*, 664–679.
- Kessler, R.C., Chiu, W.T., Demler, O., and Walters, E.E. (2005). Prevalence, Severity, and Comorbidity of Twelve-month DSM-IV Disorders in the National Comorbidity Survey Replication (NCS-R). *Arch. Gen. Psychiatry* *62*, 617–627.
- Kim, E.R., Leckstrom, A., and Mizuno, T.M. (2008). Impaired anorectic effect of leptin in neurotensin receptor 1-deficient mice. *Behav. Brain Res.* *194*, 66–71.
- Kim, S.-Y., Adhikari, A., Lee, S.Y., Marshel, J.H., Kim, C.K., Mallory, C.S., Lo, M., Pak, S., Mattis, J., Lim, B.K., et al. (2013). Diverging neural pathways assemble a behavioural state from separable features in anxiety. *Nature* *496*, 219–223.
- Knight, Z.A., Tan, K., Birsoy, K., Schmidt, S., Garrison, J.L., Wysocki, R.W., Emiliano, A., Ekstrand, M.I., and Friedman, J.M. (2012a). Molecular Profiling of Activated Neurons by Phosphorylated Ribosome Capture. *Cell* *151*, 1126–1137.
- Knight, Z.A., Tan, K., Birsoy, K., Schmidt, S., Garrison, J.L., Wysocki, R.W., Emiliano, A., Ekstrand, M.I., and Friedman, J.M. (2012b). Molecular profiling of activated neurons by phosphorylated ribosome capture. *Cell* *151*, 1126–1137.
- Koob, G.F., and Le Moal, M. (2001). Drug addiction, dysregulation of reward, and allostasis. *Neuropsychopharmacol. Off. Publ. Am. Coll. Neuropsychopharmacol.* *24*, 97–129.
- Kopelman, P.G. (2000). Obesity as a medical problem. *Nature* *404*, 635–643.

- Korotkova, T.M., Sergeeva, O.A., Eriksson, K.S., Haas, H.L., and Brown, R.E. (2003). Excitation of ventral tegmental area dopaminergic and nondopaminergic neurons by orexins/hypocretins. *J. Neurosci. Off. J. Soc. Neurosci.* *23*, 7–11.
- Kozicz, T., Vigh, S., and Arimura, A. (1997). Axon terminals containing PACAP- and VIP-immunoreactivity form synapses with CRF-immunoreactive neurons in the dorsolateral division of the bed nucleus of the stria terminalis in the rat. *Brain Res.* *767*, 109–119.
- Kranz, G.S., Kasper, S., and Lanzenberger, R. (2010). Reward and the serotonergic system. *Neuroscience* *166*, 1023–1035.
- Krashes, M.J., Koda, S., Ye, C., Rogan, S.C., Adams, A.C., Cusher, D.S., Maratos-Flier, E., Roth, B.L., and Lowell, B.B. (2011). Rapid, reversible activation of AgRP neurons drives feeding behavior in mice. *J. Clin. Invest.* *121*, 1424–1428.
- Kravitz, A.V., Freeze, B.S., Parker, P.R.L., Kay, K., Thwin, M.T., Deisseroth, K., and Kreitzer, A.C. (2010). Regulation of parkinsonian motor behaviours by optogenetic control of basal ganglia circuitry. *Nature* *466*, 622–626.
- Kudo, T., Uchigashima, M., Miyazaki, T., Konno, K., Yamasaki, M., Yanagawa, Y., Minami, M., and Watanabe, M. (2012). Three types of neurochemical projection from the bed nucleus of the stria terminalis to the ventral tegmental area in adult mice. *J. Neurosci. Off. J. Soc. Neurosci.* *32*, 18035–18046.
- Kvitsiani, D., Ranade, S., Hangya, B., Taniguchi, H., Huang, J.Z., and Kepecs, A. (2013). Distinct behavioural and network correlates of two interneuron types in prefrontal cortex. *Nature* *498*, 363–366.
- Lammel, S., Hetzel, A., Häckel, O., Jones, I., Liss, B., and Roeper, J. (2008). Unique Properties of Mesoprefrontal Neurons within a Dual Mesocorticolimbic Dopamine System. *Neuron* *57*, 760–773.
- Lammel, S., Lim, B.K., Ran, C., Huang, K.W., Betley, M.J., Tye, K.M., Deisseroth, K., and Malenka, R.C. (2012). Input-specific control of reward and aversion in the ventral tegmental area. *Nature* *491*, 212–217.
- Laque, A., Zhang, Y., Gettys, S., Nguyen, T.-A., Bui, K., Morrison, C.D., and Muenzberg-Gruening, H. (2013a). Leptin receptor neurons in the mouse hypothalamus are co-localized with the neuropeptide galanin and mediate anorexigenic leptin action. *Am. J. Physiol. Endocrinol. Metab.*
- Laque, A., Zhang, Y., Gettys, S., Nguyen, T.-A., Bui, K., Morrison, C.D., and Muenzberg-Gruening, H. (2013b). Leptin receptor neurons in the mouse hypothalamus are co-localized with the neuropeptide galanin and mediate anorexigenic leptin action. *Am. J. Physiol. Endocrinol. Metab.*
- Lee, J.H., Durand, R., Gradinaru, V., Zhang, F., Goshen, I., Kim, D.-S., Fenno, L.E., Ramakrishnan, C., and Deisseroth, K. (2010). Global and local fMRI signals driven by neurons defined optogenetically by type and wiring. *Nature* *465*, 788–792.

Lein, E.S., Hawrylycz, M.J., Ao, N., Ayres, M., Bensinger, A., Bernard, A., Boe, A.F., Boguski, M.S., Brockway, K.S., Byrnes, E.J., et al. (2007). Genome-wide atlas of gene expression in the adult mouse brain. *Nature* 445, 168–176.

Leininger, G.M., Jo, Y.-H., Leshan, R.L., Louis, G.W., Yang, H., Barrera, J.G., Wilson, H., Opland, D.M., Faouzi, M.A., Gong, Y., et al. (2009). Leptin acts via leptin receptor-expressing lateral hypothalamic neurons to modulate the mesolimbic dopamine system and suppress feeding. *Cell Metab.* 10, 89–98.

Leininger, G.M., Opland, D.M., Jo, Y.-H., Faouzi, M., Christensen, L., Cappellucci, L.A., Rhodes, C.J., Gnegy, M.E., Becker, J.B., Pothos, E.N., et al. (2011a). Leptin action via neurotensin neurons controls orexin, the mesolimbic dopamine system and energy balance. *Cell Metab.* 14, 313–323.

Leininger, G.M., Opland, D.M., Jo, Y.-H., Faouzi, M., Christensen, L., Cappellucci, L.A., Rhodes, C.J., Gnegy, M.E., Becker, J.B., Pothos, E.N., et al. (2011b). Leptin action via neurotensin neurons controls orexin, the mesolimbic dopamine system and energy balance. *Cell Metab.* 14, 313–323.

Levoy, M. (2010). Light Field Photography, Microscopy and Illumination. In *International Optical Design Conference and Optical Fabrication and Testing*, (Optical Society of America), p. ITuB3.

Lewis, T.L., Mao, T., and Arnold, D.B. (2011). A Role for Myosin VI in the Localization of Axonal Proteins. *PLoS Biol* 9, e1001021.

Li, H., Li, Y., Lei, Z., Wang, K., and Guo, A. (2013). Transformation of odor selectivity from projection neurons to single mushroom body neurons mapped with dual-color calcium imaging. *Proc. Natl. Acad. Sci.* 110, 12084–12089.

Lima, S.Q., Hromádka, T., Znamenskiy, P., and Zador, A.M. (2009). PINP: a new method of tagging neuronal populations for identification during in vivo electrophysiological recording. *PLoS One* 4, e6099.

Liu, Z., Zhou, J., Li, Y., Hu, F., Lu, Y., Ma, M., Feng, Q., Zhang, J.-E., Wang, D., Zeng, J., et al. (2014). Dorsal Raphe Neurons Signal Reward through 5-HT and Glutamate. *Neuron* 81, 1360–1374.

Ljungberg, T., Apicella, P., and Schultz, W. (1992). Responses of monkey dopamine neurons during learning of behavioral reactions. *J. Neurophysiol.* 67, 145–163.

Ludwig, D.S., Tritos, N.A., Mastaitis, J.W., Kulkarni, R., Kokkotou, E., Elmquist, J., Lowell, B., Flier, J.S., and Maratos-Flier, E. (2001). Melanin-concentrating hormone overexpression in transgenic mice leads to obesity and insulin resistance. *J. Clin. Invest.* 107, 379–386.

Madisen, L., Zwingman, T.A., Sunkin, S.M., Oh, S.W., Zariwala, H.A., Gu, H., Ng, L.L., Palmiter, R.D., Hawrylycz, M.J., Jones, A.R., et al. (2010). A robust and high-throughput Cre reporting and characterization system for the whole mouse brain. *Nat. Neurosci.* 13, 133–140.

Maeda, H., and Mogenson, G.J. (1982). Effects of peripheral stimulation on the activity of neurons in the ventral tegmental area, substantia nigra and midbrain reticular formation of rats. *Brain Res. Bull.* 8, 7–14.

- Mahler, S.V., and Aston-Jones, G.S. (2012). Fos Activation of Selective Afferents to Ventral Tegmental Area during Cue-Induced Reinstatement of Cocaine Seeking in Rats. *J. Neurosci.* 32, 13309–13325.
- Margolis, E.B., Lock, H., Hjelmstad, G.O., and Fields, H.L. (2006a). The ventral tegmental area revisited: is there an electrophysiological marker for dopaminergic neurons? *J. Physiol.* 577, 907–924.
- Margolis, E.B., Lock, H., Hjelmstad, G.O., and Fields, H.L. (2006b). The ventral tegmental area revisited: is there an electrophysiological marker for dopaminergic neurons? *J. Physiol.* 577, 907–924.
- MARGULES, D.L., and OLDS, J. (1962). Identical “feeding” and “rewarding” systems in the lateral hypothalamus of rats. *Science* 135, 374–375.
- Margules, D.L., and Olds, J. (1962). Identical “feeding” and “rewarding” systems in the lateral hypothalamus of rats. *Science* 135, 374–375.
- Matsumoto, M., and Hikosaka, O. (2009). Representation of negative motivational value in the primate lateral habenula. *Nat. Neurosci.* 12, 77–84.
- Mattis, J., Tye, K.M., Ferenczi, E.A., Ramakrishnan, C., O’Shea, D.J., Prakash, R., Gunaydin, L.A., Hyun, M., Fenno, L.E., Gradinaru, V., et al. (2012a). Principles for applying optogenetic tools derived from direct comparative analysis of microbial opsins. *Nat. Methods* 9, 159–172.
- Mattis, J., Tye, K.M., Ferenczi, E.A., Ramakrishnan, C., O’Shea, D.J., Prakash, R., Gunaydin, L.A., Hyun, M., Fenno, L.E., Gradinaru, V., et al. (2012b). Principles for applying optogenetic tools derived from direct comparative analysis of microbial opsins. *Nat. Methods* 9, 159–172.
- McFarland, K., and Ettenberg, A. (1995). Haloperidol differentially affects reinforcement and motivational processes in rats running an alley for intravenous heroin. *Psychopharmacology (Berl.)* 122, 346–350.
- Mirenowicz, J., and Schultz, W. (1994). Importance of unpredictability for reward responses in primate dopamine neurons. *J. Neurophysiol.* 72, 1024–1027.
- Monahan, P.E., and Samulski, R.J. (2000). Adeno-associated virus vectors for gene therapy: more pros than cons? *Mol. Med. Today* 6, 433–440.
- Mukamel, E.A., Nimmerjahn, A., and Schnitzer, M.J. (2009). Automated analysis of cellular signals from large-scale calcium imaging data. *Neuron* 63, 747–760.
- Nagel, G., Szellas, T., Huhn, W., Kateriya, S., Adeishvili, N., Berthold, P., Ollig, D., Hegemann, P., and Bamberg, E. (2003). Channelrhodopsin-2, a directly light-gated cation-selective membrane channel. *Proc. Natl. Acad. Sci. U. S. A.* 100, 13940–13945.
- Nagy, F.Z., and Paré, D. (2008). Timing of impulses from the central amygdala and bed nucleus of the stria terminalis to the brain stem. *J. Neurophysiol.* 100, 3429–3436.
- Nair-Roberts, R.G., Chatelain-Badie, S.D., Benson, E., White-Cooper, H., Bolam, J.P., and Ungless, M.A. (2008). Stereological estimates of dopaminergic, GABAergic and glutamatergic

- neurons in the ventral tegmental area, substantia nigra and retrorubral field in the rat. *Neuroscience* 152, 1024–1031.
- Nakai, J., Ohkura, M., and Imoto, K. (2001). A high signal-to-noise Ca²⁺ probe composed of a single green fluorescent protein. *Nat. Biotechnol.* 19, 137–141.
- Nassi, J.J., and Callaway, E.M. (2006). Multiple Circuits Relaying Primate Parallel Visual Pathways to the Middle Temporal Area. *J. Neurosci.* 26, 12789–12798.
- Nestler, E.J., and Carlezon, W.A., Jr (2006). The mesolimbic dopamine reward circuit in depression. *Biol. Psychiatry* 59, 1151–1159.
- O'Connor, D.H., Peron, S.P., Huber, D., and Svoboda, K. (2010). Neural activity in barrel cortex underlying vibrissa-based object localization in mice. *Neuron* 67, 1048–1061.
- Olds, J. (1958). Self-stimulation of the brain; its use to study local effects of hunger, sex, and drugs. *Science* 127, 315–324.
- OLDS, J., and MILNER, P. (1954). Positive reinforcement produced by electrical stimulation of septal area and other regions of rat brain. *J. Comp. Physiol. Psychol.* 47, 419–427.
- Olds, J., and Milner, P. (1954). Positive reinforcement produced by electrical stimulation of septal area and other regions of rat brain. *J. Comp. Physiol. Psychol.* 47, 419–427.
- De Olmos, J.S., and Heimer, L. (1999). The concepts of the ventral striatopallidal system and extended amygdala. *Ann. N. Y. Acad. Sci.* 877, 1–32.
- Osakada, F., Mori, T., Cetin, A.H., Marshel, J.H., Virgen, B., and Callaway, E.M. (2011). New rabies virus variants for monitoring and manipulating activity and gene expression in defined neural circuits. *Neuron* 71, 617–631.
- Parylak, S.L., Koob, G.F., and Zorrilla, E.P. (2011). The dark side of food addiction. *Physiol. Behav.* 104, 149–156.
- Phelix, C.F., and Paull, W.K. (1990). Demonstration of distinct corticotropin releasing factor--containing neuron populations in the bed nucleus of the stria terminalis. A light and electron microscopic immunocytochemical study in the rat. *Histochemistry* 94, 345–364.
- Phelps, E.A., and LeDoux, J.E. (2005). Contributions of the amygdala to emotion processing: from animal models to human behavior. *Neuron* 48, 175–187.
- Poulin, J.-F., Arbour, D., Laforest, S., and Drolet, G. (2009). Neuroanatomical characterization of endogenous opioids in the bed nucleus of the stria terminalis. *Prog. Neuropsychopharmacol. Biol. Psychiatry* 33, 1356–1365.
- Poulos, A.M., Ponnusamy, R., Dong, H.-W., and Fanselow, M.S. (2010). Compensation in the neural circuitry of fear conditioning awakens learning circuits in the bed nuclei of the stria terminalis. *Proc. Natl. Acad. Sci. U. S. A.* 107, 14881–14886.

- Qu, D., Ludwig, D.S., Gammeltoft, S., Piper, M., Pelleymounter, M.A., Cullen, M.J., Mathes, W.F., Przypek, R., Kanarek, R., and Maratos-Flier, E. (1996). A role for melanin-concentrating hormone in the central regulation of feeding behaviour. *Nature* 380, 243–247.
- Rogan, S.C., and Roth, B.L. (2011). Remote control of neuronal signaling. *Pharmacol. Rev.* 63, 291–315.
- Roitman, M.F., Wheeler, R.A., and Carelli, R.M. (2005). Nucleus accumbens neurons are innately tuned for rewarding and aversive taste stimuli, encode their predictors, and are linked to motor output. *Neuron* 45, 587–597.
- Rosin, D.L., Weston, M.C., Sevigny, C.P., Stornetta, R.L., and Guyenet, P.G. (2003). Hypothalamic orexin (hypocretin) neurons express vesicular glutamate transporters VGLUT1 or VGLUT2. *J. Comp. Neurol.* 465, 593–603.
- Sakurai, T. (1999). Orexins and orexin receptors: implication in feeding behavior. *Regul. Pept.* 85, 25–30.
- Sakurai, T., Amemiya, A., Ishii, M., Matsuzaki, I., Chemelli, R.M., Tanaka, H., Williams, S.C., Richardson, J.A., Kozlowski, G.P., Wilson, S., et al. (1998). Orexins and orexin receptors: a family of hypothalamic neuropeptides and G protein-coupled receptors that regulate feeding behavior. *Cell* 92, 573–585.
- Sasaki, K., Suzuki, M., Mieda, M., Tsujino, N., Roth, B., and Sakurai, T. (2011). Pharmacogenetic Modulation of Orexin Neurons Alters Sleep/Wakefulness States in Mice. *PLoS ONE* 6, e20360.
- Saunders, A., Johnson, C.A., and Sabatini, B.L. (2012). Novel recombinant adeno-associated viruses for Cre activated and inactivated transgene expression in neurons. *Front. Neural Circuits* 6, 47.
- Schallert, T., and Whishaw, I.Q. (1978). Two types of aphagia and two types of sensorimotor impairment after lateral hypothalamic lesions: observations in normal weight, dieted, and fattened rats. *J. Comp. Physiol. Psychol.* 92, 720–741.
- Schultz, W. (1997). Dopamine neurons and their role in reward mechanisms. *Curr. Opin. Neurobiol.* 7, 191–197.
- Schultz, W. (1998). Predictive Reward Signal of Dopamine Neurons. *J. Neurophysiol.* 80, 1–27.
- Schultz, W. (2007). Multiple dopamine functions at different time courses. *Annu. Rev. Neurosci.* 30, 259–288.
- Schultz, W., Apicella, P., and Ljungberg, T. (1993). Responses of monkey dopamine neurons to reward and conditioned stimuli during successive steps of learning a delayed response task. *J. Neurosci.* 13, 900–913.
- Schulz, D., and Canbeyli, R.S. (2000). Lesion of the bed nucleus of the stria terminalis enhances learned despair. *Brain Res. Bull.* 52, 83–87.

- Schweimer, J.V., and Ungless, M.A. (2010). Phasic responses in dorsal raphe serotonin neurons to noxious stimuli. *Neuroscience* 171, 1209–1215.
- Sharf, R., Sarhan, M., Brayton, C.E., Guarnieri, D.J., Taylor, J.R., and DiLeone, R.J. (2010). Orexin signaling via the orexin 1 receptor mediates operant responding for food reinforcement. *Biol. Psychiatry* 67, 753–760.
- Shimada, M., Tritos, N.A., Lowell, B.B., Flier, J.S., and Maratos-Flier, E. (1998). Mice lacking melanin-concentrating hormone are hypophagic and lean. *Nature* 396, 670–674.
- Sohal, V.S., Zhang, F., Yizhar, O., and Deisseroth, K. (2009). Parvalbumin neurons and gamma rhythms enhance cortical circuit performance. *Nature* 459, 698–702.
- Somerville, L.H., Whalen, P.J., and Kelley, W.M. (2010). Human bed nucleus of the stria terminalis indexes hypervigilant threat monitoring. *Biol. Psychiatry* 68, 416–424.
- Sparta, D.R., Stamatakis, A.M., Phillips, J.L., Hovelsø, N., van Zessen, R., and Stuber, G.D. (2012). Construction of implantable optical fibers for long-term optogenetic manipulation of neural circuits. *Nat. Protoc.* 7, 12–23.
- Stamatakis, A.M., and Stuber, G.D. (2012a). Activation of lateral habenula inputs to the ventral midbrain promotes behavioral avoidance. *Nat. Neurosci.* 15, 1105–1107.
- Stamatakis, A.M., and Stuber, G.D. (2012b). Activation of lateral habenula inputs to the ventral midbrain promotes behavioral avoidance. *Nat. Neurosci.* 15, 1105–1107.
- Stanley, B.G., Ha, L.H., Spears, L.C., and Dee, M.G., 2nd (1993). Lateral hypothalamic injections of glutamate, kainic acid, D,L-alpha-amino-3-hydroxy-5-methyl-isoxazole propionic acid or N-methyl-D-aspartic acid rapidly elicit intense transient eating in rats. *Brain Res.* 613, 88–95.
- St-Pierre, F., Marshall, J.D., Yang, Y., Gong, Y., Schnitzer, M.J., and Lin, M.Z. (2014). High-fidelity optical reporting of neuronal electrical activity with an ultrafast fluorescent voltage sensor. *Nat. Neurosci.* 17, 884–889.
- Straube, T., Mentzel, H.-J., and Miltner, W.H.R. (2007). Waiting for spiders: brain activation during anticipatory anxiety in spider phobics. *NeuroImage* 37, 1427–1436.
- Stuber, G.D., Sparta, D.R., Stamatakis, A.M., van Leeuwen, W.A., Hardjoprajitno, J.E., Cho, S., Tye, K.M., Kempadoo, K.A., Zhang, F., Deisseroth, K., et al. (2011). Excitatory transmission from the amygdala to nucleus accumbens facilitates reward seeking. *Nature* 475, 377–380.
- Swanson, L.W. (1982). The projections of the ventral tegmental area and adjacent regions: a combined fluorescent retrograde tracer and immunofluorescence study in the rat. *Brain Res. Bull.* 9, 321–353.
- Swanson, L.W., Sanchez-Watts, G., and Watts, A.G. (2005). Comparison of melanin-concentrating hormone and hypocretin/orexin mRNA expression patterns in a new parcelling scheme of the lateral hypothalamic zone. *Neurosci. Lett.* 387, 80–84.

- Swinburn, B., Sacks, G., and Ravussin, E. (2009). Increased food energy supply is more than sufficient to explain the US epidemic of obesity. *Am. J. Clin. Nutr.* *ajcn.28595*.
- Sylvers, P., Lilienfeld, S.O., and LaPrairie, J.L. (2011). Differences between trait fear and trait anxiety: implications for psychopathology. *Clin. Psychol. Rev.* *31*, 122–137.
- Takikawa, Y., Kawagoe, R., and Hikosaka, O. (2004). A possible role of midbrain dopamine neurons in short- and long-term adaptation of saccades to position-reward mapping. *J. Neurophysiol.* *92*, 2520–2529.
- Tan, K.R., Yvon, C., Turiault, M., Mirzabekov, J.J., Doehner, J., Labouèbe, G., Deisseroth, K., Tye, K.M., and Lüscher, C. (2012a). GABA Neurons of the VTA Drive Conditioned Place Aversion. *Neuron* *73*, 1173–1183.
- Tan, K.R., Yvon, C., Turiault, M., Mirzabekov, J.J., Doehner, J., Labouèbe, G., Deisseroth, K., Tye, K.M., and Lüscher, C. (2012b). GABA neurons of the VTA drive conditioned place aversion. *Neuron* *73*, 1173–1183.
- Tanofsky-Kraff, M., Bulik, C.M., Marcus, M.D., Striegel, R.H., Wilfley, D.E., Wonderlich, S.A., and Hudson, J.I. (2013). Binge eating disorder: The next generation of research. *Int. J. Eat. Disord.* *46*, 193–207.
- Tessmar-Raible, K., Raible, F., Christodoulou, F., Guy, K., Rembold, M., Hausen, H., and Arendt, D. (2007). Conserved sensory-neurosecretory cell types in annelid and fish forebrain: insights into hypothalamus evolution. *Cell* *129*, 1389–1400.
- Thevenaz, P., Ruttimann, U.E., and Unser, M. (1998). A pyramid approach to subpixel registration based on intensity. *IEEE Trans. Image Process.* *7*, 27–41.
- Thompson, L.T., and Best, P.J. (1990). Long-term stability of the place-field activity of single units recorded from the dorsal hippocampus of freely behaving rats. *Brain Res.* *509*, 299–308.
- Tian, L., Hires, S.A., Mao, T., Huber, D., Chiappe, M.E., Chalasani, S.H., Petreanu, L., Akerboom, J., McKinney, S.A., Schreiter, E.R., et al. (2009). Imaging neural activity in worms, flies and mice with improved GCaMP calcium indicators. *Nat. Methods* *6*, 875–881.
- Tsai, H.-C., Zhang, F., Adamantidis, A., Stuber, G.D., Bonci, A., de Lecea, L., and Deisseroth, K. (2009). Phasic firing in dopaminergic neurons is sufficient for behavioral conditioning. *Science* *324*, 1080–1084.
- Turenius, C.I., Htut, M.M., Prodon, D.A., Ebersole, P.L., Ngo, P.T., Lara, R.N., Wilczynski, J.L., and Stanley, B.G. (2009). GABA(A) receptors in the lateral hypothalamus as mediators of satiety and body weight regulation. *Brain Res.* *1262*, 16–24.
- Turner, J.N., Shain, W., Szarowski, D.H., Andersen, M., Martins, S., Isaacson, M., and Craighead, H. (1999). Cerebral Astrocyte Response to Micromachined Silicon Implants. *Exp. Neurol.* *156*, 33–49.
- Tye, K.M., Prakash, R., Kim, S.-Y., Fenno, L.E., Grosenick, L., Zarabi, H., Thompson, K.R., Gradinaru, V., Ramakrishnan, C., and Deisseroth, K. (2011). Amygdala circuitry mediating reversible and bidirectional control of anxiety. *Nature* *471*, 358–362.

Tye, K.M., Mirzabekov, J.J., Warden, M.R., Ferenczi, E.A., Tsai, H.-C., Finkelstein, J., Kim, S.-Y., Adhikari, A., Thompson, K.R., Andalman, A.S., et al. (2013). Dopamine neurons modulate neural encoding and expression of depression-related behaviour. *Nature* 493, 537–541.

Ungerstedt, U. (1971). Adipsia and aphagia after 6-hydroxydopamine induced degeneration of the nigro-striatal dopamine system. *Acta Physiol. Scand. Suppl.* 367, 95–122.

Ungless, M.A., Argilli, E., and Bonci, A. (2010). Effects of stress and aversion on dopamine neurons: Implications for addiction. *Neurosci. Biobehav. Rev.* 35, 151–156.

Vaughan, E., and Fisher, A.E. (1962). Male sexual behavior induced by intracranial electrical stimulation. *Science* 137, 758–760.

Volkow, N.D., and Wise, R.A. (2005). How can drug addiction help us understand obesity? *Nat. Neurosci.* 8, 555–560.

Vong, L., Ye, C., Yang, Z., Choi, B., Chua Jr., S., and Lowell, B.B. (2011a). Leptin Action on GABAergic Neurons Prevents Obesity and Reduces Inhibitory Tone to POMC Neurons. *Neuron* 71, 142–154.

Vong, L., Ye, C., Yang, Z., Choi, B., Chua, S., Jr, and Lowell, B.B. (2011b). Leptin action on GABAergic neurons prevents obesity and reduces inhibitory tone to POMC neurons. *Neuron* 71, 142–154.

Walker, D.L., and Davis, M. (1997). Double dissociation between the involvement of the bed nucleus of the stria terminalis and the central nucleus of the amygdala in startle increases produced by conditioned versus unconditioned fear. *J. Neurosci. Off. J. Soc. Neurosci.* 17, 9375–9383.

Walker, D.L., and Davis, M. (2008). Role of the extended amygdala in short-duration versus sustained fear: a tribute to Dr. Lennart Heimer. *Brain Struct. Funct.* 213, 29–42.

Walker, D.L., Toufexis, D.J., and Davis, M. (2003). Role of the bed nucleus of the stria terminalis versus the amygdala in fear, stress, and anxiety. *Eur. J. Pharmacol.* 463, 199–216.

Walker, J.R., Ahmed, S.H., Gracy, K.N., and Koob, G.F. (2000). Microinjections of an opiate receptor antagonist into the bed nucleus of the stria terminalis suppress heroin self-administration in dependent rats. *Brain Res.* 854, 85–92.

Wall, N.R., De La Parra, M., Callaway, E.M., and Kreitzer, A.C. (2013). Differential Innervation of Direct- and Indirect-Pathway Striatal Projection Neurons. *Neuron* 79, 347–360.

Walter, A., Mai, J.K., Lanta, L., and Göröcs, T. (1991). Differential distribution of immunohistochemical markers in the bed nucleus of the stria terminalis in the human brain. *J. Chem. Neuroanat.* 4, 281–298.

Watabe-Uchida, M., Zhu, L., Ogawa, S.K., Vamanrao, A., and Uchida, N. (2012). Whole-brain mapping of direct inputs to midbrain dopamine neurons. *Neuron* 74, 858–873.

- Whiddon, B.B., and Palmiter, R.D. (2013). Ablation of Neurons Expressing Melanin-Concentrating Hormone (MCH) in Adult Mice Improves Glucose Tolerance Independent of MCH Signaling. *J. Neurosci.* 33, 2009–2016.
- Wickersham, I.R., Finke, S., Conzelmann, K.-K., and Callaway, E.M. (2007). Retrograde neuronal tracing with a deletion-mutant rabies virus. *Nat. Methods* 4, 47–49.
- Willie, J.T., Chemelli, R.M., Sinton, C.M., Tokita, S., Williams, S.C., Kisanuki, Y.Y., Marcus, J.N., Lee, C., Elmquist, J.K., Kohlmeier, K.A., et al. (2003). Distinct narcolepsy syndromes in Orexin receptor-2 and Orexin null mice: molecular genetic dissection of Non-REM and REM sleep regulatory processes. *Neuron* 38, 715–730.
- Wise, R.A. (1968). Hypothalamic motivational systems: fixed or plastic neural circuits? *Science* 162, 377–379.
- Wise, R.A., Spindler, J., deWit, H., and Gerberg, G.J. (1978). Neuroleptic-induced “anhedonia” in rats: pimozide blocks reward quality of food. *Science* 201, 262–264.
- Witten, I.B., Lin, S.-C., Brodsky, M., Prakash, R., Diester, I., Anikeeva, P., Gradinaru, V., Ramakrishnan, C., and Deisseroth, K. (2010). Cholinergic interneurons control local circuit activity and cocaine conditioning. *Science* 330, 1677–1681.
- Woodworth, C.H. (1971). Attack elicited in rats by electrical stimulation of the lateral hypothalamus. *Physiol. Behav.* 6, 345–353.
- Yang, C.F., Chiang, M.C., Gray, D.C., Prabhakaran, M., Alvarado, M., Juntti, S.A., Unger, E.K., Wells, J.A., and Shah, N.M. (2013). Sexually Dimorphic Neurons in the Ventromedial Hypothalamus Govern Mating in Both Sexes and Aggression in Males. *Cell* 153, 896–909.
- Yang, J.C., Everett, M., Buehler, C., and McMillan, L. (2002). A Real-Time Distributed Light Field Camera. pp. 77–86.
- Yasuda, R., Nimchinsky, E.A., Scheuss, V., Pologruto, T.A., Oertner, T.G., Sabatini, B.L., and Svoboda, K. (2004). Imaging Calcium Concentration Dynamics in Small Neuronal Compartments. *Sci. Signal.* 2004, pl5.
- Yizhar, O., Fenno, L.E., Davidson, T.J., Mogri, M., and Deisseroth, K. (2011). Optogenetics in neural systems. *Neuron* 71, 9–34.
- Yokel, R.A., and Wise, R.A. (1975). Increased lever pressing for amphetamine after pimozide in rats: implications for a dopamine theory of reward. *Science* 187, 547–549.
- Zarevics, P., and Setler, P.E. (1979). Simultaneous rate-independent and rate-dependent assessment of intracranial self-stimulation: evidence for the direct involvement of dopamine in brain reinforcement mechanisms. *Brain Res.* 169, 499–512.
- Van Zessen, R., Phillips, J.L., Budygin, E.A., and Stuber, G.D. (2012a). Activation of VTA GABA neurons disrupts reward consumption. *Neuron* 73, 1184–1194.
- Van Zessen, R., Phillips, J.L., Budygin, E.A., and Stuber, G.D. (2012b). Activation of VTA GABA neurons disrupts reward consumption. *Neuron* 73, 1184–1194.

Zhang, F., Wang, L.-P., Brauner, M., Liewald, J.F., Kay, K., Watzke, N., Wood, P.G., Bamberg, E., Nagel, G., Gottschalk, A., et al. (2007). Multimodal fast optical interrogation of neural circuitry. *Nature* 446, 633–639.

Zhang, S.-J., Ye, J., Miao, C., Tsao, A., Cerniauskas, I., Ledergerber, D., Moser, M.-B., and Moser, E.I. (2013). Optogenetic Dissection of Entorhinal-Hippocampal Functional Connectivity. *Science* 340, 1232627.

Ziegler, D.R., Cullinan, W.E., and Herman, J.P. (2002). Distribution of vesicular glutamate transporter mRNA in rat hypothalamus. *J. Comp. Neurol.* 448, 217–229.

Ziv, Y., Burns, L.D., Cocker, E.D., Hamel, E.O., Ghosh, K.K., Kitch, L.J., Gamal, A.E., and Schnitzer, M.J. (2013a). Long-term dynamics of CA1 hippocampal place codes. *Nat. Neurosci.* 16, 264–266.

Ziv, Y., Burns, L.D., Cocker, E.D., Hamel, E.O., Ghosh, K.K., Kitch, L.J., El Gamal, A., and Schnitzer, M.J. (2013b). Long-term dynamics of CA1 hippocampal place codes. *Nat. Neurosci.* 16, 264–266.